Characterization of vermiculite ores with application to an *in situ* spectral method for determining the source of potentially asbestos-bearing commercial vermiculite insulation

Gregg A. Swayze[1]*, Heather A. Lowers[2], William M. Benzel[2], Roger N. Clark[3], Rhonda L. Driscoll[1], Zac S. Perlman[4], Todd M. Hoefen[1], and M. Darby Dyar[5]

[1]U.S. Geological Survey, MS964 Box 25046 Denver Federal Center, Denver, CO 80225
[2]U.S. Geological Survey, MS973 Box 25046 Denver Federal Center, Denver, CO 80225
[3]Planetary Science Institute, Lakewood, CO 80227
[4]10414 Southwest 26th Street, Davie, FL 33324
[5]Dept. of Astronomy, 206 Kendade, Mount Holyoke College, South Hadley, MA 01075

Revison 2

*E-mail: gswayze@usgs.gov

2

ABSTRACT

Commercially produced vermiculite insulation from Libby, Montana, contains trace levels of asbestiform amphibole, which is known to cause asbestos-related diseases. When vermiculite insulation is found in a building, evaluation for its potential asbestos content traditionally involves collecting a sample from an attic or wall and submitting it for potentially time-consuming analyses at an off-site laboratory. The goal of this study was to determine if *in situ* near-infrared reflectance measurements could be used to reliably identify the source of vermiculite ore and therefore its potential to contain asbestos. Spectra of 52 expanded ore samples, including attic insulation, commercial packing materials, and horticultural products from Libby, Montana; Louisa, Virginia; Enoree, South Carolina; Palabora, South Africa; and Jiangsu, China, were measured with a portable spectrometer. The mine sources for these vermiculite ores were identified based on collection location, when known, and on differences in elemental composition as measured by electron probe microanalysis. Reflectance spectra of the insulation samples show vibrational overtone and combination absorptions that vary in wavelength position and relative intensity depending on elemental composition and proportions of their constituent micas (i.e., vermiculite ore usually consists of a mixture of hydrobiotite and vermiculite mineral flakes). Band depth ratios of the 1.38/2.32-, 1.40/1.42-, and 2.24/2.38-μm absorptions allow determination of a vermiculite insulation's source and detection of its potential to contain amphibole, talc, and/or serpentine impurities. Spectroscopy cannot distinguish asbestiform vs non-asbestiform amphiboles. However, if the spectrally determined mica composition and mineralogy of an insulation sample is consistent with ore from Libby, then it is likely that some portion of the sodic-calcic amphibole it contains is asbestiform, given that all of

the nearly two dozen Libby vermiculite insulation samples examined with scanning electron

microscopy in this study contain amphiboles. One sample of expanded vermiculite ore from

multiple sources was recognized as a limitation of the spectral method, therefore an additional

test (i.e., 2.24-μm absorption position vs 2.24/2.38-μm band depth) was incorporated into the

spectral method to eliminate misclassification caused by such mixtures. With portable field

spectrometers, the methodology developed can be used to determine vermiculite insulation's

source and estimate its potential amphibole content, thereby providing low-cost analysis with

onsite reporting to property owners.

Keywords: vermiculite insulation, expanded vermiculite ore, vermiculite, reflectance

spectroscopy, elongate amphiboles, Libby, provenance, VSPEC method, electron probe

microanalysis

INTRODUCTION

There are approximately one million homes in the U.S. that have expanded vermiculite

attic insulation (Dixon et al. 1985; Gunter et al. 2004). Prior to the early 1990s, between 50 to

80 percent of the world's supply of vermiculite ore was mined near Libby, Montana, where

sodic-calcic elongate amphiboles[1] were a common mineral impurity (ATSDR 2002; Van Gosen

2002; Meeker et al. 2003). During the past 16 years, health studies of residents in the town of

Libby, as well as workers at vermiculite expansion plants that processed vermiculite ore from

this location revealed a high rate of asbestos-related lung disease (Peipins et al. 2003, McDonald

---

[1] In this study, we use the terms "elongate amphiboles" and "elongate amphibole particles"
(NIOSH 2011) to encompass all amphibole crystals longer than 5 μm with an aspect ratio greater
than 3:1 whose habits are asbestiform or nonasbestiform or may have formed as a result of
cleaving or growth. More in-depth discussion of the morphological and optical properties of
amphiboles from Libby, Montana, can be found in Brown and Gunter (2003) and Bellamy and
Gunter (2008).

4

et al. 2004, Larson et al. 2010, Antao et al. 2012). Expanded vermiculite ore from Libby was

marketed as attic insulation under the product brand name Zonolite® until 1984 when its sale was

discontinued (Kentucky DAQ 2016). Previous analyses have shown that vermiculite products

from ores mined from other commercial sources in the U.S. and South Africa do not contain

nearly as much elongate amphibole (Frank and Edmond 2001, Van Gosen 2002, Millette and

Compton 2015).

Building inspectors who encounter vermiculite insulation usually submit samples to

offsite laboratories for routine microscopic examination for asbestos. The need for asbestos

screening is likely to increase as the public becomes aware of the potential health issues posed by

exposure to elongate amphiboles during home improvements or maintenance in areas with

vermiculite insulation or potential liability of owning property containing vermiculite insulation

from Libby. Given the large number of houses and buildings potentially requiring vermiculite

insulation asbestos screening, use of an *in situ* analytical method can save time, eliminate the

need for transport and disposal of hazardous samples, and thereby reduce the cost and lag time of

screening.

There were four major historical sources of vermiculite ore used to make insulation in the

U.S. prior to 1990: (1) most ore came from the Zonolite Mountain Mine near Libby, with the

remainder likely supplied by (2) the Virginia Vermiculite Mine in Louisa, Virginia, (3) several

mines in the Enoree district in South Carolina, and (4) the large Palabora Mine in South Africa.

The Zonolite Mountain Mine is the oldest and largest vermiculite mine in the U.S. having

opened in the early 1920s. The Zonolite® product brand and the mine were acquired by W.R.

Grace in 1963 and mining continued until 1990 when operations ceased in response to concerns

over asbestos contents. Vermiculite ore is still mined from the three-other major historical

sources. Beneficiated vermiculite ore concentrate, made by physically concentrating mica from

the crude ore, contains a mixture of vermiculite and hydrobiotite mineral flakes that are rapidly

heated for a few seconds above 540 °C, causing the loss of interlayer water as steam that escapes

by expanding the mica flakes up to 30 times their original volume. The resulting lightweight

material is used as insulation, horticultural amendments, packaging, chemical sorbent, aggregate,

and in fireproof coatings (Hindman, 2006). See the appendix for a discussion of the geology of

these vermiculite deposits.

The mineral vermiculite $[(Mg,Ca)_{0.35}(Mg,Fe,Al)_3(Al,Si,Fe^{3+})_4O_{10}(OH,F)_2 \cdot 4H_2O]$ is a 2:1

clay (i.e., weathered mica), which forms when K^+ in the interlayer sites of phlogopite[2]

$[K(Mg,Fe,Al)_3(Al,Si,Fe^{3+})_4O_{10}(OH,F)_2]$ is replaced by exchangeable interlayer cations like Mg

usually coordinated between two layers of water (appendix Fig. A1). Vermiculite and

hydrobiotite, a regular 1:1 interstratification of phlogopite and vermiculite (Brindley et al. 1983),

are usually formed as supergene weathering products of phlogopite (Bassett 1959, Deer et al.

1965, Bush 1976, Badreddine et al. 2000). Alteration of phlogopite to hydrobiotite is a

necessary intermediate step in the weathering process that will ultimately form vermiculite if

weathering progresses. Complete conversion of phlogopite to vermiculite increases flake

volume from 10 to 40% along the c-axis as water enters the interlayer sheet. The expansion

---

[2] Rieder et al. (1999) suggest reserving the term "biotite" for the solid-solution series between
Mg-endmember phlogopite and Fe-endmember annite, whereas Tischendorf et al. (2007) suggest
abandoning use of the term "biotite" in favor of more precise terms such as Fe-rich phlogopite,
Al-Fe-rich phlogopite, Mg-rich annite, and Al-Mg rich annite. The dividing line between
phlogopite and annite is defined at $Mg/(Mg+Fe^{2+}) = 0.5$ with phlogopite at lower values and
annite at higher values. According to this convention, most of the "biotite" in the vermiculite
ores examined in this study would then be Al-Fe phlogopite. For simplicity, the term
"phlogopite" is used instead of "Al-Fe rich phlogopite" or "biotite" in this study.

requires that the lithostatic pressure of overlying rocks be exceeded to accommodate this expansion. This limits vermiculite ore formation to a maximum depth of 25 to 30 m below the surface (Hindman 2006). Hydrobiotite is a desired component of vermiculite ores because it has a higher coefficient of expansion relative to pure vermiculite. During flash heating, steam trapped at boundaries between vermiculite and phlogopite domains, within single mica flakes, exerts pressure that exceeds the interlayer bonding forces causing adjoining layers to move apart in an accordion-like fashion (Hillier et al. 2013). This expansion (also known as exfoliation) gives vermiculite ore its lightweight thermal-insulating property.

The color of expanded vermiculite ore varies from dark-mottled golden brown to pure golden brown, with its density and appearance controlled by residence time and furnace temperature (Hindman 2006). Figure 1 shows photos of expanded vermiculite ores from the four major historical sources. In general, individual flakes vary from sub-millimeter up to a few centimeters parallel to their basal cleavage with samples becoming visibly dark-mottled as grain size increases. The air-trapping quality of larger expanded flakes makes them preferred for insulation whereas smaller flakes are used in liquid-absorbent packing, as a lightweight concrete aggregate, and as a water-absorbent horticultural amendment. The color of expanded vermiculite ore is not definitive for distinguishing among sources. Some color variations are related to iron oxidation state: for a given flake size, vermiculite and hydrobiotite flakes generally trend to lighter colors as Fe^{2+} content decreases. Phlogopite that contains both Fe^{2+} and Fe^{3+} has a strong $Fe^{2+} \rightarrow Fe^{3+}$ charge transfer absorption at 0.72 micrometers (μm), and strong Fe^{2+} ligand-field absorptions at 0.92 and 1.15 μm (Robbins and Strens 1972) that span the visible spectral region, thus its flakes can appear dark green to black. During vermiculization (i.e., the alteration of mica

to vermiculite by progressive leaching of K^+ from its interlayer sites), Fe^{2+} is oxidized to Fe^{3+}

causing these absorptions to weaken substantially resulting in the golden hue commonly

associated with pure vermiculite flakes.

Commercial producers sometimes mix vermiculite ores from different sources to achieve

desired physical qualities (see individual sample descriptions in Swayze et al., 2018). In some

attics, vermiculite insulation may be mixed with other materials such as cellulose or fiberglass

(Figs. 1k and l). Over time, household insulation can become adulterated with wood splinters,

insect parts, gypsum wallboard chips, dirt, and dust, which must be taken into account when

evaluating analytical results.

Detection of Impurities in Vermiculite Ores and Determination of Ore Provenance

Traditional methods of analyzing expanded vermiculite ore to detect elongate amphibole

impurities involve time-consuming laboratory inspection using phase contrast microscopy

(PCM), polarized light microscopy (PLM), transmission electron microscopy (TEM), or

scanning electron microprobe (SEM) analysis (Chatfield and Lewis 1980; Beard et al. 2004). In

addition, these methods generate potentially hazardous waste that requires proper disposal.

Analytical results are usually reported about a week or two after the samples are collected.

These approaches do not determine the source of the expanded vermiculite ore.

Chemical analyses can discriminate sources of vermiculite ore by comparing analytical

results to known compositions representative of specific source areas. Electron probe

microanalysis (EPMA) uses wavelength dispersive analysis on individual mica flakes to

determine the source of vermiculite ore samples (Lowers and Meeker 2004) as discussed in

detail later. X-ray fluorescence (XRF) analysis of bulk samples has been used to determine the

composition and source of expanded vermiculite (Gunter et al. 2005), but is sensitive to

impurities (e.g., dirt, wood, cellulose, and fiberglass). Wright and Palmer (2008) differentiated

vermiculite ores and products from China, Libby, Enoree, and South Africa using discriminant

analysis of rare earth, trace, and major elemental data measured with neutron activation and XRF

analyses. X-ray diffraction analysis can be used to determine amphibole content (Sanchez and

Gunter 2006), but cannot be used to determine its elongate habit or the source of the vermiculite

ore. The neutron-activation and X-ray analyses require time-consuming sample preparation.

Millette and Compton (2015) provide a detailed summary of analytical techniques used to

characterize expanded vermiculite products.

While investigating the spectral properties of vermiculite ore from Libby, Montana, we

realized that portable ultraviolet to near infrared (UV – NIR) field spectrometers might be used

to estimate the amount of potentially elongate amphibole in vermiculite insulation in attics and

walls (Clark et al. 2003). We also realized that spectrally identifying the source (i.e.,

provenance) of expanded vermiculite ore might predict the likelihood of elongate amphibole

impurities, and that use of an *in situ* spectral method could speed this evaluation process by

avoiding potentially costly and time-consuming laboratory analysis. Near-infrared spectral

examination of expanded vermiculite ores from the four major historical sources confirms they

have diagnostic vibrational absorptions in the 1.4- and 2.3-μm spectral regions. Reflectance

spectra of 52 expanded vermiculite ore samples, including attic insulation, commercial packing

materials, horticultural products, and aggregate were measured in a laboratory setting with a

portable field spectrometer equipped with a light emitting contact probe (for a detailed sample

list see Table 1). The resulting spectral method applies wavelength positions and relative

9

intensities of its NIR vibrational absorptions to determine the source of the expanded vermiculite

ore and from knowledge of the mineral characteristics of those sources, provide an estimation of

its amphibole content.

METHODS

Buoyancy differences between vermiculite ore's expanded mica components and denser

mineral impurities can be used to concentrate amphiboles for examination. All but 6 of the 52

expanded ore samples had sufficient volume for water-based sink segregation of amphibole

particles/bundles using a modification of the Cincinnati Method (Beard et al. 2004). Flotation

work was performed in a high-efficiency particulate air (HEPA) hood to avoid exposure to

respiratory hazards. For the modified method, 50 mL of a well-mixed expanded ore sample was

placed in a 250-mL beaker and filled with 200 mL of deionized water and stirred well. After 15

minutes, the floating portion of the sample was scooped into a second beaker and put aside to dry

and eventually disposed of as hazardous waste, while the remaining liquid was decanted into a

third beaker being careful not to disturb material resting on the bottom of the beaker. Liquid in

the third beaker was allowed to evaporate and its dried suspended load discarded as hazardous

waste. The sample remaining in the original beaker was allowed to remain in the HEPA hood

until it was completely dry, which usually took a week or longer. This sink fraction was then

examined using a stereomicroscope with its stage fully enclosed in a HEPA hood. Any obvious

elongate amphibole particles/bundles were removed using tweezers and gently crushed into a

sticky-tape mount for SEM examination. If no elongate amphibole particles/bundles were found,

any non-mica mineral grains were mounted for SEM examination and when sufficiently

abundant analyzed by powder x-ray diffraction (XRD). For the remaining six low-volume

samples, a sticky-tape mount was used to collect a dab sample of the container sides for SEM

examination.

SEM analysis of expanded vermiculite ore container dab samples, elongate amphibole

particles, and non-mica mineral grains from the sink fractions was performed on carbon-coated

plugs using a JEOL 5800LV® SEM equipped with a Thermo Fisher silicon drift detector with an

ultra-thin window energy dispersive X-ray analysis system. Samples were examined in both

secondary electron and backscattered electron-imaging modes at 15 kV and approximately 0.5

nA current.

Quantitative elemental analysis of carbon-coated polished grain mounts of unexpanded

and expanded vermiculite ore samples using EPMA were acquired with a fully automated JEOL

JXA-8900® electron microprobe equipped with five wavelength X-ray spectrometers. Operating

conditions were 15 kV, 20 nA (cup), 5 μm beam diameter, and 20 seconds on the peak and 10

seconds on the background. Well-characterized silicate and oxide mineral standards were used

for calibration. The data were normalized to 22 oxygen equivalents using the ZAF correction

procedure supplied by JEOL. The analytical errors for EPMA were approximately ±2 percent

relative concentration for major and minor elements (Si, Al, Fe, Mg, and K) based on replicate

analyses of laboratory standards. Errors for the minor elements (Na, Ca, Ti, and Mn) were

approximately ±3 percent (Lowers and Meeker 2004). Up to 50 individual flakes were analyzed

for samples with adequate grain size and polished surface quality; for the poorest mount where

grain plucking was a problem only 3 flakes could be analyzed (i.e., the coarse-grained GDS700

sample; see Swayze et al., 2018). Statistical comparisons of EPMA compositional data were

11

made with the data analysis routines in Sigma Plot®. Sample populations were tested for

normality and equivalence of variance prior to applying one-way analysis of variability

(ANOVA), and populations that failed the initial tests had ANOVA on ranks. Subsequent to

ANOVA, post hoc multiple comparison tests were applied to identify specific significant

differences.

Traditional determination of non-essential water (H_2O^- released during heating to 105 °C)

and essential water (H_2O^+ released during heating from 105 to 950 °C) in the mineral vermiculite

may underestimate the essential component because weakly held interlayer water may be driven

off by heating at temperatures as low as 80 °C (Weiss and Rowland 1956). A better estimate of

essential water in vermiculite (interlayer plus OH equivalent) and in the vermiculite component

of hydrobiotite was determined by heating the selected unexpanded ore samples (one from each

of the four major historical sources) at 70 °C for 2 hours and subtracting the resulting weight

change values (i.e., absorbed H_2O) from the combined H_2O^- and H_2O^+ values (see Table 2

notes). These samples regained their original weight when left to reabsorb atmospheric water

over a two-day period suggesting their water loss more closely mimics what happens in the

desiccating environment of an electron microprobe sample chamber during analysis, so these

essential water estimates permit more accurate calculation of microprobe elemental totals.

For Mössbauer analysis, approximately 10 to 30 mg sample splits of the four selected

unexpanded vermiculite ore samples were ground and mixed with powdered sugar, and then

gently packed into washer-shaped sample-holders confined by cellophane tape to minimize

preferred orientation. Mössbauer spectra were acquired at 295 K using a source of 100 to 60

mCi [57]Co in Rh on a WEB Research Co. model WT302® spectrometer at Mount Holyoke

College in Massachusetts. For each sample, the fraction of the baseline due to the Compton

scattering of 122 keV gamma rays by electrons inside the detector was subtracted. Run times

were 6 to 24 hours and baseline counts ranged from ~1 to 8 million after the Compton correction.

Spectra were collected in 1024 channels and corrected for nonlinearity via interpolation to a

linear-velocity scale, which is defined by the spectrum of the 25 mm Fe foil used for calibration.

Mössbauer data were fit using Mexfieldd, a program provided by E. De Grave at the University

of Ghent, Belgium. This program solves the full hyperfine interaction Hamiltonian to fit

Lorentzian doublets to the spectral data with isomer shift (IS), quadrupole splitting (QS), and full

width at half maximum (fwhm) as free parameters. Curve fitting was done independent of the

phases present; interpretation and Fe site assignments were made considering all possible phases

and only after careful comparison with literature values.

The selected unexpanded vermiculite ore samples, and as needed, about a third of the

expanded vermiculite ore samples and mineral sink fractions were analyzed using X-ray

diffraction. Samples were dry pulverized with a mortar and pestle to an average particle size of

about 50-150 μm prior to analyses. Approximately 1 gram of each specimen was then packed in

a sample holder and scanned on a Scintag X-1® Automated Diffractometer fitted with a spinning

sample holder. Diffraction patterns were collected using a copper (Cu) K-alpha X-ray tube

operated at 45 kV and 40 mA, a tube divergence slit of 2 mm, tube scatter slit of 4 mm, detector

scatter slit of 1 mm and detector receiving slit of 0.3 mm over a range of 5 to 65 degrees two-

theta with a 0.02 step size and a scan rate of 1 degree per minute. For the selected unexpanded

samples, micronized powder XRD scans were collected on a PANalytical "X'Pert Pro – MPD®

X-ray Diffractometer using the following settings: theta/theta geometry, Cu K-alpha (Ni filtered)

x-ray tube operated at: 45 kV, 40 mA, with a 15 mm beam mask, ½° anti-scatter slit, ¼° divergence slit, ½° receiving anti-scatter slit, ¼° receiving divergence slit, "X'celerator" solid state "strip" detector, step size of 0.033 degrees in continuous scan mode, scan range of 5 to 65 degrees two-theta, and sample spinner on. The scan rate was 2 degrees two-theta per minute. Interpretation of the diffractograms was completed using Materials Data Inc. (MDI 2009) "Jade" search-match software with International Center for Diffraction Data "PDF-4" (Kabekkodu 2010) and National Institute of Standards and Technology (NIST) "FIZ/NIST Inorganic ICSD" databases (Belsky et al. 2002; NIST 2010). Summaries of XRD analyses and diffractograms for the selected unexpanded ore samples, expanded ore samples, and sink fractions are available in Swayze et al. (2018).

Reflectance measurements of expanded vermiculite ore samples, handpicked pure mineral flakes, and mineral impurity standards were made with ASD (PANalytical) FieldPro® and FieldSpec® spectrometers over the wavelength range from 0.35 to 2.5 μm using a contact probe for illumination and Spectralon® disk for reference. Spectra were collected with 2.1 nm sampling interval (resampled to 1 nm by the software) and 11 to 12 nm bandpass (fwhm) over the 1 to 2.5 μm spectral range. Measurements of expanded samples were repeated up to 40 times while shifting the contact probe to cover previously unmeasured flakes. Spectra were converted to absolute reflectance using a modified NIST-traceable Spectralon® reflectance spectrum supplied with the Spectralon® panel by Labsphere, Inc. Wavelength positions are accurate to <1 nm based on annual calibrations done at the ASD (PANalytical) facility and independently verified by the USGS using measurements of well-characterized sharp spectral features in spectra of a Corning® Rare earth element doped glass CG 5121, a clear mylar sheet, and a NIST

SRM 2035 wavelength standard. Higher spectral resolution NIR reflectance spectra of

vermiculite VTx-1 and hydrobiotite GDS469 were measured at 4 cm^{-1} fwhm relative to a

polished stainless-steel mirror on a Nicolet 780 Magna FTIR Spectrometer® equipped with a

Spectrotech® biconical reflectance attachment, KBr beam splitter, and cryogenically cooled InSb

detector from 1.4 to 5 μm. Mid-InfraRed (MIR) transmission spectra of the selected unexpanded

samples, expanded samples, and pure mineral flakes were measured using the same instrument,

pressed KBr pellets (0.7 mg of sample ground in 0.3 g of desiccated KBr), and a cryogenically

cooled MCTB detector from 2 to 25 μm. Because of the small quantity of sample used in the

KBr pellets, variations in the actual amount of sample in each pellet affected the overall

transmission level and hence calculated absorbance level, but not the relative strengths of

adjacent absorptions within a spectrum. NIR transmission spectra of handpicked, ground

mineral flakes and vermiculite ores from Enoree (i.e., the Zonolite® 4 and ALB22SC00 ore

samples) were also measured in pressed pellets, but using a different sample/KBr ratio of 26 mg

of ground sample to 0.274 g of desiccated KBr.

Cation-exchange experiments were also used to evaluate which spectral absorptions were

sensitive to the presence of interlayer cations. Handpicked, ground vermiculite flakes from the

selected unexpanded Libby ore sample were K$^+$ exchanged in a 1 M KCl solution for 48 hours at

22° C then in a 2 M KCl solution for an additional 24 hours at 100° C at a 1:10 solid:liquid

weight ratio. After rinsing, these samples were allowed to dry and then remeasured in NIR

reflectance with an ASD spectrometer and in MIR transmission with the Nicolet spectrometer

using a KBr pellet. Sample splits of the unexpanded Mg-rich VTx-1 vermiculite mineral

standard and the expanded ALB22SC00 ore sample from Enoree, were K^+ exchanged in a similar way (see appendix for more details).

Spectral deconvolution of transmission data was performed with the PeakFit® program, version 4.12 (Systat Software Inc.) after converting the data to absorbance (= $\log_{10} 1/T$; Burns 1993). The spectroscopy peak-fit function "Gaussian+Lorentzian Area" was used to model individual overlapping absorptions of continuum-removed absorbance spectra. Symmetric Gaussians with a fixed shape and variable width were used for deconvolution because this peak shape worked best for modeling absorptions in synthetic annite-siderophyllite micas (Redhammer et al. 2000) and synthetic phlogopite (Papin et al. 1997). Use of Gaussian-Lorentzian peaks with variable shapes and widths was necessary for modeling overlapping interlayer water and OH absorptions in the 1.4-μm spectral region to achieve reasonable fits. As a starting point, the "AutoFit Peaks I Residuals" option that automatically finds hidden peaks by positioning them so their total area equals the area of absorptions in the data was used. Peaks were then manually added and/or shifted to refine the models where there were discrepancies between observed and modeled intensity with the constraint that each additional absorption be reasonably attributable to a predicted OH vibration. Dozens of models were generated for each measured spectrum to find the most spectrally reasonable fits with the best overall r^2 values. Although the most reasonable spectral models are not unique, they represent what is possible within the constraints of the deconvolution program, the assumption of Gaussian peak shapes, predicted OH absorptions, and overall fits to the observed data.

RESULTS AND DISCUSSION

Modified Cincinnati Method

The Cincinnati Method (Beard et al. 2004) for detecting elongate amphiboles in vermiculite ore is based on innovative work done by Chatfield and Lewis (1980). It is a very effective method of isolating elongate amphibole bundles and individual elongate particles from expanded vermiculite ore. Elongate amphibole particles/bundles consist of an aggregate of parallel, small diameter particles attached along their lengths. The original method involves examining the sink fraction to find elongate amphibole bundles and determining their weight percent abundance. If no bundles are detected, then the suspended fraction is examined for individual elongate particles using a SEM or TEM. The strong electrostatic attraction between the mica flakes and container walls, in the relatively dry climate of Colorado, hindered accurate determination of the expanded ore weight fractions and, hence, a precise weight fraction of amphiboles could not be determined. As a result, the weight percent calculations were discontinued and only the presence or absence of elongate amphibole bundles and elongate particles was determined. Other impurities found in the sink fractions and identified by XRD included albite, apatite, augite, amphibole (blocky by visual inspection), calcite, clinochlore, diopside, dolomite, enstatite, hornblende, kaolinite, microcline, muscovite, quartz, serpentine, talc, and tridymite. Out of the 46 expanded ore samples subjected to this modified Cincinnati Method (MCM), all 23 of the Libby samples and 1 sample of mixed expanded ores contained macroscopically visible bundles of elongate amphiboles (Table 1).

Figure 2 shows examples of blue-gray sometimes brown-stained sodic-calcic elongate amphiboles separated from the expanded vermiculite ore samples from Libby. Evidence

discussed in detail later indicates these amphiboles are typical of those found in expanded ore

from Libby, Montana. Amphibole bundle size varies from a few millimeters in width up to 10

mm in length, and typically corresponds to the overall grain size of flakes in the expanded ores.

Finer-grained (<5 mm) ore samples usually contain smaller amphibole bundles. In some

samples, elongate amphiboles occur in patches on or between mica flakes (e.g., gray colored area

of lower left particle Fig. 2c). Magnification may be needed to observe the parallel needle-like

amphibole particles in some of the bundles (e.g., Figs. 2d and e).

SEM Analyses of Sink Fractions

Examples of elongate amphiboles extracted from the sink fractions of expanded

vermiculite ore samples are shown in Figure 3. Gentle pressure, while mounting on SEM stubs

spreads the amphibole particles out for easy detection with secondary electron imaging. The

elongate shape of amphiboles extracted from expanded Libby ore samples is evident in the SEM

micrographs (Figs. 3a to f). Many of the needle-like amphibole particles are <3 μm wide and

have length-to-width ratios of a few hundred to one with a sodic-calcic composition. Some of

these particles are also curved and exhibit splayed ends characteristic of Libby amphibole

(Meeker et al. 2003). An expanded ore sample, spectrally identified as Enoree in origin, has a

rare amphibole bundle with several needle-like particles protruding from its surface (Fig. 3g);

unlike the Libby amphibole bundles, it consists of mostly parallel prismatically shaped particles.

Overall, elongate particles in the relatively abundant Libby amphibole bundles are consistently

thinner and longer than those found more rarely in the sink fractions of expanded ore samples

from the three-other major historical sources (see individual sample descriptions in Swayze et

al., 2018).

Source Determination Using Electron Probe Microanalysis

Lowers and Meeker (2004) investigated the use of EPMA to determine the source of vermiculite ores collected from Enoree, Libby, Louisa, and Palabora. They used covariance diagrams to separate the unexpanded ore samples into groups based on the chemical composition of individual flakes and found that a diagram of Al/Ti versus Al/[Mg/(Mg + Fe^{2+})] demonstrated the best separation among the ore sources. Figure 4 shows their provenance fields modified to accommodate analyses points of 11 expanded ore samples (red dots) with documented provenance from this study (Table 1). EPMA allows the examination of individual mica flakes while avoiding mineral impurities and contaminants, such as fiberglass or gypsum from building materials. Among the 52 expanded vermiculite ore samples, comparison of compositional variations between individual mica flakes revealed several samples were mixtures of expanded ore from multiple sources (Table 1).

Some compositional overlap exists among ores from the four major historical deposits (i.e., provenance fields overlap in Fig. 4), but the refined fields can be used to link expanded vermiculite ores to their sources. The Palabora provenance field (orange ellipse) is isolated to the left of the other fields (at lower Al), whereas the Libby field (blue ellipse) occupies the center of the compositional diagram. In general, spot analyses from the expanded Libby and Palabora ore samples tightly cluster in their respective provenance fields (Figs. 4a and b). Spot analyses of expanded Enoree and Louisa samples (Figs. 4c and d) occupy multiple provenance fields, two of which completely overlap on the right side of the diagram (at higher Al); this makes it more complicated to distinguish ores from these two sources. Nonetheless, spot analyses of Louisa samples usually cluster in the two Louisa fields on the right side of the diagram (green fields in

19

Fig. 4c), whereas spot analyses of Enoree samples cluster in the four Enoree fields (magenta

ellipses in Fig. 4d). Multiple fields for the Enoree samples span a broader range of Al

compositions than do provenance fields of the other ore sources likely reflecting multiple sources

for the Enoree samples. These modified fields can be used to assign the provenance of

undocumented ore samples from the four major historical sources (see Table 1 and the sample

descriptions in Swayze et al., 2018).

Cation compositions of the unexpanded vermiculite ore samples (i.e., bulk samples not

individual minerals) are compared with those of their corresponding expanded ore samples (Fig.

5). Several compositional variations between sources are apparent. Based on box and whisker

diagram comparisons and ANOVA statistical tests of median compositional values (or mean

compositional values as noted in appendix Tables A1 to A4), the Mg fraction of unexpanded

Palabora samples is higher than those of unexpanded Enoree, Libby, and Louisa samples (Fig.

5a). Tetrahedral Al fraction is highest for unexpanded Libby and Louisa samples but notably

lower for unexpanded Palabora samples with intermediate values in unexpanded Enoree samples

(Fig. 5b). Among unexpanded samples, total Al shows the strongest systematic decrease from

Louisa to Palabora samples whereas total Fe is lowest in Enoree and Palabora samples (Figs. 5c

and 5d). The expanded samples follow these same trends with total Fe lowest in the Palabora

samples (Fig. 5a to d). Table 2 lists bulk compositions for selected unexpanded vermiculite ore

samples from each major historical source. These compositions are statistically representative of

all analyzed unexpanded ore samples from their respective sources for Libby, Louisa, and

Palabora. Similarly, the selected unexpanded sample from Enoree (i.e., Zonolite® 4) has a bulk

composition that is statistically representative of most but not all analyzed unexpanded samples

from this source (Table A3). This is not unexpected given the large number of regionally

separate sources supplying the mill at Enoree. Based on these observations, the selected

unexpanded Louisa and Enoree samples contain sufficient Al to complete their tetrahedral layers

following the convention (Deer et al. 1966) that when completing formulas, the tetrahedral layers

are filled first. In contrast, the composition of the selected unexpanded ALB5SA00 sample

indicates that for Palabora ore, there is a deficiency in Al and Si necessary to complete their

tetrahedral layers on a bulk sample basis, requiring 4% of the sites to be filled with Fe^{3+} (Table

2). Additional evidence for tetrahedral Fe^{3+} is discussed in the Mössbauer section below.

Likewise, the selected unexpanded GDS469 sample from Libby requires a trace amount of Fe^{3+}

to complete its tetrahedral layers on a bulk sample basis. The analyses in Table 2 also indicate

that interlayer sites of unexpanded samples from Enoree and Libby may contain more Ca than

Mg.

Mössbauer Analysis

Mössbauer spectra of the four selected unexpanded vermiculite ore samples were

measured and modeled to determine the distribution of Fe among sites and valence states

(appendix Fig. A2). Results listed in Table 3 show all samples contained some Fe^{2+} in

octahedral sites (9-26% of the total Fe atoms), but the majority of Fe in all cases was Fe^{3+}.

Mössbauer spectra of phyllosilicates may have up to three Fe^{3+} distributions corresponding to

highly overlapped combinations of Fe^{3+} in the M1, M2, and octahedral sites (Dyar et al. 2008),

but it is often not possible to distinguish Fe^{3+} distributions among those sites without

independent evidence such as from composition (Dyar 1993, 2002; Dyar et al. 2008). Typically,

Fe^{3+} in tetrahedral sites has an isomer shift around 0.20 mm/s, but no doublet with that centroid

was observed in unconstrained fits to spectra of any of the samples. All samples had a low

isomer shift doublet of about 0.26-0.39 mm/s that could be a mixture of doublets from

tetrahedral and octahedral occupancy. In such cases, it is necessary to use crystal chemical

arguments to differentiate between Fe^{3+} in the two sites. The lowest isomer shift doublet was

observed in the unexpanded ALB5SA00 sample from Palabora, which lacks sufficient Si plus Al

to complete its tetrahedral layers. So, for this Palabora sample only, it is assumed that some of

the Fe^{3+} is in the tetrahedral site (Fig. 6). Areas under the curves are accurate to within ± 1-3%

of the total Fe, and what was observed from these measurements is well within those limits.

Badreddine et al. (2000) note that Palabora phlogopites contain about 35 to 40% of their total Fe

as tetrahedral Fe^{3+} compared to the ALB5SA00 sample with 38% of its total Fe as tetrahedral

Fe^{3+} (Table 2).

X-Ray Diffraction Analysis

Qualitative XRD analyses, with no internal standards, were performed on about one third

of the 52 expanded vermiculite ore samples to characterize their mica constituents (see sample

descriptions in Swayze et al., 2018). Handpicked grains and MCM sink fractions from many

samples were analyzed by XRD to determine the presence of amphibole, talc, and serpentine

impurities. Table 1 lists the six expanded samples that lacked sufficient volume for MCM

analysis. When feasible, elongate amphibole bundles were removed from the sink fractions for

SEM examination prior to performing discretionary XRD analyses of the remaining handpicked

grains. It is worth noting that expansion may destroy some of the long-range crystallographic

order of vermiculite and hydrobiotite flakes that is the basis of XRD. Loss of long-range order in

major constituents causes minor unexpandable phases, such as phlogopite, to appear more

abundant in XRD measurements.

Quantitative XRD analyses were used to characterize the relative proportions of

phlogopite, hydrobiotite, and vermiculite mineral components of the four selected unexpanded

vermiculite ore samples. Initially, a semi-quantitative mineral mode was calculated for each

sample. Lack of appropriate reference structure information for hydrobiotite limited the options

for quantification. Neither the International Center for Diffraction Data (ICDD) database nor the

Inorganic Crystal Structure Database (ICSD) contains a complete structure card for hydrobiotite.

Without a complete structure reference for hydrobiotite, rigorous models such as Rietveld

refinement cannot be used to quantify mineral contents of the ore samples. There is one

reference card in the ICDD Relational Database (Brindley et al. 1983) of a regular 1:1

interstratification of phlogopite and vermiculite layers (hydrobiotite). This information was

suitable for use of relative intensity ratios (RIR) as part of a "whole pattern fit" model.

The first part of this quantitative XRD study involved determining the composition of the

hydrobiotite phase. To accomplish this task, scans were completed on oriented mounts of the

four selected unexpanded ore samples. Interpretive tables from Brindley et al. (1983) were used

to estimate the proportion of phlogopite and vermiculite in the hydrobiotite interstratification.

As noted by Brindley et al. (1983) who used large individual flakes of their source materials to

collect high-quality data, measurements made on bulk materials will reflect a range of values

from the numerous flakes in the sample. Our oriented scans yielded a range of phlogopite

fractions for the hydrobiotite component of the samples as shown in the rightmost pie diagrams

in Figure 7. Although the uncertainty in the fractions is large for some of the samples, the results

23

show that the hydrobiotites are not perfect 1:1 interstratifications of phlogopite and vermiculite in all samples.

The second part of this quantitative XRD study focused on determining the abundances of the mineral components of the selected unexpanded ore samples. Data for mineral quantification were collected using these samples amended with an internal standard. Isolated flakes of nearly pure mineral phases of phlogopite, hydrobiotite, and vermiculite were blended with corundum in a 50:50 weight ratio mixture. Random mounts of these powders were scanned and the peak height of the {001} reflection of phlogopite and {002} reflection of hydrobiotite and {001} or {002} reflection (dependent on space group assignment) in vermiculite were ratioed against the {104} reflection of corundum. This produced RIR values of 1.1, 1.3, and 6.7 for phlogopite, hydrobiotite, and vermiculite, respectively.

These calculated RIR values were checked against other published values to verify the method was yielding reasonable results. Hydrobiotite is the only one of the three micas that does not have a published RIR value in the peer-reviewed national databases. Phlogopite has more than 90 entries between ICDD and ICSD with RIR values ranging from 0.55 to 1.76 with a median value of 1.09. That compares well with our calculated value of 1.1. There are nine entries for vermiculite that have RIR values, ranging from 8.78 to 21.49. However, all but two of the entries have notes indicating they were laboratory synthesized, chemically treated or have known interlayering with other phases. The two remaining vermiculites both have RIR values of 9.5. Although the calculated value of 6.7 is approximately 30% lower than the 9.5, the RIR value can be very sensitive to substitutions in the mineral and orientation during sample preparation for the measurement. Given these limitations, the 6.7 calculated RIR was accepted

as a reasonable value for this work. Based on the phlogopite and vermiculite comparisons, the

method was applied to these mixtures with the understanding that that accurate mineral

quantification may have errors but the relative differences among the samples are correct.

Using these derived RIR values, the mineral contents were calculated from the random

mount scans shown in Figure 7. Because the Libby hydrobiotite {002} peak has a larger fwhm

value (broader peak) than observed in the three other selected unexpanded ore samples, the

hydrobiotite estimate for the Libby sample is considered a minimum value.

Quantitative estimates of phlogopite, hydrobiotite, and vermiculite for the four selected

unexpanded ores are given in the leftmost ore components pie charts in Figure 7. The Palabora

sample contains mostly hydrobiotite (93 wt%) and minor vermiculite (7 wt%) with no

phlogopite. Both Louisa and Enoree samples contain less hydrobiotite (~70 wt%), more

vermiculite (~30 wt%), with no phlogopite. The Libby sample contains the least hydrobiotite

(52 wt%) with the most vermiculite (38 wt%), but also has a notable amount of phlogopite (10

wt%).

Hydrobiotite flakes in the Libby and Palabora selected unexpanded ore samples are

nearly 1:1 mixtures of phlogopite and vermiculite, whereas hydrobiotite in the Louisa and

Enoree samples deviate from 1:1 ratios. Combining the amount of phlogopite resolved in the

bulk sample with the phlogopitic component of hydrobiotite gives 45 wt% total phlogopite in the

Palabora sample, about 36 wt% in the Enoree sample, and only about 34 wt% in the Louisa

sample. Note that the Libby sample contains a minimum of 36 wt% phlogopite based on these

measurements, but spectroscopic measurements suggest a greater phlogopite content (described

below).

25

Spectral Analysis

Mineral Impurities in Expanded Vermiculite Ore. *In situ* detection of mineral

impurities in expanded vermiculite ore using reflectance spectroscopy would simplify the task of

identifying potentially hazardous vermiculite insulation. Amphibole itself is spectrally

recognizable when present as a major or minor impurity in vermiculite ore. However, at the low

levels normally present, amphibole's diagnostic absorptions can be overwhelmed by mica's

stronger absorptions. In particular, direct spectral identification of amphibole at trace levels (<5

wt%) is difficult because expanded vermiculite ore has vibrational OH-stretch overtone and OH-

stretch-plus-bend combination absorptions in the 1.4- and 2.3-μm spectral regions, respectively,

which can conceal diagnostic amphibole absorptions (Fig. 8). Talc and serpentine also have OH

overtone absorptions at nearly the same wavelengths as amphibole, so these impurities may not

be distinguishable from amphibole at low concentrations in the NIR spectral region.

Expanded vermiculite ore's 1.4-μm OH overtone absorptions are relatively weak and

more easily influenced by the overlapping spectral features of amphibole, talc, and serpentine

impurities. These weak overtone absorptions are a consequence of vermiculite ore's micaceous

habit. For instance, in trioctahedral micas like phlogopite, hydrobiotite, and vermiculite, the

majority of the octahedral layer hydroxyls' O-H bonds are oriented nearly perpendicular to the

basal cleavage. Most photons entering these micas at a high angle to the basal cleavage tend to

travel a shorter path through the mica flakes before scattering out, whereas those entering at a

low angle tend to travel a longer path and are preferentially absorbed without being scattered

back out. Photons entering mica flakes perpendicular to their basal cleavage excite a smaller

cross-section of O-H bonds, responsible for the OH stretching vibrations, but a larger cross

section of the cation-OH bonds, giving rise to the bend vibrations. This propensity for selective

absorption and mica's tendency for preferred orientation biases the reflected light toward those

photons that scatter out of the basal plane, thereby producing relatively strong combination bands

but fairly weak overtone absorptions (top spectrum of Fig. 8). Because amphibole, talc, and

serpentine have relatively stronger overtones in reflectance (lower three spectra in inset of Fig.

8), they will contribute more, even when present at trace levels, to the composite OH overtone

absorption at 1.40 μm in expanded vermiculite ore, than do their combination absorptions in the

2.3-μm region, which overlap with stronger mica combination absorptions.

Spectral Features of Phlogopite, Hydrobiotite, and Vermiculite. Distinguishing

features among the spectra of expanded vermiculite ores from Enoree, Libby, Louisa, and

Palabora can be used to sort the 52 expanded ore samples based on their respective sources (Fig.

9). The 1.4-μm region contains three composite OH overtone absorptions near 1.38, 1.40, and

1.42 μm that are superimposed on the shorter wavelength wing of a broad composite 1.43-μm

interlayer water absorption. Figure 9b displays these three, narrow composite OH overtone

absorptions particularly well. The 1.91-μm composite H_2O-combination absorption strengthens

as vermiculite and its component in hydrobiotite in the unexpanded ores increase, but weakens

during heat-induced expansion as water is driven off. A composite OH-stretch-plus-bend

combination absorption, which forms a shoulder at 2.24 μm, is strongest in expanded Louisa and

Enoree samples (leftmost vertical lines Figs. 9c and d), intermediate in the expanded Libby

sample (Fig. 9a), and weakest in expanded Palabora sample (Fig. 9b). The 2.3-μm region has

OH-stretch-plus-bend combination absorptions near 2.30, 2.32, and 2.38 μm that vary in relative

strength depending on the ratio of vermiculite to phlogopite (including those components in

hydrobiotite) for each different source. The long wavelength wings of intense 0.72, 0.92 and

1.15 μm Fe-electronic absorptions overlap the narrow OH-overtone-region absorptions to

varying degrees but overlap least in the expanded Palabora sample (i.e., arrow at 1.82-μm in Fig.

9b versus arrows at 2.15-μm in spectra of the other samples in Figs. 9a, c, and d). Note that

individual components of these narrow vibrational absorptions overlap and so are commonly

unresolved, but the position of their composite absorption's minimum (in reflectance) or

maximum (in absorbance) can be referred to as occurring at a single wavelength.

Continuum-removed spectra of handpicked, ground flakes of phlogopite, hydrobiotite,

and vermiculite from the unexpanded Libby GDS469 ore have features that change with

progressive vermiculization (see appendix for explanation of continuum-removal process). The

1.40- and 1.42-μm absorptions increase and the 1.38-μm absorption decreases as alteration

progresses from phlogopite to hydrobiotite and ultimately to vermiculite (Fig. 10a). A similar

change is recognized in the combination region where 2.32- and 2.38-μm phlogopite absorptions

weaken as the 2.30-μm vermiculite absorption grows (Fig. 10b). Note that the 1.42-μm OH-

stretch-overtone absorption is overwhelmed by the considerably stronger, overlapping interlayer

water absorptions in the 1.43-μm spectral region of the ground vermiculite flakes (bottom

spectrum of Fig. 10a). Vermiculite ores are mixtures of these three mica components and their

relative proportions vary according to the extent of vermiculization in each sample.

Most spectral changes caused by vermiculization can be reversed by K^+ saturation.

Figures 10c and d show how spectra of ground vermiculite flakes change as the extent of K^+

saturation increases and their interlayers collapse as water is replace by K^+. In general, the

sequence of spectral changes during progressive K^+ substitution is the reverse of those induced

by vermiculization (e.g., in Fig. 10 compare spectra in c to those in a and spectra in d to those in

b). Note the growth of a 1.38-μm overtone absorption and decrease of the 2.30-μm combination

absorption in the K^+-exchanged vermiculite spectra. Many of the spectral changes caused by

vermiculization are a result of water replacing interlayer K^+ and the impact this has on O-H bond

lengths in adjacent octahedral sites. Examining corresponding spectral changes in absorbance in

the MIR region facilitates unraveling the complexities of these NIR absorptions.

Mid-Infrared Fundamental Absorptions of Micas in Vermiculite Ore. Generally, the

NIR overtone and combination spectral regions mirror details of fundamental absorptions in the

3700 cm^{-1} (2.7 μm) OH stretch and 700 cm^{-1} (14.3 μm) cation-OH bend regions. Based on

crystal symmetry, there is only one IR-active hydroxyl stretching vibration predicted in

trioctahedral micas; however, local differences in octahedral content, interlayer cations, and

tetrahedral layer composition can give rise to multiple hydroxyl stretch absorptions (Farmer

1974).

In phlogopite, the frequencies at which O-H bonds absorb light is influenced by the type

of cations in the octahedral layer, with substitution of Al and Fe for Mg causing absorption at

lower frequencies (Vedder and Wilkins 1969), with at most slight coupling between OH

vibrations (Farmer 1974). Vedder (1964) defines three types of OH-stretch absorptions in micas:

N-band (normal), I-band (impurity), and V-band (vacancy) absorptions caused by different

combinations of cations occupying the three immediately neighboring octahedral layer sites

adjacent to hydroxyl ions. Table 4 lists the cation cluster combinations likely to occur in

phlogopite, hydrobiotite, and vermiculite. Hydroxyls bonded to three divalent, octahedrally

coordinated cations (i.e., Mg, Fe^{2+}, or combinations of these cations) give rise to the N-band

absorptions near 3700 cm^{-1}. Hydroxyls bonded to two divalent and one trivalent cation (i.e., Al

or Fe^{3+}) give rise to the I-band absorptions near 3660 cm^{-1}. Hydroxyls adjacent to an octahedral

vacancy give rise to V-band absorptions near 3620 cm^{-1}. Because vermiculite ores from the four

major historic sources are relatively Mg-rich (see Table 2 and Fig. 5a), the probability of Fe^{2+}- or

Fe^{3+}-dominated cation clusters is very low. Accordingly, Fe-dominant cation clusters in these

ores will yield only weak absorptions at slightly lower frequencies than their Mg-dominant

analogues. Consequently, the MIR absorbance spectra of these vermiculite ores are dominated

by N-, I-, and V-band absorptions associated with Mg-dominant cation clusters (e.g., N-bands =

Mg$_3$OH and Mg$_2$Fe^{2+}OH; I-bands = Mg$_2$AlOH and Mg$_2$Fe^{3+}OH; V-bands = MgAl[   ]OH, and

MgFe^{3+}[   ]OH; after Vedder and Wilkins, 1969).

With progressive conversion of phlogopite to vermiculite, apparent shifts of composite

absorptions to lower frequencies are likely caused by the growth of new overlapping absorptions

at the expense of the original ones with changes in interlayer and octahedral occupancy. Figure

11 shows absorptions in spectra of handpicked, ground flakes of phlogopite, hydrobiotite, and

vermiculite from the unexpanded Libby GDS469 sample. This figure includes the deconvolved

symmetric Gaussian absorptions expected for the OH vibrations in the 3700 cm^{-1} region,

compared with a spectrum of handpicked, ground K$^+$-exchanged Libby vermiculite flakes.

Slight variations in the quantity of sample used in the preparation of the KBr pellets lead to

variations in the magnitudes of the computed absorbance. Nonetheless, the relative intensities of

the absorptions in a given spectrum are accurate and spectral shifts are consistent.

Spectral deconvolution can help unravel the complexities of observed band shifts and

help us understand how to use them as fingerprints to distinguish between sources of expanded

vermiculite ores. Critical to this effort is the observation that second-neighbor effects from

variable Si and Al compositions of the pseudo-hexagonal rings of six tetrahedra facing each

hydroxyl group (e.g., see appendix Fig. A1) can give rise to additional overlapping versions of

each cation cluster absorption (Papin et al. 1997). Based on the asymmetry of the 3710 cm^{-1}

composite absorption, most clearly seen in the spectrum of the ground Libby vermiculite flakes

(i.e., third spectrum from the top in Fig. 11), there are two Mg_3OH cation cluster absorptions (N-

band stretches). The higher frequency ν_a absorption at 3718 cm^{-1} results from hydroxyl adjacent

to a tetrahedral Si_5Al ring whereas the lower frequency ν_b absorption at 3708 cm^{-1} results from

hydroxyl adjacent to a Si_4Al_2 ring. This frequency shift is attributed to increased negative charge

on the tetrahedral oxygens with increasing Al or Fe^{3+} content of the neighboring tetrahedral sites.

The greater negative charge increases the degree of hydrogen bonding thus producing a duplicate

overlapping absorption at a slightly lower frequency. This results in an apparent broadening of

the Mg_3OH absorption, which becomes a composite absorption. The same applies for the I-

bands. Notation such as $Mg_3OH:Si_5Al$ can be used to indicate an Mg_3OH cluster adjacent to a

Si_5Al tetrahedral ring and its corresponding absorption, and is used in this study to assign

individual OH absorptions (e.g., Tables 5 and 6) following the convention adopted by Papin et

al. (1997). Langner et al. (2012) note that Al content in phlogopite increases according to

Tschermak's coupled substitution $^{VI}Mg + ^{IV}Si = ^{VI}Al + ^{IV}Al$, which maintains charge balance.

Accordingly, the higher frequency absorptions are from hydroxyls in Mg-Si coupled regions

whereas lower frequency absorptions are from hydroxyls in $^{IV}Al – ^{VI}Al$ coupled regions that

stretch across tetrahedral and octahedral layers. Table 5 lists the frequencies and corresponding

wavelength positions of vibrational assignments for OH-related MIR fundamental absorptions of

phlogopite, hydrobiotite, and vermiculite from the unexpanded Libby GDS469 sample.

Previous studies have shown that the interlayer cation also influences the frequencies of

light absorbed by hydroxyl in trioctahedral micas. According to Serratosa and Bradley (1958)

and Serratosa et al. (1970), O-H bonds in these micas are oriented nearly perpendicular to the

tetrahedral layers, with their hydrogens pointing toward the hexagonal holes. These hydrogens

are repulsed by interlayer cations, which cause the O-H bonds to absorb light at higher

frequencies (i.e., ~ 3700 cm^{-1}). The spectrum of talc can be used as an analogue for vermiculite

that has only H_2O in its interlayer sites, because both produce similar "unperturbed" OH

vibrations that give rise to stretch absorptions at lower frequencies near 3680 cm^{-1}. Wunder and

Melzer (2002) noted similar absorptions between 3674 and 3678 cm^{-1} in synthetic phlogopite

with interlayer site vacancies that they attribute to a "talc component" resulting from Mg_3OH

cation clusters. The ν_d and ν_e absorptions in spectra of hydrobiotite and vermiculite from Libby

(middle spectra of Fig. 11) are assigned to this "unperturbed" hydroxyl, which is designated as

$Mg_3OH_{non-repulsed}$ (Table 5). By analogy, the ν_a and ν_b absorptions in these spectra are assigned to

the "perturbed" hydroxyl, which is designated as $Mg_3OH_{repulsed}$. The same applies to I-band

absorptions ν_f and ν_g near 3660 cm^{-1}, which are due to repulsed $Mg_2(Fe^{3+}, Al, Ti)OH$ cation

cluster, whereas ν_h and ν_j near 3630 cm^{-1} are the corresponding non-repulsed I-band absorptions

(see hydrobiotite and vermiculite spectra in Fig. 11). There is an inverse relationship between

the strength of the repulsed and non-repulsed absorptions in these micas, with the repulsed

absorptions strongest in phlogopite and weakest in vermiculite, whereas the opposite holds for

the non-repulsed absorptions.

According to Vedder and Wilkins (1969), oxidation of Fe^{2+} results in an increase in the

intensity of the I-band absorptions as the N-band absorptions diminish. An example is the ν_c

$Mg_2Fe^{2+}OH_{repulsed}$ absorption at 3696 cm^{-1}, which systematically weakens from phlogopite to

vermiculite as Fe^{2+} is oxidized to Fe^{3+} during vermiculization (Fig. 11). Oxidation of Fe^{2+} results

in dehydrogenation of one of the two hydroxyl groups associated with it, whereas the surviving

hydroxyl then contributes intensity to the ν_f and ν_g $Mg_2Fe^{3+}OH_{repulsed}$ I-band absorptions. This

new contribution to I-band intensity is enhanced relative to the surviving hydroxyl's original N-

band contribution because its absorption coefficient is now twice as high in the I environment

(Sanz et al. 1983, and reference therein).

V-band absorptions (i.e., ν_i and ν_k) are an order of magnitude weaker than N- and I-band

absorptions in Libby phlogopite and hydrobiotite, but about half as intense as the N-band

absorptions in vermiculite (compare ν_i and ν_k to ν_a and ν_b in the top three spectra of Fig. 11).

O-H bonds adjacent to cation clusters with vacancies are oriented nearly parallel to the mica

layers, and may point toward these vacancies (Serratosa el al. 1970). These hydrogens form

strong hydrogen bonds to adjacent apical tetrahedral oxygens, thus lengthening their O-H bonds,

giving rise to V-band absorptions at relatively low frequencies (Farmer et al. 1971; Robert and

Kodama 1988). Farmer (1974) notes that because of the nearly layer parallel orientation of these

O-H bonds, their vibrations are relatively unaffected by interlayer cations. Comparable to what

happens with the N- and I-band absorptions, changes in tetrahedral composition may give rise to

additional overlapping versions of V-band absorptions separated by about 10 cm^{-1}. An intense

series of overlapping interlayer H_2O-related absorptions around 3425 cm^{-1} overlap these weak V-

band absorptions in vermiculite. V-band absorptions at frequencies < 3600 cm^{-1} are

overwhelmed by these broad water absorptions and are difficult to detect in spectra of pure

vermiculite. Fortunately, most of the unexpanded and expanded vermiculite ore samples studied

are relatively Mg-rich so the strongest V-band absorptions occur at frequencies >3600 cm^{-1} and

are not entirely masked by interlayer water absorptions. For the unexpanded Libby GDS469

sample, V-band absorptions tend to gain intensity during vermiculization, but diminish during

cation exchange (bottom spectrum of Fig. 11), though this later change could be due to the

overwhelming spectral contribution of water absorbed during the K^+-exchange process.

Cation exchange can be used to determine which absorptions are from repulsed and non-

repulsed hydroxyls in the MIR region. An absorbance spectrum of ground, K^+-exchanged

vermiculite flakes illustrates the influence of K^+ saturation on the wavelength position of

hydroxyl vibrations. Addition of K^+ to interlayer sites reverses the progressive low-frequency

shift of OH absorptions resulting from vermiculization, back to higher frequencies, producing a

spectrum resembling that of hydrobiotite (compare bottom and upper middle spectra of Fig. 11).

Note that relatively weak ν_i and ν_k MgFe^{3+}[   ]OH V-band absorptions near 3620 cm^{-1} in the K^+-

exchanged vermiculite's spectrum all but disappear, whereas ν_f and ν_g repulsed Mg$_2$(Fe^{3+}, Al,

Ti)OH I-band absorptions grow at the expense of their corresponding non-repulsed ν_h and ν_j

absorptions. Repulsed ν_a and ν_b Mg$_3$OH N-band absorptions also grow relative to their

corresponding non-repulsed ν_d and ν_e absorptions.

Mid-infrared cation-OH bends couple with OH stretches to form the NIR combination

absorptions that can be used to differentiate among the sources of vermiculite ore. Figure 12

shows deconvolution models of the out-of-plane bend absorptions in the 580 to 900 cm^{-1} (11 to

17.2 μm) region and in-plane bend absorptions in the 400 to 680 cm^{-1} (14.7 to 25 μm) region for

handpicked, ground flakes of phlogopite, hydrobiotite, and vermiculite from the unexpanded

Libby GDS469 sample (see vibrational assignments in Table 5). Extensive overlap between

these two varieties of cation-OH bend absorptions, with the added complexity of overlapping Si-

O-Al, Si-O-Mg, Al-O-Al bend absorptions (Jenkins 1989; Papin et al. 1997), makes

deconvolution modeling more challenging than in the OH stretch region. It is interesting that the

talc Mg-OH bend absorption at 669 cm^{-1} (Russel and Farmer 1970) is located at nearly the same

frequency as the vermiculite δ_e non-repulsed out-of-plane Mg-OH bend absorptions at 674 cm^{-1}

(Fig. 12 and Table 5), a relationship consistent with the "unperturbed" hydroxyl concept

discussed above. Apparently, the repulsed version of this out-of-plane bend absorption (δ_a) is

present near 591 cm^{-1} in spectra of phlogopite (Beran 2002). In a reversal of their relative

positions in the OH stretch region, the corresponding out-of-plane N-band bend absorptions

occur at lower frequencies near 600 cm^{-1}, the I-band bend absorptions occur at intermediate

frequencies near 710 cm^{-1}, and the V-band bend absorptions occur at higher frequencies near 860

cm^{-1}. Consistent with this reversed sequence, the non-repulsed out-of-plane δ_d and δ_e N-band

bend absorptions in vermiculite occur at lower frequencies (near 660 cm^{-1}) than does the

repulsed out-of-plane δ_f I-band bend absorption (at 710 cm^{-1}). Moreover, the deconvolution

model predicts that the strongest repulsed δ_a and δ_b Mg$_3$OH bend absorptions are in spectra of

phlogopite, whereas the strongest non-repulsed δ_d and δ_e Mg$_3$OH bend absorptions are in spectra

of vermiculite, with absorptions of intermediate strength in spectra of hydrobiotite. This is

consistent with their relative strengths in the OH stretch region.

Near-Infrared Overtone and Combination Absorptions. Near-infrared OH overtone

and combination absorptions of phlogopite, hydrobiotite, and vermiculite mimic the wavelength

sequence of their MIR fundamental absorptions, but are an order of magnitude weaker.

Hydroxyl overtone absorptions cluster in three general regions: the1.38-µm group is composed

of overlapping N-bands, the 1.40-µm group is composed of overlapping N- and I-bands, and the

1.42-µm group is composed of overlapping I- and V-bands (Figs. 10a and 13). Spectra of

phlogopite are dominated by repulsed N- and I-band absorptions. Spectra of hydrobiotite are

dominated by repulsed and non-repulsed N-, I- and V-band absorptions, whereas spectra of

vermiculite are dominated by non-repulsed I- and V-band absorptions. A set of intense, broad

interlayer H_2O-related absorptions covering the spectral range from 1.39 to 1.54 µm overlaps

nearly all of the weaker OH overtone absorptions in spectra of hydrobiotite and vermiculite

(middle and bottom spectra of Fig. 13). Their vibrational assignments and wavelength positions

are given in Table 6. The first OH stretch overtones are usually less than double their

fundamental frequencies due to anharmonic vibration, and in spectra of phlogopite, hydrobiotite,

and vermiculite, the overtone absorptions are shifted an average of 166 cm^{-1} (2σ = ±6 cm^{-1})

toward lower frequencies (i.e., longer wavelengths) than would be predicted for perfect harmonic

vibration. This value is close to the 168 cm^{-1} anharmonicity constant derived by Madejova et al.

(2000) for OH overtone absorptions in montmorillonite. Unlike the OH overtones, the

combination vibrations are less anharmonic with vacancy bands shifted an average of 33 cm^{-1}

(2σ = ±5 cm^{-1}), repulsed N-band shifted 22 cm^{-1} (2σ = ±4 cm^{-1}), and non-repulsed bands shifted

1 cm^{-1} (2σ = ±8 cm^{-1}) toward lower frequencies relative to their predicted positions for perfect

harmonic vibration.

Although the NIR combination absorptions arise from MIR cation-OH out-of-plane and

in-plane bend-plus-stretch vibrations, their wavelength sequence is reversed from that of the OH

overtone region. This results in composite absorptions in three general regions: the 2.3-μm

group is composed of overlapping repulsed and non-repulsed I-bands, and non-repulsed c_e N-

band; the 2.32-μm group is composed of overlapping repulsed N-bands, and non-repulsed c_d N-

band; whereas the 2.38-μm group is composed of both these groups of vibrations arising from

the intrinsically weaker in-plane bend-plus-stretch combinations (Figs. 10b and 14). Note that

the 2.30-μm absorption, formed mostly by the non-repulsed c_e absorption in vermiculite, is

shifted well away from its matching non-repulsed c_d absorption, and consequently forms a

separate absorption. This shift is most noticeable because of the 42 cm^{-1} separation of their

corresponding non-repulsed out-of-plane δ_e and δ_d bend absorptions, twice the separation of the

corresponding repulsed δ_b and δ_a bend absorptions, and likely caused by larger differences in

hydrogen bonding to apical tetrahedral oxygens opposite interlayer water (see the bottom

spectrum of Fig. 12). Deconvolution modeling was not able to separately resolve the relatively

weak c_i V-band absorption because it is likely overlapped by much stronger non-repulsed I-band

absorptions c_h and c_j. Modeling did resolve the c_k absorption at 2.245 μm, isolated from the rest

of the combination absorptions at a relatively shorter wavelength (Fig. 14). Hence, the sequence

of absorptions in the NIR combination region starts with V-bands, then I-bands, followed by N-

bands in increasing wavelength (decreasing frequency) order. Absorptions at wavelengths

longward of 2.45 μm in spectra of phlogopite might be combinations of OH stretches with

framework vibrations (top spectrum in Fig. 14 with vibrational assignments given at the bottom

of Table 6). Hydroxyl absorptions do not overlap as much in the overtone region, relative to

their corresponding combination absorptions, because the overtones have nearly double the

wavelength separation of their fundamental absorptions whereas the separation between

combination absorptions is additive, relative to the separation between their fundamentals. Add

to this extensive overlap between combination absorptions derived from overlapping sets of out-

of-plane and in-plane bends and stretch fundamentals, and the deconvolution of individual

combination absorptions becomes quite challenging. Those interested in a comparison of the

spectral properties of vermiculite and saponite for remote sensing purposes can read more in the

appendix section devoted to this subject.

Spectroscopy of Unexpanded and Expanded Vermiculite Ores. Differences among

MIR spectra of vermiculite ores from the four major historical sources result from variations in

their composition and the relative proportions of their mica constituents. Figure 15a shows

deconvolution models for the OH stretch fundamental region in spectra of the selected

unexpanded ore samples. The repulsed N-band composite absorption near 3710 cm^{-1} dominates

spectra of the unexpanded samples, consistent with results of XRD analysis (i.e., Fig. 7), that

hydrobiotite is a major component relative to vermiculite. The asymmetry of the 3710, 3675,

and 3620 cm^{-1} absorptions, seen most clearly in the spectrum of the unexpanded Zonolite® 4

sample from Enoree (second spectrum from top in Fig. 15a), supports the interpretation that

these are composite absorptions composed of overlapping individual absorptions. Overlapping

non-repulsed N- and I-band absorptions near 3675 cm^{-1} are intermediate in their combined

strength except in the unexpanded Palabora sample (bottom spectrum of Fig. 15a), where they

form a composite absorption nearly as intense as the repulsed N-band composite absorption near

3720 cm^{-1}. The overlapping non-repulsed I- and V-band absorptions near 3620 cm^{-1} are weakest

in the spectrum of the Palabora sample, of intermediate strength in the spectra of the Libby

sample, and strongest in the spectra of the Enoree and Louisa samples. Based on box and

whisker diagram comparisons (Fig. 5d) and ANOVA tests (Table A4), the selected unexpanded
Enoree and Libby samples contain more total Fe, whereas the selected unexpanded Palabora
sample contains relatively less. Oxidation of Fe^{2+} to Fe^{3+} during vermiculization may lead to the
formation of additional cation clusters with vacancies, and as a consequence, the development of
stronger V-band absorptions. The selected unexpanded Palabora ore sample also has the least
total Al (Figs. 5c) so its spectrum has only weak V-bands, with non-repulsed ν_d and ν_e N-bands
contributing most to the overall strength of its 3675 cm^{-1} composite absorption.

The ν_a and ν_b absorptions in the unexpanded Palabora ALB5SA00 sample are shifted
toward higher frequencies (ν_a and ν_b = 3721 and 3712 cm^{-1}, respectively), than are the
corresponding absorptions in spectra of the other selected unexpanded ores (e.g., the Zonolite® 4
sample's spectrum with ν_a and ν_b = 3716 and 3702 cm^{-1}, respectively). This may be due to the
Palabora sample's low Al content. According to Robert and Kodama (1988), increasing total Al
in trioctahedral micas shifts their N- and I-band absorptions to lower frequencies. As mentioned
earlier, this Palabora sample does not have enough Si and Al to fill its tetrahedral layer and likely
has about 4% tetrahedral Fe^{3+} and no octahedral Al. Because Fe^{3+} is a relatively large cation, it is
possible that its substitution into the tetrahedral site in place of Al causes the apical tetrahedral
oxygen to keep relatively more of its electronic charge, which also results in a shorter O-H bond
and hence the formation of a 3739 cm^{-1} ν_2 absorption. This may explain why the spectrum of the
Palabora sample, the only ore with significant tetrahedral Fe^{3+} based on compositional and
Mössbauer comparisons, has this absorption (Fig. 15a). X-ray diffraction analysis of the
Palabora sample shows it has normal {200} basal spacing, thus confirming that it does not have

collapsed interlayers that could lead to the formation of an absorption near this wavelength

position as discussed below.

In general, the samples of unexpanded and expanded Palabora ore contain more

hydrobiotite and less vermiculite than the other selected unexpanded ore samples, causing their

combination absorptions to resemble those of phlogopite with a stronger 2.38-μm composite

absorption (see XRD pie diagrams in Fig. 7 and compare the spectrum in Fig. 9b to those in Fig.

10b). Furthermore, the 2.30-μm absorption in spectra of unexpanded Palabora ores is not as

strong as in spectra of the other unexpanded ores due to a lower level of non-repulsed hydroxyl

because the Palabora ores contain less vermiculite.

Heating and accompanying expansion cause profound changes in the spectral signatures

of the vermiculite ores with greater Al and Fe contents. Figure 15b shows deconvolution models

for the OH stretch fundamental region of representative expanded vermiculite ores. Absorption

intensities change relative to those in spectra of the unexpanded ores. The $Mg_3OH_{repulsed}$

composite absorption at 3710 cm^{-1} shrinks to about half its original intensity in the expanded

Louisa and Enoree ores, while retaining its intensity in the expanded Libby and Palabora

samples, when compared to the strength of their 3675 cm^{-1} composite absorptions. Factors

contributing to this spectral decline include mechanical beneficiation of expanded ores and

expansion-related chemical changes in the vermiculite component of the ores in response to

collapse of their interlayers, as water is driven out and Fe^{2+} is oxidized. The expanded ore

samples are exfoliated commercial products that have likely undergone post-expansion sorting,

which selectively removes the non-expandable portions of the ores. This potentially includes

removal of non-expandable phlogopite-rich flakes, which mainly contribute to the 3710 cm^{-1}

40

composite absorption's intensity. Presumably, the expanded Libby and Palabora ore samples

have undergone the same post-expansion beneficiation, yet their 3710 cm^{-1} absorptions retain

their relative high intensity (Fig. 15b). This apparent inconsistency may indicate that

beneficiation is not the sole factor contributing to a reduction of the 3710 cm^{-1} absorption's pre-

expansion intensity, suggesting instead that differences in composition may be the principal

cause of spectral changes between expanded ores from the major historical sources.

There are several factors that influence the overall intensity of the 3710 cm^{-1} composite

absorption. Phlogopite's spectrum with its three repulsed ν_a, ν_b, and ν_c Mg$_3$OH absorptions

results in a more intense 3710 cm^{-1} composite absorption compared to that in spectra of

vermiculite, which is composed of the ν_a and ν_b absorptions (i.e., compare the first and third

spectra in Fig. 11). Although fewer in number when compared to the number of K$^+$ cations in

phlogopite on a unit cell basis, water-coordinated interlayer cations (i.e., Mg, Ca, and Na) in

vermiculite may locally repulse adjacent hydroxyl hydrogens to nearly the same degree as K$^+$,

thus contributing to the overall intensity of the 3710 cm^{-1} composite absorption (i.e., its intensity

is not solely a function of the ore's phlogopite content and phlogopite component in its

hydrobiotite). For example, the ν_b absorption at 3708 cm^{-1} is the most intense N-band absorption

in the unexpanded Louisa ore, but the weakest one in the corresponding expanded ore (i.e.,

compare top spectra of Figs. 15a and b), suggesting its loss of intensity may be due to heat-

driven changes in hydroxyl hydrogen repulsion by water-coordinated interlayer cations. This

also may explain why the Mg$_3$OH$_{repulsed}$ composite absorption at 3710 cm^{-1} is always more

intense than its neighboring non-repulsed N- and I-band composite absorption centered near

3675 cm^{-1} in the unexpanded samples (Fig. 15a), even when up to a third of the sample is

composed of vermiculite (Fig. 7). Serratosa et al. (1970) proposed that the absorption near 3740 cm^{-1}, which forms as vermiculite ore is heated (Fig. 15b), may be caused by strong repulsion of hydroxyl hydrogen in Mg_3OH cation clusters, as interlayer cations move into 12-fold coordination sites adjacent to the tetrahedral layer, to neutralize charge as interlayer water is driven off. However, Kawano and Tomita (1991) used X-ray electron density curves to show that cations remain in the interlayers of vermiculite even after thermal dehydration. Perhaps when interlayer divalent cations (e.g., Mg^{2+} and Ca^{2+}) are freed from their hydration shells during heating, they may then more strongly repulse adjacent hydroxyl hydrogens due to their higher charge compared to that of K^+. Thus, formation of the ν_1 absorption at 3741 cm^{-1}, as a consequence of interlayer collapse and loss of interlayer cation hydration shells, would reduce the intensity of the 3710 cm^{-1} composite absorption. It is also possible that heating preferentially dehydroxylates phlogopite and its component in hydrobiotite in the Louisa and Enoree ores because of their higher Al content. There may be other heat-related effects that also contribute intensity to the ν_1 absorption as discussed below.

Heating vermiculite ore can lead to other reactions that can change the relative intensities of its spectral absorptions. Oxidation of Fe^{2+} in $Mg_2Fe^{2+}OH$ cation clusters weakens the ν_c absorption, at 3696 cm^{-1}, while, to some extent, strengthening the repulsed ν_f and ν_g I-band absorptions, at 3663 and 3654 cm^{-1}, respectively, by creating more $Mg_2Fe^{3+}OH$ clusters. This is most noticeable in the expanded Louisa sample (top spectrum of Figure 15b), where the ν_c absorption, originally present in spectra of the unexpanded Louisa sample (Fig. 15a), is completely eliminated and repulsed I-band absorptions are strengthened. The ν_h non-repulsed I-band absorption, in particular, also gains strength from oxidation of Fe^{2+}, and along with the

appearance of the ν_3 absorption, helps create the distinctive tail on the low frequency end of the

OH stretch absorption envelope near 3630 cm^{-1} (top two spectra of Fig. 15b). As mentioned

above, the absorption coefficient of hydroxyl associated with I-band cation clusters is twice that

of N-band clusters, so the intensity of the I-band absorptions should double relative to the

decrease in the N-band absorptions in these spectra during heat-induced expansion. Specifically,

Fe^{2+} oxidation and simultaneous collapse of the interlayers during heating, reduces the intensity

of the 3710 cm^{-1} composite absorption relative to the ν_f and ν_g I-band absorptions in the

spectrum of the expanded Louisa sample (compare top spectra of Figs. 15a and b). This intensity

loss is mirrored by a proportional decrease in the intensity of the corresponding 1.38-μm N-band

overtone composite absorption.

Oxidation of Fe^{2+} in mica likely requires the deprotonation or dehydroxylation of one of

the two hydroxyl groups associated with it, leading to an overall reduction in all OH-related band

intensities (Farmer et al. 1971; Farmer 1974; Sanz et al. 1983). Deprotonation of hydroxyl can

result in a net loss of local positive charge, causing surrounding cation clusters to hold their

remaining hydrogens more tightly, potentially shifting their OH vibrations to higher frequencies,

but simultaneously creating vacancy clusters with vibrations at lower frequencies. In contrast,

dehydroxylation can result in a net loss of local negative charge, causing surrounding cation

clusters to hold their hydrogens less tightly, potentially shifting their OH vibrations to lower

frequencies. Farmer et al. (1971) used electron microscopy and electron diffraction to document

the formation of crystalline and amorphous iron hydroxides in the interlayers of vermiculite they

formed by exposing Fe-phlogopite to oxidizing agents Br$_2$ and H$_2$O$_2$ in lab experiments. They

attribute formation of these interlayer Fe-phases as a response to ejection of Fe^{3+} created by

oxidation of octahedral Fe^{2+}. This oxidation process creates cation clusters with vacancies that

dehydroxylate at 300 to 400 °C, leaving a "residual" absorption at 3645 cm^{-1} in spectra of

vermiculites with low iron content, which they attribute to $Mg_2Fe^{3+}OH$. The ν_3 absorption

observed in spectra of the expanded ores from Louisa and Enoree, has a similar position at 3647

cm^{-1} (top two spectra of Fig. 15b). This absorption is weakly present in the spectrum of the

expanded Libby sample, but based on modeling, is not detectable in the spectrum of the

expanded Palabora sample (bottom two spectra of Fig. 15b). The presence of octahedral Fe^{3+} in

the unexpanded ore samples (Table 2 and Fig. 6), but absence of a 3647 cm^{-1} absorption in

spectra of them (all four spectra in Fig. 15a), suggests this $Mg_2Fe^{3+}OH$ vibrational assignment is

incorrect. It is more likely that the $Mg_2Fe^{3+}OH$ vibration forms absorptions unresolved from

those of Mg_2AlOH at 3663 and 3654 cm^{-1} at the 4 cm^{-1} spectral resolution of our measurements

(see ν_f and ν_g assignments in Table 5).

An alternative explanation for the origin of the ν_3 3647 cm^{-1} absorption is needed, given

the importance of its corresponding combination absorption in differentiating between

vermiculite ore sources as discussed in more detail below. The expanded Enoree ALB22SC00

sample has the most intense ν_3 absorption of the representative expanded ores, so a split of it was

K^+ exchanged and measured with XRD. Resulting K^+ saturation caused the sample's vermiculite

interlayers to collapse causing the vermiculite {002} reflection to appear at 10Å. If any

hydroxyl interlayers were present, upon ethylene glycolation, those layers would expand and a

portion of the vermiculite in the sample would develop a reflection at 11.2Å. No expansion was

observed after glycolation, indicating that hydroxyl interlayers are not present. A spectrum of

this K^+-exchanged split shows that the ν_1 3741 cm^{-1} repulsed N-band absorption is eliminated,

44

along with its non-repulsed ν_h and ν_j I-band absorptions, likely due to replacement of migrated

interlayer cations and residual interlayer water by K^+ (i.e., compare top and bottom spectra of

appendix Fig. A5). This is in contrast to the ν_3 3647 cm^{-1} absorption, which retains its original

intensity in the K^+-exchanged split relative to the ν_f and ν_g absorptions, indicating it has spectral

properties similar to these repulsed I-band absorptions or is a V-band absorption.

A spectrum of an unexpanded Mg-rich VTx-1 vermiculite from Llano, Texas, has a

similar 3648 cm^{-1} absorption, attributed to a MgAl[ ]OH cation cluster vibration based on K^+

exchange, spectral polarization, and deuteration experiments (see appendix discussion and

appendix Figs. A6 to A8). Electron probe microanalysis of this Mg-rich vermiculite indicates it

has octahedral Al but is relatively Fe-poor (appendix Table A5). Conversion of Mg_2AlOH to a

vacancy cluster could be accomplished by heat-induced deprotonation of a neighboring cation

cluster that then more strongly attracts its once mutually shared Mg, resulting in a MgAl[ ]OH-

like vibration shifted to the 3647 cm^{-1} frequency. This deprotonation mechanism would also

preferentially weaken the 3710 cm^{-1} composite N-band absorption through loss of H^+ and

potentially shift absorptions to higher frequencies (i.e., forming the 3741 cm^{-1} ν_1 absorption and

potentially a new $Mg_3OH_{non-repulsed}$ absorption that overlaps but is unresolved from the 3696 cm^{-1}

ν_c absorption). This heat-induced deprotonization mechanism is supported by the absence of a

3647 cm^{-1} absorption in the spectrum of the expanded Palabora GDS918 ore (bottom spectrum in

Fig. 15b), particularly because its corresponding unexpanded ALB5SA00 ore has no octahedral

Al with which to form Mg_2AlOH cation clusters (Table 2). In contrast, the unexpanded Enoree

Zonolite® 4 ore has plentiful octahedral Al consistent with the existence of Mg_2AlOH cation

clusters and presence of a strong 3647 cm^{-1} absorption in its corresponding expanded

ALB22SC00 ore (second spectrum from top in Fig. 15b).

Vermiculite Source Determination

      Source identification using the 1.38/2.32-µm band depth ratio. The compositional

and mineralogical variations discussed above are also expressed as changes in the relative depths

of the overtone and combination absorptions in NIR reflectance spectra of expanded ore from the

four major historical sources. Ratios of the continuum-removed band depths of the 1.38- and

2.32-µm composite absorptions in spectra of expanded samples can be related directly to their

sources. Figure 16 is a summary diagram of the band-depth-ratio values for the 52 expanded ore

samples. The diagram is empirically divided into five provenance fields: Louisa,

Enoree/Jiangsu, Libby, Mixtures, and Palabora according to 1.38/2.32-µm band-depth-ratio

values. Symbol shape for each sample is based on its provenance as determined by EPMA or

independent documentation of its source (see individual sample descriptions in Swayze et al.,

2018). Absorption band-area ratios could also be used in place of band-depth ratios to

differentiate among vermiculite ore sources, but they are computationally more intensive.

      The reason a simple 1.38/2.32-µm band depth ratio allows determination of provenance is

based on the observation that expanded ores contain different proportions of phlogopite,

hydrobiotite, and vermiculite depending on their source. This holds true even though many

samples, likely spanning decades of ore extraction at a given mine, were included in this study,

suggesting site-specific compositional consistency in the altered parent materials, weathering

climate, and beneficiation processes. Although the 1.38-µm composite absorption is sensitive to

the total phlogopite content (i.e., discrete phlogopite and the phlogopite component of

46

hydrobiotite), the 2.32-μm composite absorption is relatively insensitive to variations in the

relative proportions of the three mica types. In effect, the depth of the 2.32-μm composite

absorption represents the "total" mica present in the sample against which the spectral

contribution from its phlogopitic content can be scaled. In particular, the 1.38-μm composite

absorption is composed of overlapping repulsed o_a and o_b N-band overtone absorptions that are

strongest in phlogopite and weakest in vermiculite (Fig. 13). Two of phlogopite's and one of

vermiculite's strongest OH-stretch-plus-out-of-plane-bend vibrations give rise to three

overlapping combination absorptions that compose the 2.32-μm composite absorption. The

components of this composite absorption, the repulsed c_a and c_b and non-repulsed c_d combination

absorptions, are nearly coincident in wavelength, so as the c_a and c_b absorptions weaken with

decreasing phlogopitic content, the c_d absorption strengthens with increasing vermiculite content

(Fig. 14), keeping the overall depth of the 2.32-μm composite absorption nearly constant as the

proportions of the three micas vary in a given expanded ore sample.

The effectiveness of using the 1.38-μm absorption to differentiate between vermiculite

ore sources is evident in a spectral comparison of unexpanded ore samples from Palabora and

Louisa. The unexpanded Palabora ALB5SA00 sample contains a larger proportion of phlogopite

as a component in hydrobiotite (~46 wt%) than does the unexpanded Louisa ALB1VA00 sample

(~34 wt%), which contains a significant portion of vermiculite. This contrast extends to spectra

of their corresponding expanded ores, making the 1.38/2.32-μm band depth ratio larger for

expanded Palabora samples and smaller for expanded Louisa samples. Evidently, expanded

Libby ore contains more phlogopitic content, on average, than does expanded Enoree ore (i.e.,

based on the distribution of their sample points in Fig. 16), perhaps due to the presence of

phlogopite flakes not removed by post-expansion beneficiation. In this way, the 1.38/2.32-μm

band depth ratio functions to spectrally separate expanded ores according to their mineralogy,

which is directly related to their respective sources. Relatively strong repulsed N-band

absorptions contribute to high values of the 1.38/2.32-μm band depth ratio in spectra of the

expanded Palabora ores (Fig. 16). In contrast, intrinsically weak repulsed N-band absorptions,

which are overwhelmed by stronger overlapping Fe-electronic absorptions, keep values of the

1.38/2.32-μm band depth ratio low in spectra of the expanded Louisa ores. Spectral properties of

expanded Libby and Enoree ores produce intermediate 1.38/2.32-μm band-depth-ratio values.

There are differences between transmission and reflectance measurements of vermiculite

ore that can influence the magnitude of the 1.38/2.32 band depth ratio. Specifically, the

continuum-removed 1.38-μm composite absorption in expanded ores is weaker in reflectance

than in transmission, relative to the other overtone absorptions, due to overlap with the long

wavelength wings of broad neighboring Fe-electronic absorptions. The widths of these broad

electronic absorptions are $\sqrt{2}$ greater in reflectance than in transmission (Clark and Roush 1984),

so they overwhelm the 1.38-μm absorption more in reflectance than in transmission (Fig. 17).

The long wavelength wings of these electronic absorptions extend to 2.15 μm in the expanded

Libby, Louisa, and Enoree ores (arrows in Figs. 9a, c, and d), but only to 1.82 μm in the

expanded Palabora ore (arrow in Fig. 9b). These broad electronic absorptions, which overlap the

narrower vibrational 1.38-μm composite absorption, are less intense in low-Fe expanded ores,

such as those from Palabora (Fig. 5d), thus allowing more photons to scatter out relative to those

absorbed. This effectively raises the level of the local continuum resulting in a deeper 1.38-μm

composite absorption. Unlike expanded ores from the three other sources, Palabora ore's 1.38-

µm composite absorption is shifted to a slightly shorter wavelength because of its relatively

lower Al content, so the overlap by its neighboring, relatively strong 1.40-µm composite

absorption, is smaller and consequently has little effect on its calculated depth.

Detection of impurities using the 1.40/1.42-µm band depth ratio. As discussed above,

direct spectral identification of amphibole, talc, and/or serpentine contents at trace levels (<5

wt%) in expanded ore is difficult, but detection of their presence can be done indirectly. These

impurity phases have OH-stretch-overtone absorptions that can contribute intensity to an

expanded ore's 1.40-µm composite absorption. In contrast to micas in the ores, spectra of these

impurities lack a 1.42-µm absorption (dotted vertical line in Fig. 8 inset), so their presence can be

detected by ratioing the continuum-removed band depths of an expanded ore's 1.40- and 1.42-

µm composite absorptions. The black sigmoidal curve in Figure 16 was drawn to pass through

symbols whose samples contain only minute levels of amphibole (i.e., at most a few individual

microscopic amphibole particles detected by SEM in the sink fractions of expanded ores

GDS327, GDS628, GDS631, GDS650, GDS906, and GDS918; see individual sample

descriptions in Swayze et al., 2018). The curve defines the threshold value of the 1.40/1.42-µm

band depth ratio above which phases with 1.40-µm absorptions other than the micas, contribute

to the overall strength of the observed OH composite absorption. This non-detect curve is lowest

in the Louisa, Enoree, and Libby provenance fields because spectra of expanded samples from

these sources have deeper 1.42-µm composite absorptions than spectra of expanded Palabora

samples. Note that the 1.42-µm composite absorption is composed of overlapping non-repulsed

$Mg_2(Fe^{3+}, Al, Ti)OH$, $MgAl[\ ]OH$, and $MgFe^{3+}[\ ]OH$ overtone absorptions. Because the ν_3

$MgAl[\ ]OH$ V-band absorption is strongest in the spectrum of the expanded Enoree

ALB22SC00 sample (Fig. 15b), its overtone absorption will contribute more intensity to the

1.42-μm composite absorption. Likewise, the expanded Louisa GDS847 sample has 1.42-μm

contributions from overtones of these non-repulsed I- and V-band OH stretch absorptions in the

long wavelength "tail" (top two spectra of Fig. 15b). The relative strength of these I- and V-

band overtone absorptions requires the impurity non-detect curve to be at lower 1.40/1.42-μm

band-depth-ratio values for the expanded Louisa and Enoree samples compared to higher band-

depth-ratio values for expanded Libby and Palabora samples (Fig. 16).

The expanded Louisa GDS847 sample has a transmission spectrum with evidence of a

talc absorption (i.e., sharp absorption in the top spectrum of Fig. 15b). Because talc has an

Mg_3OH stretch fundamental at 3677 cm^{-1} (2.720 μm; Parry et al. 2015), its overtone absorption

contributes to the depth of the expanded sample's composite 1.40-μm overtone and 2.32-μm

combination absorptions (Fig. 8). The spectrum of talc does not have a 1.38-μm absorption (see

leftmost vertical line in Fig. 8 inset), consequently, the presence of this impurity could

potentially shift the 1.38/2.32-μm band-depth-ratio value of an ore's spectrum toward the left in

Figure 16. Likewise, spectra of amphibole and serpentine have, at most, only weak absorptions

near 1.38-μm, but have intense absorptions in the 2.32-μm region; hence, the presence of either

in an expanded ore could potentially shift its 1.38/2.32-μm band-depth-ratio value to the left.

One expanded ore in particular can help test this potential shift. Sample ALB22SC00, from

Spartanburg in the Enoree district of South Carolina, has ~5 wt% talc content, prior to removal

by hand for measurement of the spectra shown in this study, giving it the highest 1.40/1.42-μm

band depth ratio among the 52 expanded ore samples, yet its 1.38/2.32-μm band-depth-ratio

value still plots in the correct provenance field (i.e., green triangle at the top of the

Enoree/Jiangsu provenance field in Fig. 16). Therefore, impurities up to this trace level are

unlikely to shift sample points into incorrect provenance fields. Note that the presence or

absence of talc was not tested as an indicator of a vermiculite ore's source, as it is not present in

ore samples from Libby, examined with XRD, and inconsistently present in ores from the other

major historical sources, and because spectroscopy may not dependably differentiate between it

and amphibole at trace levels in expanded samples (see details of analytical examinations in

Table 1).

When an expanded ore's 1.40/1.42-μm band-depth-ratio value plots just above the

contaminant non-detect line on the provenance diagram, it does not necessarily mean it contains

proportionately fewer amphibole, talc, and/or serpentine particles. A sample of expanded ore

from an attic in Silver Springs, Maryland, has numerous sodic-calcic elongate amphibole

particles, but its 1.40/1.42-μm band-depth-ratio value plots near the impurity non-detect curve

(i.e., lowest pink circle in the Libby provenance field of Fig. 16). The fine-grained nature of the

amphibole in this sample causes it to have a weaker 1.40-μm absorption, which produces a

relatively small band-depth-ratio value, yet it still contains abundant respirable elongate

amphibole particles. Although the degree of elongation of amphibole and serpentine particles in

an expanded ore is not directly measurable using the 1.40/1.42-μm band depth ratio, this spectral

parameter varies with the size of impurity particles. See the appendix for a more in-depth

discussion of the grain-size distribution of impurities in fine- and coarse-grained expanded

vermiculite ores.

Source identification using the 2.24/2.38-μm band depth ratio. Compositional

variations among expanded ores from different sources also influence the relative intensity of the

51

2.24- and 2.38-μm composite absorptions. Figure 18 is a provenance diagram empirically

divided into six provenance fields: Louisa, Enoree, Jiangsu, Libby, Mixtures, and Palabora

according to 2.24/2.38 - 1.38/2.32-μm band depth ratios. Combining both band depth ratios in a

single plot allows separation of expanded ore samples into their individual provenance fields.

The 2.24-μm composite absorption in expanded ores is primarily composed of

overlapping V-band combination vibrations. Figure 19 compares the OH stretch and cation-OH

bend fundamental regions for spectra of unexpanded and expanded vermiculite ores from

Enoree. The ν_3 MgAl[ ]OH V-band stretch absorption at 3647 cm^{-1} and its corresponding out-

of-plane δ_3 bend absorption at 838 cm^{-1} are both noticeably missing from the spectra of the

unexpanded Zonolite$^®$ 4 sample (see vertical arrows in Fig. 19). When present, these

fundamentals should give rise to a combination absorption at 4452 cm^{-1} (2.246 μm) with a 33

cm^{-1} anharmonicity correction. Figure 20a shows absorptions in spectra spanning the NIR

combination region for the same samples (from Fig. 19) deconvolved into individual Gaussian

absorptions. The unexpanded Zonolite$^®$ 4 sample's spectrum shows a single absorption forming

a shoulder at 4450 cm^{-1} (2.247 μm), which likely represents overlapping unresolved c_i and c_k

MgFe^{3+}[ ]OH V-band combination absorptions on the shorter wavelength (higher frequency)

side of more intense I- and N- band absorptions. In contrast, the deconvolved spectrum of the

expanded ALB22SC00 sample shows a c_3 absorption overlapping less intense c_i and c_k

absorptions. Together, they produce a distinctly stronger peak at 2.245 μm (4454 cm^{-1}). Figure

20b displays the same combination region for these samples in reflectance, with a stronger 2.24-

μm composite absorption and a weaker 2.38-μm composite absorption in the spectrum of the

expanded ALB22SC00 ore compared to those in the spectrum of the unexpanded Zonolite$^®$ 4

ore. The 2.38-µm composite absorption weakens in spectra of the expanded ore as some

vermiculite, and its component in hydrobiotite, is preferentially destroyed by heating, weakening

the in-plane-bend-plus-stretch c_e' and c_d' combination absorptions. The same mechanism also

weakens the 2.3-µm composite absorption due to reduction in the intensity of the corresponding

out-of-plane-bend-plus-stretch c_e and c_d combination absorptions (Fig. 20b). With these

relationships in mind, reflectance spectra of expanded ores in Figure 9 are reexamined, to see

how the intensities of these composite absorptions compare to those in spectra of expanded ores

from the three other major historical sources.

The 2.38-µm composite absorption in expanded vermiculite ore is due primarily to

repulsed and non-repulsed N-band combination absorptions arising from cation-OH in-plane

bend-plus-stretch fundamentals. In essence, it is a repeat of the 2.32-µm composite absorption,

but at a longer wavelength, with its depth controlled by the proportion of the three micas in a

given sample. In spectra of phlogopite, the repulsed c_b' and c_a' N-band combination absorptions

overlap, creating a relatively sharp 2.38-µm composite absorption (top spectrum in Fig. 14). As

the vermiculite content increases, the 2.38-µm composite absorption weakens because the non-

repulsed c_e' and c_d' N-band combination absorptions are farther apart in wavelength, perhaps due

to differences in the strength of hydrogen bonding to adjacent tetrahedral oxygens. This

separation causes the shorter wavelength c_e' absorption to form a weak shoulder on the more

intense 2.32-µm composite absorption. As a consequence, increasing the vermiculite component

in an expanded ore simultaneously weakens its 2.38-µm composite absorption and strengthens its

2.32-µm composite absorption (e.g., compare the combination region of the vermiculite-poor

Palabora GDS918 ore's spectrum to the vermiculite-rich Enoree ALB22SC00 sample's spectrum

in Figs. 9b and d, respectively). Therefore, expanded ore samples that have greater Al, Fe, and vermiculite contents, like those from Louisa and Enoree (see Figs. 5c and d), have spectra with stronger 2.24- and weaker 2.38-μm composite absorptions resulting in higher 2.24/2.38-μm band-depth-ratio values (Fig. 18).

Accuracy of spectral methods for determining ore sources and impurity contents. Band depth ratios are spectral indicators of mica composition and their proportions; the classifications based on them can be compared to check source determinations for consistency. For instance, the Louisa and Enoree provenance fields are situated on the upper left side of the 2.24/2.38 - 1.38/2.32-μm depth band ratio diagram, well away from the Libby provenance field (Fig. 18). This allows sample points that otherwise might fall on or close to the Enoree – Libby boundary on the 1.38/2.32-μm band-depth-ratio diagram (Fig. 16), to be more confidently placed in the correct provenance field. Complementary use of both band-depth-ratios values in a single diagram allows recognition of most mixtures made with vermiculite ores from the four major historical sources and differentiates between Enoree and Jiangsu expanded ores. It is worth noting that the relatively narrow, adjacent Louisa and Enoree provenance fields on the 2.24/2.38 – 1.38/2.32-μm band-depth-ratio diagram suggests their ores have similar compositions, and that confident spectral separation between them remains challenging.

False positive determinations based on the band-depth-ratio method can occur when mixtures of non-Libby ores mimic the spectral signature of the Libby ore. For instance, the expanded GDS629 sample used for packing chemicals has a 1.38/2.32-μm band-depth-ratio value that plots in the Libby provenance field (gray hexagon symbol in Fig. 16), but EPMA shows a match to Palabora and Enoree ores (see the GDS629 sample description in Swayze et

al., 2018). This mixture of expanded ores can be spectrally differentiated from Libby ore by

plotting the wavelength position of its 2.24-μm composite absorption against its 2.24/2.38-μm

band depth ratio (Fig. 21). Because the precise position of the 2.24-μm composite absorption is

controlled by composition, expanded samples from different sources exhibit a range of

wavelength positions for this absorption. This composite absorption is near 2.241 μm in the

spectrum of the single Palabora sample in which it was detected and near 2.248 μm in spectra of

two Enoree samples, suggesting that increased total Al (Fig. 5c) may cause the shift to longer

wavelengths. Despite overlap in the wavelength position of the 2.24-μm absorption in spectra of

expanded ores from Libby, Louisa, and Enoree, plotting the wavelength position of this

composite absorption against the 2.24/2.38-μm band depth ratio causes the false positive sample

value to plot outside of the Libby provenance field (i.e., outside of the light green box defined by

EPMA confirmed Libby samples). This false positive test can be performed in combination with

the spectral provenance determinations to identify mixtures of expanded ores that mimic the

Libby ore's spectral signature.

No false negative determinations, with regard to Libby, were found among the 52

expanded ore samples investigated. It is conceivable that a false negative source determination

(i.e., when a Libby sample's band-depth-ratio value plots in another provenance field) could be

made using these spectral methods on ore mixtures in which expanded ore from Libby is a minor

component. Therefore, samples that plot outside of the Libby provenance field on any of the

band-depth-ratio diagrams (Figs. 16, 18, or 21) will require alternative testing for the presence of

elongate amphibole and/or serpentine impurities.

55

Table 1 allows the side-by-side comparison of source determinations and detection of amphibole, talc, and/or serpentine impurities in the 52 expanded ore samples, whereas the third column in Table 7 summarizes errors in vermiculite ore source determinations. There is a one-to-one correspondence between the source identified by EPMA and that determined spectrally for all but three of the expanded ore samples. The first exception is the 1.38/2.32-μm band-depth-ratio value of the GDS651 sample from Enoree, which plots on the Louisa – Enoree provenance boundary (red triangle in Figs. 16 and 18). This sample's relatively weak 1.38-μm absorption is overwhelmed by strong electronic absorptions due to its relatively higher Fe and lower phlogopite contents. The second exception is the Palabora – Enoree ore mixture false positive, discussed above, which was resolved using the 2.24-μm absorption wavelength position diagram (Fig. 21). The third exception is the GDS327 sample, which has 3 EPMA points that plot in the Enoree provenance field compared to 26 that plot in the Palabora field (see the GDS327 sample description in Swayze et al., 2018), suggesting it contains a few percent Enoree ore. Spectral analysis indicated only the presence of Palabora ore, implying that ore from this source was spectrally dominant.

Table 7 also compares accuracies for the different amphibole, talc, and/or serpentine impurity detection methods used to search for amphibole, talc, and/or serpentine impurities in the expanded ore samples. XRD analysis was performed as an aid to identify the constituents of the sink fractions when macroscopic amphibole bundles were not obvious. This method had mixed success when used to identify the presence of these impurities in the bulk samples due to their low concentrations in some samples; therefore, although results from it are listed in Table 1, its accuracy is not listed in Table 7.

56

In general, the SED-EDS method found evidence of these impurities in expanded ore samples more consistently than did the MCM method alone. Interestingly, both methods were equally effective in finding elongate amphibole bundles in all 23 expanded Libby samples examined. Based on SEM-EDS examination, 67% of the "Mixtures" samples (i.e., most containing some Enoree ore) and about 63% of Enoree samples contain elongate amphibole particles, whereas only 40% of the Louisa samples contain prismatic to elongate amphibole particles. Only a single elongate amphibole particle was found in one of the eight Palabora samples examined (or 13% of total Palabora samples), after hours of SEM-EDS examination per sample. Because the 1.40/1.42-µm band-depth-ratio method only indicates the presence of amphiboles, talc, and/or serpentine and not their aspect ratio, it is more appropriate to compare its detection rate to that of the SEM-EDS "Any Shape" category. Doing so shows overall agreement between the two methods (i.e., results are within 33% of each other), which not surprisingly, is better than when compared to the SEM-EDS "Elongate" category, as not all samples contain elongated amphibole, talc, and/or serpentine. All 23 of the expanded Libby ore samples had spectral evidence of these impurities, based on the relatively large spread of their 1.40/1.42-µm band-depth-ratio values (Fig. 16). The spectral method consistently overestimates impurity levels relative to those of the SEM-EDS "Any Shape" method for expanded Enoree and Palabora samples. This may be a consequence of empirically placing the impurity detection threshold through the lower 1.40/1.42-µm band-depth-ratio values among the expanded samples, without the ability to simultaneously compensate for intra-source compositional variations that can cause values to move slightly up or down along this axis independent of their samples' impurity levels.

IMPLICATIONS

Results of this study show that reflectance spectroscopy can be an effective tool for determining the source of expanded vermiculite ores and assessing them for amphibole, talc, and/or serpentine impurities. According to SEM-EDS examination, the level of elongate amphibole impurities in expanded ores from the four major historical sources varies considerably, but follows a progressively decreasing trend where Libby >> Enoree > Louisa > Palabora. An SEM-EDS examination of expanded Palabora samples found only a single elongate amphibole fiber in 1 of 8 samples after hours of searching each sample. In contrast, numerous elongate amphibole bundles were found in all Libby samples. Taken as a whole, the analyses conducted for this study of expanded ore samples from the four major historical sources, rarely found significant quantities of elongate amphibole particles in samples other than those from Libby. Based on medical studies, there is general agreement that all expanded Libby ore is potentially hazardous, and by extending this study's results to expanded ores from the four major historical sources, then spectrally determining the source of an ore will provide enough information to make a remediation decision.

Expanded vermiculite insulation can be analyzed *in situ* using a portable spectrometer programmed to analyze spectra for appropriate absorption wavelengths and intensities to identify probable sources of the material. The selection of usable spectra for determining the origin of expanded ore, from all those collected, can be automated. Band depth calculations can also be automated if the wavelength locations of the spectral absorptions are standardized and the data have a signal-to-noise ratio high enough to allow accurate continuum endpoint placement and band-depth-ratio calculations. Software on the computer controlling the spectrometer could do

these tasks to determine an expanded ore's source and, by association, indicate its relative

amphibole, talc, and/or serpentine contents. This spectral identification procedure, herein

referred to as the Vermiculite SPectral Evaluation and Classification (VSPEC) method can also

be used in a laboratory setting to identify expanded ores from the four major historical sources

(e.g., for a coarse-grained ore, a single spectral measurement of an optically thick 20-cm

diameter pile of a bulk sample will suffice for source determination). It can be used to

potentially identify expanded ores from other sources (e.g., Australia, Brazil, China, Tanzania,

and Uganda) if representative samples with known origins are used to define their provenance

fields on the spectral band-depth-ratio diagrams. Additional details on the optimum number of

spectral measurements for provenance determination and necessary spectrometer resolution can

be found in the appendix.

The Zonolite Attic Insulation Trust was set up to aid home owners in understanding the

risks and to possibly obtain financial assistance in removing Zonolite insulation from their attics

(see http://www.zonoliteatticinsulation.com). To determine a Libby versus a non-Libby source

for expanded vermiculite ore, the trust currently uses a Ba compositional test based on Gunter et

al. (2005). Contaminants (eg., wood fiber) can dilute the Ba content of the vermiculite insulation

below the diagnostic 1500 ppm level producing false negative results (Millette and Compton

2015).

Limited observations suggest that minor levels of cellulose or fiberglass in expanded ores

do not spectrally interfere with the source analyses. The two attic insulation samples that

contained these additives (i.e., GDS649 and GDS460 in Figs. 1k and l, respectively) still yielded

diagnostic spectra, because these admixed materials are relatively bright in the NIR and the

reflectance spectra of these samples are dominated by the relatively darker expanded ore.

Additional tests are needed to determine at what concentration levels these materials start to

interfere. Dirt on expanded vermiculite ore caused by exposure to dust, mud (e.g., from mud

wasps), and construction materials (e.g., wallboard and nails) can lead to spectral interference,

but collection of spectra on expanded mica flakes from below the surface, at a number of spots,

may yield cleaner usable spectra. Small handheld battery-operated spectrometers with internal

light sources and built-in computers are now a reality. With appropriate precautions to prevent

contamination by potential elongate particles, the front of the spectrometer can be inserted

directly into the expanded ore to make a measurement.

For locations outside of Libby, Montana, remediation of vermiculite insulation usually

becomes an issue at the time houses or buildings are sold. A quarter of the attic insulation

samples analyzed in this study were not from Libby, making it potentially erroneous to assume

that all vermiculite attic insulation is from this source. Home inspectors currently deal with

vermiculite insulation by sending a sample in for PLM analysis or calling in an asbestos

inspector. As an alternative to sending samples to a lab for analysis, inspectors could use a

portable spectrometer to do *in situ* measurements themselves, in nearly the same time it takes to

collect a bulk sample for traditional lab analysis. Samples for laboratory analyses do not need to

be collected from an attic if the insulation is spectrally confirmed as expanded Libby ore.

Instead, a report can be generated and given to the owner while on site, along with information

on remediation scenarios. If the vermiculite insulation is not from Libby (i.e., its band-depth-

ratio value plots in a different provenance field) then a sample will need to be collected for

traditional lab analysis to determine if it contains an actionable level of elongate amphibole or

chrysotile. This spectral inspection scenario does not address all of the potential safety issues associated with its use; it is the responsibility of users to establish appropriate safety protocols.

ACKNOWLEDGEMENTS

REFERENCES

Antao, V.C., Larson, T.C., and Horton, D.K. (2012) Libby vermiculite exposure and risk of developing asbestos-related lung and pleural diseases. Current Opinion in Pulmonary Medicine, 18, 161-167.

Arguelles, A., Leoni, M., Blanco, J.A., and Marcos, C. (2010) Semi-ordered crystalline structure of the Santa Olalla vermiculite inferred from X-ray powder diffraction. American Mineralogist, 95, 126-143.

Atkinson, G.R., Rose, D., Thomas, K., Jones, D., Chatfield, E.J., and Going, J.E. (1982)
Collection, analysis, and characterization of vermiculite samples for fiber content and
asbestos contamination: Midwest Research institute (MRI), Task 32, Final Report
prepared for U.S. Environmental Protection Agency, Project 4901-A32 under EPA
Contract No. 68-01-5915, Washington, D.C., EPA0717, 69 p. 5 appendixes.

ATSDR: Agency for Toxic Substances and Disease Registry (2002) Public Health Assessment,
Libby Asbestos NPL Site, U.S. Department of Health and Human Services. Accessed:
2016-04-15. URL: http://www.atsdr.cdc.gov/NEWS/libby-pha.pdf

Badreddine, R., Grandjean, F., Vandormael, D., Fransolet, A.-M., and Long, G.J. (2000) An ^{57}Fe
Mössbauer spectral study of vermiculization in the Palabora Complex, Republic of South
Africa. Clay Minerals, 35, 653-663.

Bassett, W.A. (1959) The origin of the vermiculite deposit at Libby, Montana. American
Mineralogist, 44, 282-299.

Beard, M. E., Shaul, G. M., and Wilmoth, R.C. (2004) Research method for sampling and
analysis of fibrous amphibole in vermiculite attic insulation. U.S. Environmental
Protection Agency, Washington, D.C., EPA/600/R-04/004 (NTIS PB2004-102559), 27p.

Bellamy, J.M., and Gunter, M.E. (2008) Morphological characterization of Libby "six-mix"
amphiboles used in in vivo studies. Periodico di Mineralogia, 77:2, 75-82.

Belsky, A. J., Hellenbrandt, M., Karen, V. L., Lucksch, P. (2002) New developments in the
Inorganic Crystal Structure Database (ICSD): Accessibility in support of materials
research and design. Acta Crystallographica Section B, Structural Science, B58, 364-
369.

Beran, A. (2002) Infrared Spectroscopy of Micas. In Micas; Crystal Chemistry and Metamorphic
Petrology. Reviews in Mineralogy and Geochemistry, 46, 351-369.

Besson, G. and Drits, V.A. (1997) Refined relationships between chemical composition of
dioctahedral fine-grained mica minerals and their infrared spectra within the OH
stretching region: Part I: Identification of the OH stretching bands. Clays and Clay
Minerals, 45, 158-169.

Bishop, J.L., Murad E., and Dyar M.D. (2002) The influence of octahedral and tetrahedral cation
substitution on the structure of smectites and serpentines as observed through infrared
spectroscopy. Clay Minerals, 37, 617-628.

Boettcher, A.L. (1967) The Rainy Creek alkaline-ultramafic igneous complex near Libby,
Montana – I: Ultramafic rocks and fenite. Journal of Geology, 75, 526-553.

Brindley, G.W., Zalba, P.E., and Bethke, C.M. (1983) Hydrobiotite, a regular 1:1
interstratification of biotite and vermiculite layers. American Mineralogist, 68, 420-425.

Brown, B.M., and Gunter, M.E. (2003) Morphological and optical characteristics of amphiboles
from Libby, Montana U.S.A. by spindle stage assisted-polarized light microscopy.
Microscope, 51:3, 121-140.

Burns, R.G. (1993) Mineralogical applications of crystal field theory. Cambridge University
Press, Cambridge, Massachusetts, USA, 551p.

Bush, A.L. (1976) Vermiculite in the United States. In Eleventh Industrial Minerals Forum, p.
145-155. Montana Bureau of Mines and Geology Special Publication 74.

Bush, A.L. and Sweeney, J.W. (1968) Construction materials. In Mineral Resources of the
Appalachian Region, U.S. Geological Survey Professional Paper 580, p. 210-260.

63

Carter, J., Poulet, F., Bibring, J.-P., Mangold, N., and Murchie, S. (2013) Hydrous minerals on
Mars as seen by the CRISM and OMEGA imaging spectrometers: Updated global view.
Journal of Geophysical Research Planets, 118, 831–858, doi:10.1029/2012JE004145.

Chatfield, E.J., and Lewis, G.M. (1980) Development and application of an analytical technique
for measurement of asbestos fibers in vermiculite. In O. Johari, Ed., Scanning Electron
Microscopy, I., p. 329-340. SEM Inc., AMF O'Hare Chicago, Illinois.

Clark, R.N. (1993) SPECtrum Processing Routines User's Manual Version 3 (program
SPECPR), U.S. Geological Survey, Open File Report 93-595, 228 p. Accessed: 2015-07-
06.
URL:ftp://ftpext.cr.usgs.gov/pub/cr/co/denver/speclab/pub/tetracorder+specpr+libraries/d
istrib.04.2013.

Clark, R.N. (1999) Chapter 1: Spectroscopy of Rocks and Minerals and Principles of
Spectroscopy. In A.N. Rencz, Ed., Manual of Remote Sensing, p. 3-58. John Wiley and
Sons, New York.

Clark, R.N., and Roush, T. (1984) Reflectance spectroscopy: Quantitative analysis techniques for
remote sensing applications. Journal of Geophysical Research, 89, 6329-6340.

Clark, R.N., Hoefen, T.M., Swayze, G.A., Livo, K.E., Meeker, G.P., Sutley, S.J., Wilson, S.,
Brownfield, I.K., and Vance, J.S. (2003) Reflectance spectroscopy as a rapid assessment
tool for detection of amphibole from the Libby, Montana region (Online). U.S.
Geological Survey Open-File Report 03-128.

Clark, R.N., Swayze, G.A., Wise, R., Livo, E., Hoefen, T., Kokaly, R., Sutley, S.J. (2007) USGS
digital spectral library splib06a (Online). U.S. Geological Survey, Digital Data Series
DS-231.

Deer, W.A., Howie, R.A., and Zussman, J. (1965) Rock-Forming Minerals v. 3 Sheet Silicates,
270 p. Longmans, Green and Company, Ltd., London.

Deer, W.A., Howie, R.A., and Zussman, J. (1966) An Introduction to the Rock Forming
Minerals, 528p. John Wiley and Sons Inc., New York, N.Y.

Dixon, G.H., Doria, J., Freed, J.R., Wood, P., May, I., Chambers, T., and Desai, P. (1985)
Exposure assessment for asbestos-contaminated vermiculite. EPA 560/5-85-013, PB85-
183085, 102 p. U.S. Environmental Protection Agency, Washington, D.C.

Dyar, M.D. (1993) Mössbauer spectroscopy of tetrahedral Fe3+ in trioctahedral micas -
Discussion. American Mineralogist, 78, 665-668.

Dyar, M.D. (2002) Optical and Mössbauer spectroscopy of iron in micas. In Mottana, A., and
Sassi, F., Advances in Micas, Mineralogical Society of America and The Geochemical
Society, Reviews in Mineralogy and Geochemistry, 46, 313-349.

Dyar, M. D., Agresti, D.G., Schaefer, M.W., Grant, C.A., and Sklute, E.C. (2006) Mössbauer
spectroscopy of Earth and Planetary Materials. Annual Reviews of Earth and Planetary
Science, 34, 83-125.

Dyar, M.D., Schaefer, M.W., Sklute, E.C., and Bishop, J.L. (2008) Mössbauer spectroscopy of
phyllosilicates: Effects of fitting models on recoil-free fractions and redox ratios. Clay
Minerals., 43, 3-33.

Ehlmann, B.L., Mustard, J.F., Swayze, G.A., Clark, R.N., Bishop, J.L., Poulet, F., Des Marais, D.J., Roach, L.H., Milliken, R.E., Wray, J.J., Barnouin-Jha, O., and Murchie, S.L. (2009) Identification of hydrated silicate minerals on Mars using MRO-CRISM: Geologic context near Nili Fossae and implications for aqueous alteration. Journal of Geophysical Research, v. 114, E00D08, doi:10.1029/2009JE003339, 33 p.

Farmer, V.C., Russell, J.D., McHardy, W.J., Newman, A.C.D., Ahlrichs, J.L., Rimsaite, J.Y.H. (1971) Evidence for loss of protons and octahedral iron from oxidized biotites and vermiculites. Mineralogical Magazine, 38, 121-137.

Farmer, V.C. (1974) The layer silicates. In V.C. Farmer, Ed., The Infrared Spectra of Minerals. Monograph 4, p. 331-363. London, Mineral Society.

Fechtelkord, M., Behrens, H., Holtz, F., Bretherton, J.L., Fyfe, C.A., Groat, L.A., and Raudsepp, M. (2003) Influence of F content on the composition of Al-rich synthetic phlogopite: Part II. Probing the structural arrangement of aluminum in tetrahedral and octahedral layers by ^{27}Al MQMAS and ^{1}H/^{19}F- ^{27}Al TETCOR and REDOR experiments. American Mineralogist, 88, 1046-1054.

Frank, D. and Edmond, L. (2001) Feasibility for identifying mineralogical and geochemical tracers for vermiculite deposits. EPA 910-R-01-002, 44 p. U.S. Environmental Protection Agency, Region 10, Seattle, Washington.

Gates, W.P. (2005) Infrared spectroscopy and the chemistry of dioctahedral smectites. In Kloprogge, T., Vibrational Spectroscopy of Layer Silicates and Hydroxides, Clay Mineral Society Workshop Lectures, 13, 125-168.

Gunter, M.E., Dyar, M.D., Twamley, B., Foit, F.F., Jr., and Cornelius, S.B. (2004) Errata and
Clarification: Composition, $Fe^{3+}/\Sigma Fe$, and crystal structure of non-asbestiform and
asbestiform amphiboles from Libby, Montana, U.S.A. American Mineralogist, 89, 1579.

Gunter, M.E., Singleton, E., Bandli, B.R., Lowers, H.A., and Meeker, G.P. (2005)
Differentiation of commercial vermiculite based on statistical analysis of bulk chemical
data: Fingerprinting vermiculite from Libby, Montana U.S.A. American Mineralogist,
90, 749-754.

Hillier, S. Marwa, E.M.M., and Rice, C.M. (2013) On the mechanism of exfoliation of
vermiculite. Clay Minerals, 48, 563-582.

Hindman, J.R. (2006) Vermiculite. In J.E. Kogel, N.C. Trivedi, J.M. Barker, and S.T.
Krukowski (Eds.), Industrial Minerals & Rocks: Commodities, markets, and uses (7th
edition) p. 1015-1026. Society for Mining, Metallurgy and Exploration, Inc., Littleton,
Colorado.

Jenkins, D.M. (1989) Empirical study of the infrared lattice vibrations (1100—350 cm^{-1}) of
phlogopite. Physics and Chemistry of Minerals, 16, 408-414.

Kabekkodu, S., Ed. (2010) Powder Diffraction File, PDF-4+ 2010. Available:
http://www.icdd.com JCPDS-International Centre for Diffraction Data, Newtown
Square, PA.

Kawano, M., and Tomita, K. (1991) Dehydration and rehydration of saponite and vermiculite.
Clays and Clay Minerals, 39, 174-183.

Kentucky Division for Air Quality (2016) Asbestos in the attic? Access: 2017-07-09. URL:
http://air.ky.gov/SiteCollectionDocuments/Asbestos_in_the_Attic.pdf

Kokaly, R.F. (2011) PRISM: Processing routines in IDL for spectroscopic measurements (installation manual and user's guide, version 1.0). Online. U.S. Geological Survey Open-File Report 2011-1155, 431p.

Langner, R., Fechtelkord, M., Garíca, A., Palin, E.J., López-Solano, J. (2012) Aluminum ordering and clustering in Al-rich synthetic phlogopite: $\{^1H\} \rightarrow {}^{29}Si$ CPMAS HETCOR spectroscopy and atomistic calculations. American Mineralogist, 97 (2-3), 341-352.

Larson, T.C., Antao, V.C., and Bove, F.J. (2010) Vermiculite worker mortality: Estimated effects of occupational exposure to Libby amphibole. Journal of Occupational Environmental Medicine, 52, 555-560.

Libby, S.C. (1975) The origin of potassic ultramafic rocks in the Enoree "Vermiculite" District, South Carolina: University Park, Pennsylvania, Pennsylvania State University, unpublished M.S. thesis, 116 p.

Lowers, H.A., and Meeker, G.P. (2004) Electron probe microanalysis as a tool for identifying vermiculite sources. Proceedings of Microscopy and Microanalysis, Vol. 10, Supplement 2, Microscopy Society of America, p. 904-905. Cambridge University Press.

Madejová, J. (2003) FTIR techniques in clay mineral studies. Vibrational Spectroscopy, 31, 1-10.

Madejová, J., Bujdák, J., Petit, S., and Komadel, P. (2000) Effects of chemical composition and temperature of heating on the infrared spectra of Li-saturated dioctahedral smectites. (II) Near-infrared region. Clay Minerals, 35, 753-761.

68

McDonald, J.C., Harris, J., and Armstrong, B. (2004) Mortality in a cohort of vermiculite miners exposed to fibrous amphibole in Libby, Montana. Occupational Environmental Medicine, 61, 363-366.

MDI (2009) JADE software. Available: http://www.materialsdata.com Materials Data Inc., Livermore, California.

Meeker, G.P., Bern, A.M., Brownfield, I.K., Lowers, H.A., Sutley, S.J., Hoefen, T.M., and Vance, J.S. (2003) The composition and morphology of amphiboles from the Rainy Creek Complex, near Libby, Montana. American Mineralogist, 88, 1955-1969.

___ (2011) NIOSH: Asbestos fibers and other elongate mineral particles: State of the science and roadmap for research, revised edition. National Institutes of Occupational Safety and Health. Current Intelligence Bulletin, 62, 154 p.

Millette, J.R. and Compton, S. (2015) Analysis of vermiculite for asbestos and screening for vermiculite from Libby, Montana. The Microscope, 63(2), 59-75.

Moatamed, F., Lockey, J.E., and Parry, W.T. (1986) Fiber contamination of vermiculites: A potential occupational and environmental health hazard. Environmental Research, 41(1), 207-218.

Muiambo, H.F. (2011) Inorganic modification of Palabora vermiculite, M.S. Thesis, University of Pretoria, South Africa, 103 p.

Mustard, J.F., Murchie, S.L., Pelkey, S.M., Ehlmann, B.L., Milliken, R.E., Grant, J.A., Bibring, J.-P., Poulet, F., Bishop, J., Noe Dobrea, E., Roach, L., Seelos, F., Arvidson, R.E., Wiseman, S., Green, R., Hash, C., Humm, D., Malaret, E., McGovern, J.A., Seelos, K., Clancy, T., Clark, R., Des Marais, D., Izenberg, N., Knudson, A., Langevin, Y., Martin,

69

T., McGuire, P., Morris, R., Robinson, M., Roush, T., Smith, M., Swayze, G., Taylor, H., Titus, T., and Wolff, M. (2008) Hydrated silicate minerals on Mars observed by the CRISM instrument on MRO. Nature, v. 454, p. 305-309.

___ (2010) NIST Standard Reference Database Number 84, FIZ/NIST Inorganic Crystal Structure Database (ICSD). Available: http://www.nist.gov/srd/nist84.cfm National Institute of Standards and Technology, Gaithersburg, Maryland. Produced cooperatively with Fachinformationszentrum Karlsruhe, Germany.

Palabora Mining Company Limited, Mine Geological and Mineralogical Staff (1976) The geology and the economic deposits of copper, iron, and vermiculite in the Palabora Igneous Complex: A brief review. Economic Geology, 7, 177-192.

Papin, A., Sergent, J., and Robert, J.-L. (1997) Intersite OH-F distribution in an Al-rich synthetic phlogopite. European Journal of Mineralogy, 9, 501-508.

Pardee, J.T. and Larsen, E.S. (1928) Deposits of vermiculite and other minerals in the Rainy Creek District, near Libby, Mont. In Contributions to Economic Geology, p. 17-29. U.S. Geological Survey Bulletin 805-B.

Parry, S.A., Pawley, A.R., Jones, R.L., Clark, S.M. (2015) An infrared spectroscopic study of the OH stretching frequencies of talc and 10-Å phase to 10 GPa. American Mineralogist, 92(4), 525-531.

Peipins, L.A., Lewin, M., Compolucci, S., Lybarger, J.A., Miller, A., Middleton, D., Weis, C., Spence, M., Black, B., and Kapil, V. (2003) Radiographic abnormalities and exposure to asbestos-contaminated vermiculite in the community of Libby, Montana, USA. Environmental Health Perspectives, 111, 1753-1759.

70

Post, J.L. (1984) Saponite from near Ballarat, California. Clay and Clay Minerals, 32(2), 147-
153.

Redhammer, G.J., Beran, A., Schneider, J., Amthauer, G., and Lottermoser, W. (2000)
Spectroscopic and structural properties of synthetic micas on the annite-siderophyllite
binary: Synthesis, crystal structure refinement, Mössbauer, and infrared spectroscopy.
American Mineralogist, 85, 449-465.

Rieder, M., Cavazzini, G., D'yakonov, Yu. S., Frank-Kamenetskii, V.A., Gottardi, G.,
Guggenheim, S., Koval', P.V., Müller, G., Neiva, A.M.R., Radoslovich, E.W., Robert, J.-
L., Sassi, F.P., Takeda, H., Weiss, Z., and Wones, D.R. (1999) Nomenclature of the
micas. Mineralogical Magazine, 62, 267-279.

Robbins, D.W., and Strens, R.G.J. (1972) Charge-transfer in ferromagnesian silicates: The
polarized electronic spectra of trioctahedral micas. Mineralogical Magazine, 38, 551-
563.

Robert, J.L., and Kodama, H. (1988) Generalization of the correlations between hydroxyl-
stretching wavenumbers and composition of micas in the system K_2O-MgO-Al_2O_3-SiO_2-
H_2O: A single model for trioctahedral and dioctahedral micas. American Journal of
Science, 288-A, 196-212.

Rohl, A.N., and Langer, A.M. (1977) Mineral analysis of core samples from the Green Springs
area, Virginia vermiculite deposit. Unpublished letter report from Mt. Sinai School of
Medicine, 10 p. Accessed: 2016-04-01.
URL:https://hero.epa.gov/hero/index.cfm/reference/details/reference_id/783502

71

Russell, J.D., and Farmer, V.C. (1970) Replacement of OH by OD in layer silicates, and
identification of the vibrations of these groups in infra-red spectra. Mineralogical
Magazine, 37(292), 869-879.

Sanchez, M. and Gunter, M.E. (2006) Quantification of amphibole content in expanded
vermiculite products from Libby, Montana U.S.A. using powder X-ray diffraction.
American Mineralogist, 91, 1448-1451.

Sanz, J., Gonzalez-Carreno, T., and Gancedo, R. (1983) On dehydroxylation mechanisms of a
biotite in vacuo and in oxygen. Physics and Chemistry of Minerals, 9, 14-18.

Serratosa, J.M. and Bradley, W.F. (1958) Determination of the orientation of OH bond axes in
layer silicates by infrared absorption. Journal of Physical Chemistry, 62, 1164-1167.

Serratosa, J.M., Johns, W.D., and Shimoyama, A. (1970) I.R. study of alkyl-ammonium
vermiculite complexes. Clays and Clay Minerals, 18, 107-113.

Swayze, G.A., Lowers, H.A., Benzel, W.M., Clark, R.N., Driscoll, R.L., Perlman, Z.S., Hoefen,
T.M., and Dyar, M.D. (2018) Spectroscopy of expanded vermiculite products and
insulation. U.S. Geological Survey data release https://doi.org/10.5066/F7JM27SR.

Tischendorf, G., Förester, H.-J., Bottesmann, B., and Rieder, M. (2007) True and brittle micas:
Composition and solid-solution series. Mineralogical Magazine, 71, 285-320.

Van Gosen, B.S. (2002) Reconnaissance study of the geology of U.S. Vermiculite Deposits –
Are asbestos minerals common constituents? U.S. Geological Survey Bulletin 2192, 8p.

Vedder, W. (1964) Correlations between infrared spectrum and chemical compositions of mica.
American Mineralogist, 49, 736-768.

Vedder, W. and Wilkins, R.W.T. (1969) Dehydroxylation and rehydroxylation, oxidation and

reduction of micas. American Mineralogist, 54, 482-509.

Virginia Department of Mines, Minerals, and Energy (2012) Vermiculite. Accessed: 2016-04-

16. URL: https://www.dmme.virginia.gov/dgmr/vermiculite.shtml

Weiss, E.J. and Rowland, R.A. (1956) Effect of heat on vermiculite and mixed layered

vermiculite-chlorite. American Mineralogist, 41, 899-914.

Wright, K.E., and Palmer, C.D. (2008) Geochemical signatures as a tool for vermiculite

provenance determination. INL/EXT-08-14828, 157 p. Idaho National Laboratory.

Wunder, B. and Melzer, S. (2002) Interlayer vacancy characterization of synthetic phlogopitic

micas by IR spectroscopy. European Journal of Mineralogy, 14, 1129-1138.

FIGURES

Figure 1. Photographs of commercial, expanded vermiculite ore from the four major historical

sources: Libby, Montana; Palabora, South Africa; Louisa, Virginia; and Enoree, South

Carolina. Scale of the rightmost image in each set is the same as the left image unless

otherwise labeled. Note (k) shows Libby vermiculite insulation with admixed cellulose

whereas (l) shows Libby vermiculite insulation with admixed fiberglass as they occur in

the attics where they were collected.

Figure 2. Bluish-gray elongate amphibole bundles found in samples of commercial expanded

vermiculite ore from Libby. Amphibole bundles were handpicked from sink fractions

that were separated from expanded ore samples using a modified Cincinnati Method (see

text for details). Image (e) is an enlargement of the bottom portion of the rightmost

amphibole bundle shown in (b).

Figure 3. Secondary electron images of elongate amphibole bundles from the sink fractions of commercial expanded vermiculite ore. (a) to (f) from Libby, Montana, (g) from Enoree, South Carolina, and (h) from an expanded vermiculite ore of unknown origin. Note splayed crystal terminations in (e).

Figure 4. Vermiculite ore provenance diagrams for the four major historical sources: (a) Libby, Montana, (b) Palabora, South Africa, (c) Louisa, Virginia, and (d) Enoree, South Carolina based on compositions from electron probe microanalysis (EPMA). Provenance fields (colored polygons) for individual sources were modified from Lowers and Meeker (2004) by redrawing them around spot analyses from 11 expanded vermiculite ore samples (red symbols) with source documentation (see sample numbers marked with an "h" superscript in Table 1) in addition to their original spot analyses from 36 unexpanded vermiculite ore samples (spot analyses not shown). These fields allow the provenance of the 33 commercial expanded vermiculites (black circles) without source documentation to be determined. In EPMA analyses, all Fe is calculated as Fe^{2+}. All values are total cations of Al, Ti, Mg, and Fe detected per 22 oxygen equivalents. Compositions of the unexpanded and expanded vermiculite ore samples are given in the "Table of Electron Probe Microanalysis of Vermiculite Samples" in Swayze et al. (2018).

Figure 5. Box and whisker diagrams of electron probe microanalysis cation compositions (listed in Table 2) of 4 selected unexpanded vermiculite ore samples (boxes with down-to-left diagonal lines), 28 unexpanded vermiculite ore samples (boxes with cross-hatched lines) and 43 expanded vermiculite ore samples (boxes with down-to-right diagonal lines) from the four major historical sources (excludes the Jiangsu, Mixtures, and "Unknown"

samples). Fe content is calculated as Fe^{2+}. s = number of ore samples used in each box

plot from a given source; n = number of microprobe spot analyses used for each box plot

calculation for a given source. Box bottoms and tops are the first quartile (25th

percentile) and third quartile (75th percentile) whereas the line inside is the median (50th

percentile). Whiskers are the 10th and 90th percentiles. Small circles are outliers. In

order to show details, some outliers ($>90^{th}$ percentile) extend beyond the range of the

plot's y-axis. Mg = total Mg; Al^{oct} = octahedral Al; Fe^{oct} = octahedral Fe; Al^{tet} =

tetrahedral Al.

Figure 6. Measured values of isomer shifts and quadrupole splittings have distinctive ranges

(boxes from Dyar et al., 2006) for each valence state and site occupancy of Fe in the

selected vermiculite ore samples from Enoree, Libby, Louisa, and Palabora (Table 3).

The symbols refer to Fe^{2+} (M1), Fe^{2+} (M2), Fe^{3+} octahedral (O_h), and Fe^{3+} tetrahedral (T_d)

sites in the micas composing the ore samples. The Palabora ALB5SA00 sample contains

tetrahedral Fe^{3+} (shown by the star symbol).

Figure 7. Quantitative X-ray diffraction analyses of selected unexpanded vermiculite ore

samples. Relative intensity ratios were employed to calculate the relative weight percent

of ore components (numbers in left set of pie charts) from random mount scans

(diffractograms under pie charts). Weight percent proportions of phlogopite and

vermiculite in hydrobiotite (numbers in right set of pie charts) were estimated using scans

of oriented mounts (see sample descriptions in Swayze et al., 2018). Note the

hydrobiotite {002} reflection located between the vermiculite and phlogopite {001}

reflections. The hydrobiotite estimate for the Libby GDS469 sample is considered a

minimum value (see text for details).

Figure 8. Comparison of vermiculite insulation's spectral features with those of elongate

amphibole from Libby, talc (from Clark et al., 2007), and serpentine (chrysotile).

Vermiculite ore's 1.40-μm OH overtone and 2.32-μm cation-OH stretch-plus-bend

combination absorptions overlap with similar absorptions in amphibole, talc, and

serpentine making it difficult to detect trace levels of these impurities. Inset shows that

amphibole, talc, and serpentine spectra lack a 1.42-μm absorption like that present in

spectra of expanded vermiculite ore (see dashed vertical lines; spectra offset vertically for

clarity). Reflectance spectra collected with an ASD Inc. FieldSpec$^{®}$ spectrometer.

Spectral identification numbers (i.e., spd0075 r90067) uniquely identify spectra.

Figure 9. Reflectance spectra of representative expanded vermiculite ore samples from each of

the four major historical sources. The shapes of the 1.40- and 2.32-μm composite

absorptions vary depending on sample mineralogy and composition. Arrows mark the

long wavelength edge of the intense Fe-electronic absorption envelope; vertical lines

mark the 2.24- and 2.38-μm composite absorptions.

Figure 10. (a) and (b) show continuum-removed OH stretch overtone and combination

absorptions from spectra of handpicked, ground flakes of phlogopite, hydrobiotite, and

vermiculite from unexpanded Libby vermiculite ore. Identification of these phases is

based on XRD analyses. Spectra offset vertically for clarity in (a) and (b). (c) and (d)

show continuum-removed OH stretch overtone and combination absorptions from spectra

of unexpanded, handpicked, ground Libby vermiculite flakes before and after interlayer

K^+ exchange. Vertical lines in (a) and (c) mark the wavelength positions of the 1.38-,

1.40-, and 1.42-μm OH stretch overtone absorptions. Vertical lines in (b) and (d) mark

the wavelength positions of the 2.30-, 2.32-, and 2.38-μm cation-OH bend-plus-stretch

combination absorptions.

Figure 11. Continuum-removed absorbance spectra of handpicked, ground flakes of phlogopite,

hydrobiotite, and vermiculite from unexpanded Libby ore, and of a K^+-exchanged split of

the vermiculite, showing the OH stretch fundamental absorptions and their deconvolution

into symmetrical Gaussians. Phase identification and purity of the separates were

verified by XRD. Vibrational assignments of individual Gaussian absorptions are given

in Table 5. The coefficient of determination (r^2) gives the goodness of fit between the

observed spectrum (dotted line) and deconvolution model (wide gray line under dotted

line). Note asymmetry of N-band composite absorption in the vermiculite spectrum. See

text for discussion of N-, I-, and V-band ranges labeled beneath spectra.

Figure 12. Continuum-removed absorbance spectra of handpicked, ground phlogopite,

hydrobiotite, and vermiculite flakes from unexpanded Libby ore showing the out-of-

plane and in-plane cation-OH bend fundamental absorptions and their deconvolution into

symmetrical Gaussians. Vibrational assignments of individual Gaussian absorptions are

given in Table 5. The coefficient of determination (r^2) gives the goodness of fit between

the observed spectrum (dotted line) and deconvolution model (wide gray line under

dotted line). The N-, I-, and V-band ranges labeled beneath spectra are for the out-of-

plane bend vibrations; see text for details.

Figure 13. Continuum-removed absorbance spectra of handpicked, ground phlogopite,

hydrobiotite, and vermiculite flakes from unexpanded Libby ore showing the OH-stretch-

overtone absorptions and their deconvolution into symmetrical Gaussians. Vibrational

assignments of individual Gaussian absorptions are given in Table 6. The coefficient of

determination (r^2) gives the goodness of fit between the observed spectrum (dotted line)

and deconvolution model (wide gray line under dotted line). See text for discussion of N-

, I-, and V-band ranges labeled beneath spectra.

Figure 14. Continuum-removed absorbance spectra of handpicked, ground phlogopite,

hydrobiotite, and vermiculite flakes from unexpanded Libby ore showing the out-of-

plane and in-plane cation-OH bend-plus-stretch combination absorptions and their

deconvolution into symmetrical Gaussians. Vibrational assignments of individual

Gaussian absorptions are given in Table 6. The coefficient of determination (r^2) gives the

goodness of fit between the observed spectrum (dotted line) and deconvolution model

(wide gray line under dotted line). The N-, I-, and V-band ranges labeled beneath spectra

are for the out-of-plane vibrations; see text for details.

Figure 15. (a) Continuum-removed absorbance spectra of selected unexpanded vermiculite ores

from Enoree, Libby, Louisa, and Palabora showing the OH stretch fundamental

absorptions and their deconvolution into symmetrical Gaussians. (b) Continuum-

removed absorbance spectra of representative expanded vermiculite ores from the same

sources. Vibrational assignments for the absorptions are given in Table 5.

Deconvolution suggests the presence of a sharp absorption from trace talc in the spectrum

of GDS847. The presence of this impurity is also supported by XRD and SEM analyses

(see the GDS847 sample description in Swayze et al., 2018). The relatively large grain

size of talc in the ALB22SC00 sample allowed removal by hand prior to KBr pellet

fabrication. The coefficient of determination (r^2) gives the goodness of fit between the

observed spectrum (dotted line) and deconvolution model (wide gray line under dotted

line). Note asymmetry of N-, I-, and V-band composite absorptions in the Zonolite[®] 4

spectrum.

Figure 16. Average 1.40/1.42 – 1.38/2.32-μm band-depth-ratio values of commercial expanded

vermiculite ore samples used to determine their mine sources. The phlogopite and

phlogopitic component of hydrobiotite in expanded vermiculite ores is indicated by the

1.38/2.32-μm band depth ratio. Spectral abundance of impurities (i.e., amphibole, talc,

and/or serpentine) is indicated by 1.40/1.42-μm band depth ratio. Mine sources can also

be identified by the 1.38/2.32-μm band depth ratio. Source areas determined

independently by electron probe microanalysis and, when available, sample

documentation for expanded ore samples from the four major historical sources (see

Table 1 and the individual sample descriptions in Swayze et al., 2018). Louisa samples

fall on the zero-tick mark of the 1.38/2.32-μm band-depth-ratio axis, so its provenance

field was extended left of zero for display purposes. Symbol shape is keyed to

vermiculite ore deposit and color to individual samples. Sample key is also applicable to

Figures 18 and 21. Black curve is the impurity non-detect threshold (see text for details).

See text for origin of constructed amphibole (amp.) + vermiculite (vermic.) ore mixtures

and significance of the false positive identification (i.e., gray hexagon).

Figure 17. Comparison of the continuum-removed OH-stretch-overtone region of handpicked, ground flakes of hydrobiotite from the unexpanded Libby ore in transmission and reflectance. Vertical line marks wavelength position of the 1.38-μm $Mg_3OH_{repulsed}$ composite overtone absorption. Overall, the strength of this absorption is weaker in transmission than in reflectance due to the low concentration of sample (0.23 wt%) dispersed in the KBr transmission pellet compared to the optically thick sample used for the reflectance measurement. Nonetheless, the 1.38-μm composite absorption appears weaker in reflectance relative to the 1.40-μm composite absorption, despite their similar strengths in transmission. This is due to the spectrally dominating effect, in reflectance, of intense overlapping Fe-electronic absorptions centered at shorter wavelengths (not shown).

Figure 18. Mine sources of expanded vermiculite ore samples based on their average 2.24/2.38 – 1.38/2.32-μm band-depth-ratio values. "Mixtures" and Palabora sample values plot on the zero-tick mark of the 2.24/2.38-μm band-depth-ratio axis, so those provenance fields were extended above and below zero for display purposes. The Louisa sample values fall on the zero-tick mark of the 1.38/2.32-μm band-depth-ratio axis, so this provenance field was extended left of zero for display purposes. See Figure 16 for sample key. The relative amount of phlogopitic component is indicated by the 1.38/2.32-μm band depth ratio; the 2.24/2.38-μm band depth ratio indicates the relative spectral abundance of octahedral $MgFe^{3+}[\ ]OH$ and $MgAl[\ ]OH$ cation clusters.

Figure 19. Continuum-removed absorbance spectra of the unexpanded Zonolite® 4 and expanded ALB22SC00 ore samples from Enoree, South Carolina, in the (a) OH stretch and (b)

cation-OH bend fundamental regions showing absorptions and their deconvolution into

symmetrical Gaussians. Vibrational assignments for the ν_3, ν_h, ν_i, ν_j, ν_k, and δ_3

absorptions are given in Table 5. Vertical arrows in (a) and (b) indicate that the ν_3 stretch

and δ_3 bend absorptions are present in spectra of the expanded ore but not in the spectra

of the unexpanded ore. The ν_i absorption, present in the spectrum of the unexpanded ore,

was not resolved from the ν_h and ν_j absorptions in the deconvolution model in the

expanded ore spectrum. The KBr pellet was made from a different split of the same

expanded ore sample used to measure the spectra shown in Figures 15b and A5, but it has

a slightly different relative content of phlogopite, hydrobiotite, and vermiculite. The

coefficient of determination (r^2) gives the goodness of fit between the observed spectrum

(dotted line) and deconvolution model (wide gray line under dotted line).

Figure 20. (a) Continuum-removed absorbance spectra of the NIR combination region for

unexpanded and expanded vermiculite ore samples from Enoree, South Carolina (same

samples as used in Fig. 19), with their deconvolution into symmetrical Gaussians.

Montmorillonite and talc are trace impurities in the unexpanded ore. The diagnostic

spectral signature of montmorillonite at 2.21 μm is absent from the spectrum of the

heated, expanded ore. Vibrational assignments for c_i, c_k, and c_3 are given in Table 6.

Modeling did not resolve c_i and c_k into separate absorptions by modeling. The coefficient

of determination (r^2) gives the goodness of fit between the observed spectrum (dotted

line) and deconvolution model (wide gray line under dotted line). (b) Continuum-

removed reflectance spectra of the same samples in the same spectral region. Both

sample containers were labeled Zonolite® 4 from Enoree, South Carolina, including that

containing the ALB22SC00 sample. Note that the 2.24-μm absorption intensifies while

the 2.38-μm absorption weakens in response to heat-induced expansion.

Figure 21. Mine sources of expanded vermiculite ore samples based on the average 2.24/2.38-

μm band-depth-ratio values and 2.24-μm composite absorption wavelength positions in

microns. Sample values that plot just outside of the Libby provenance field (i.e., the light

green box) are most likely from ores or mixtures of ores from sources other than Libby

(i.e., the gray hexagon symbol is from a mixture of Palabora and Enoree ores that mimics

the spectral signature of Libby ore as shown in Figs. 16 and 18). See Figure 16 for

sample key. The Palabora provenance field was extended left and right of zero along the

2.24/2.38-μm band-depth-ratio axis for display purposes.

Figure A1. Atomic structure model of a vermiculite from Santa Olalla, Teoledo Province, Spain,

based on X-ray diffraction information from Arguelles et al. (2010), created using

CrystalMaker® v. 10.0.4. It consists of octahedral layers (O) sandwiched between

tetrahedral layers (T) forming repeating T-O-T stacks that surround water-rich interlayers

forming a 2:1 clay.

Figure A2. The 295 K Mössbauer spectra of selected unexpanded vermiculite ore samples from

the four major historical sources. See text for a discussion of the deconvolution modeling

process.

Figure A3. Locations of the four major historical vermiculite ore sources (in bold) for the U.S.

market including Libby, Montana; Louisa, Virginia; Enoree district, South Carolina; and

Palabora, South Africa. An expanded vermiculite ore sample from Jiangsu, China was

also part of this study. Modified from Frank and Edmond (2001).

Figure A4. Spectral absorption continuum removal procedure. Note continuum endpoints were

manually selected in this study, but their selection could be automated using first

derivatives to locate shoulder high points in high signal-to-noise ratio reflectance data.

See appendix for details of this procedure.

Figure A5. Continuum-removed absorbance spectrum of the expanded ALB22SC00 ore sample

from Enoree, before and after K^+ exchange, in the OH stretch fundamental region

showing absorptions and their deconvolution into symmetrical Gaussians. Note that the

ν_3 MgAl[ ]OH absorption retains its strength relative to the ν_g non-repulsed I-band

absorption after K^+ exchange. Vibrational assignments for the absorptions are given in

Table 5. The coefficient of determination (r^2) gives the goodness of fit between the

observed spectrum (dotted line) and deconvolution model (wide gray line under dotted

line).

Figure A6. Continuum-removed absorbance spectra of an unexpanded Mg-vermiculite VTx-1

sample from Llano, Texas, in the (a) OH stretch and (b) cation-OH bend fundamental

regions showing absorptions and their deconvolution into symmetrical Gaussians.

Vibrational assignments for the absorptions are given in Table 5. The need to tie a

continuum endpoint to the low-frequency side of the broad 600 to 850 cm^{-1} composite

absorption in the presence of strong overlapping H_2O-related absorptions, distorts the

relative strength of δ_d, which is actually greater than that of δ_e, whereas the relative

strength of δ_a (not shown) is actually about equal to that of δ_b. The coefficient of

determination (r^2) gives the goodness of fit between the observed spectrum (dotted line)

and deconvolution model (wide gray line under dotted line).

Figure A7. (a) NIR reflectance spectra of the unexpanded Mg-vermiculite VTx-1 sample from

Llano, Texas, before and after K^+ exchange. Note the 2.24-μm c_3 composite combination

absorption persists even after K^+ replaces interlayer water. (b) Polarized transmission

spectra of VTx-1 showing that the intensity of the 2.24-μm absorption is stronger when

light is parallel to the basal cleavage (inclination = 0°), whereas the 1.39-μm composite

absorption (marked by leftmost vertical lines) is weaker. See appendix for a discussion

of the significance of these observations. Rightmost vertical lines mark position of the

2.24-μm absorption. Reflectance spectra offset vertically for clarity.

Figure A8. Continuum-removed (a) OH stretch overtone and (b) combination absorptions of the

Mg-vermiculite VTx-1 sample from Llano, Texas, before and after partial deuteration. In

the middle spectra, H_2O absorptions are replaced by D_2O absorptions at longer

wavelengths (not shown), which reduces overlap with the 1.4-μm region OH overtone

and 2.3-μm region combination absorptions. Weaker H_2O absorptions, as a result of

deuteration, allow photons to penetrate further into the sample, so the OH absorptions

become stronger relative to those in spectra of the pre-deuteration sample, after

continuum removal. Vertical lines mark the wavelength position of the 2.24-μm

absorption.

Figure A9. The distribution of individual 1.40/1.42-μm band-depth-ratio values of expanded

Libby vermiculite ore is positively skewed by the presence of coarse-grained elongate

amphibole bundle impurities relative to the negative skew of band-depth-ratio values of

an expanded Palabora – Enoree ore mixture that was amended with fine-grained elongate

amphibole particles. Black curve is the impurity non-detect threshold (see text for a more details).

Figure A10. Evaluation of the total surface area of an expanded vermiculite ore sample that must be spectrally measured to derive a precise average 1.38/2.32-µm band-depth-ratio value for source determination. Individual measurements of 1.38/2.32-µm band-depth-ratio values for expanded Libby ore samples with different average flake size distributions: (a) 4 to 5 mm and (b) 1 to 2 mm. Note that some individual band-depth-ratio values fall outside the Libby provenance field. (c) and (d) cumulative averages of 1.38/2.32-µm band-depth-ratio values for the same samples. Variability in the cumulative average band-depth-ratio values stabilize after measuring 43 cm^2 of the coarser-grained sample's surface area whereas only 20 cm^2 must be measured to reach stable values for the finer-grained sample.

Figure A11. Evaluation of the total surface area of an expanded vermiculite ore sample that must be spectrally measured to derive a precise average band-depth-ratio value for detecting amphibole, talc, and/or serpentine impurities. (a) and (b) individual measurements of 1.40/1.42-µm band-depth-ratio values for coarser- and finer-grained expanded Libby ore samples. (c) and (d) cumulative averages of 1.40/1.42-µm band-depth-ratio values for the same samples. Band-depth-ratio values stabilize after measuring 28 cm^2 of the coarser-grained sample's surface area whereas only 20 cm^2 must be measured to reach stable values for the finer-grained sample.

Figure A12. Evaluation of the total surface area of an expanded vermiculite ore sample that must be spectrally measured to derive a precise average 2.24/2.38-µm band-depth-ratio

value for source determination. (a) and (b) individual measurements of 2.24/2.38-μm

band-depth-ratio values for coarser- and finer-grained expanded Libby ore samples. Note

that some individual data values fall outside the Libby provenance field. (c) and (d)

cumulative averages of 2.24/2.38-μm band-depth-ratio values for the same samples.

Band-depth-ratio values stabilize after measuring 100 cm^2 of the coarser-grained

sample's surface area whereas only 60 cm^2 need be measured to reach stable values for

the finer-grained sample.

Figure A13. Same as Figure 16 with band-depth-ratio values of a few expanded vermiculite ore

samples derived from spectra measured at finer spectral resolution (6 nm) then convolved

to the sampling and bandpasses of the normal resolution (11 nm). FR= band-depth-ratio

values from the convolved finer resolution spectra; NR = band-depth-ratio values from

the spectra measured at normal resolution. Note that FR points plot within their correct

provenance fields. An ASD FieldSpec 4 Hi-Res NG$^®$ spectrometer was used to measure

the reflectance of the samples at 6 nm resolution.

Figure A14. Same as Figure 18 with band-depth-ratio values of a few expanded vermiculite ore

samples derived from spectra measured at finer spectral resolution (6 nm) then convolved

to the sampling and bandpasses of the normal resolution (11 nm). FR= band-depth-ratio

values from the convolved finer resolution spectra; NR = band-depth-ratio values from

the spectra measured at normal resolution. Note that FR points plot within their correct

provenance fields. An ASD FieldSpec 4 Hi-Res NG$^®$ spectrometer was used to measure

the reflectance of samples at 6 nm resolution.

Figure A15. Same as Figure 21 with 2.24/2.38-μm band depth ratio and 2.24-μm absorption

wavelength position values of a few expanded vermiculite ore samples derived from

spectra measured at finer spectral resolution (6 nm) then convolved to the sampling and

bandpasses of the normal resolution (11 nm). FR= band-depth-ratio values from the

convolved finer resolution spectra; NR = band-depth-ratio values from the spectra

measured at normal resolution. Note that FR points plot within their correct provenance

fields. An ASD FieldSpec 4 Hi-Res NG$^{®}$ spectrometer was used to measure the

reflectance of samples at 6 nm resolution.

Figure A16. Continuum-removed reflectance spectra of vermiculite, saponite, and expanded

vermiculite ore showing absorptions in the NIR (a) overtone and (b) combination spectral

regions.   All spectra are convolved to CRISM (Compact Reconnaissance Imaging

Spectrometer for Mars) spectral resolution (Mustard et al. 2008). Vertical lines in (a)

mark the wavelength positions of the 1.38-, 1.40-, 1.42-μm composite overtone

absorptions in the spectrum of the vermiculite ore; vertical lines in (b) mark the 2.30-,

2.32-, and 2.38-μm composite combination absorptions in spectra of the vermiculite and

vermiculite ore. Spectral identification numbers (i.e., spd0449 r740) uniquely identify

spectra. Vermiculite and expanded vermiculite ore samples are from this study. Saponite

SapCa-1 is from the Source Clays Repository with its chemistry listed in Post (1984).

This sample underwent acetate-acetic acid buffer removal of carbonate prior to spectral

measurement.

Table 1. Expanded vermiculite ores examined in this study: their sources and amphibole, talc, and/or serpentine impurities.

Sample information	Sample number	Collection location [a]	Source (provenance) Probe micro-analysis	Source (provenance) UV-NIR spectroscopy	XRD B	XRD S	MCM[b]	SEM/ EDS	Band Depth Ratio	Details of analytical examinations [c]
					Attic insulation					
House	at1UI	Moscow, ID	Libby	Libby	No	Yes[d]	Yes	Yes	Yes	Sodic-calcic elongate amphibole bundles
House bag 1	GDS332	Lansing, MI	Libby	Libby	Yes	Yes[d]	Yes	Yes	Yes	Sodic-calcic elongate amphibole bundles
House	GDS460	Denver, CO	Enoree	Enoree	Yes	---[e]	---[e]	No	Yes	No amphibole, serpentine or talc particles [f]
House bag 2	GDS649	Lansing, MI	Libby	Libby	---[g]	Yes[d]	Yes	Yes	Yes	Sodic-calcic elongate amphibole bundles
Church	GDS701 [h]	Libby, MT	Libby	Libby	Yes	Yes[d]	Yes	Yes	Yes	Sodic-calcic elongate amphibole bundles
House	GDS823	Pueblo, CO	Libby	Libby	---[g]	Yes[d]	Yes	Yes	Yes	Sodic-calcic elongate amphibole bundles
Building	GDS886	Denver, CO	Libby	Libby	---[g]	Yes[d]	Yes	Yes	Yes	Sodic-calcic elongate amphibole bundles
Building	GDS887	Denver, CO	Libby	Libby	---[g]	Yes[d]	Yes	Yes	Yes	Sodic-calcic elongate amphibole bundles
Building	GDS907	Silver Spring, MD	Libby	Libby	---[g]	Yes[d]	Yes	Yes	Yes	Sodic-calcic elongate amphibole bundles
House	GDS909 [h]	Libby, MT	Libby	Libby	---[g]	Yes[d]	Yes	Yes	Yes	Sodic-calcic elongate amphibole bundles
Building	GDS911	Silver Spring, MD	Libby	Libby	---[g]	Yes[d]	Yes	Yes	Yes	Sodic-calcic elongate amphibole bundles
House	GDS915 [h]	Libby, MT	Libby	Libby	---[g]	Yes[d]	Yes	Yes	Yes	Sodic-calcic elongate amphibole bundles
Building	GDS916	New Bedford, MA	Libby	Libby	---[g]	Yes[d]	Yes	Yes	Yes	Sodic-calcic elongate amphibole bundles
House	GDS919 [h]	Libby, MT	Libby	Libby	---[g]	Yes[d]	Yes	Yes	Yes	Sodic-calcic elongate amphibole bundles
House	GDS920 [h]	Libby, MT	Libby	Libby	---[g]	Yes[d]	Yes	Yes	Yes	Sodic-calcic elongate amphibole bundles
House	GDS921 [h]	Libby, MT	Libby	Libby	---[g]	Yes[d]	Yes	Yes	Yes	Sodic-calcic elongate amphibole bundles
Building	GDS922	Denver, CO	Libby	Libby	---[g]	Yes[d]	Yes	Yes	Yes	Sodic-calcic elongate amphibole bundles
Building	GDS923	Denver, CO	Libby	Libby	---[g]	Yes[d]	Yes	Yes	Yes	Sodic-calcic elongate amphibole bundles
Building	GDS924	Denver, CO	Libby	Libby	---[g]	Yes[d]	Yes	Yes	Yes	Sodic-calcic elongate amphibole bundles
Building	GDS925	Denver, CO	Libby	Libby	---[g]	Yes[d]	Yes	Yes	Yes	Sodic-calcic elongate amphibole bundles
Bag insulation	GDS450	Golden, CO [i]	Palabora[j]	Mixture	No	---[e]	---[e]	No	Yes	No amphibole, serpentine or talc particles [f]
Bag A-Tops®	GDS906	Beaver Falls, PA [i]	Palabora	Palabora	---[g]	---[g]	No	No	No	No amphibole, serpentine or talc particles [f]
Bag Strong-Lite®	GDS918	Arlington Heights, IL [i]	Palabora	Palabora	---[g]	---[g]	No	No	No	No amphibole, serpentine or talc particles [f]
Bag Zonolite®	Li2UI [h]	Libby, MT [k]	Libby	Libby	---[g]	Yes[d]	Yes	Yes	Yes	Sodic-calcic elongate amphibole bundles

101

Horticultural products (from bags)

Scotts®	GDS327	Marysvale, OH[k]	Palabora+Enoree	Palabora	No	No	No	Yes	No	Two equant amphibole particles
Black Gold®	GDS453	Hubbard, OR[k]	Palabora	Palabora	No	No	No	No	No	No amphibole, serpentine or talc particles[f]
Hoffman®	GDS455	Lancaster, PA[k]	Louisa or Enoree	Louisa	Yes	Yes	No	Yes	Yes	Talc & possible serpentine, no amphibole[f]
Schultz®	GDS626	St. Louis, MO[k]	Palabora	Palabora	No	Yes	No	No	Yes	No amphibole, serpentine or talc particles[f]
Hyponex®	GDS627	Marysvale, OH[k]	Enoree	Enoree	No	Yes	Yes	Yes	Yes	Elongate tremolite/actinolite particles and talc
ACE Hardware®	GDS628	Oak Brook, IL[k]	Louisa	Louisa	Yes	Yes	No	Yes	No	Prismatic amphibole particles likely tremolite
Sun Gro®	GDS631	Pine Bluff, AR[k]	Palabora+Enoree/Louisa+unknown	Mixture	Yes	---[g]	No	Yes	No	Amphibole particle likely tremolite
DESA Heating®	GDS836	Denver, CO[i]	Unknown source	Mixture	---[g]	---[g]	Yes	Yes	Yes	Elongate amphibole/tremolite particles
Mica Grow®	GDS908	Bloomfield, OH[i]	Louisa	Louisa	---[g]	---[g]	No	Yes	Yes	Elongate tremolite/actinolite particles
Purcells®	GDS910	Springfield, VA[k]	Palabora	Palabora	---[g]	---[g]	No	No	Yes	No amphibole, serpentine or talc particles[f]
Country Cottage®	GDS913	Hopkins, MN[i]	Louisa or Enoree	Louisa	---[g]	---[g]	No	Yes	Yes	Amphibole particle likely hornblende
Miracle Grow®	GDS914	Hopkins, MN[i]	Enoree	Enoree	---[g]	---[g]	No	Yes	Yes	Blocky amphibole particles -- no talc

Packing & miscellaneous products

Al Bush Collection	ALB006CH01	Jiangsu, China	Jiangsu	Jiangsu	No	---[e]	---[e]	Yes	Yes	Trace serpentine and talc; no amphibole
Al Bush Coll. Zonolite® 4	ALB22SC00[h]	Enoree, SC	Enoree	Enoree	No	---[e]	---[e]	Yes	Yes	Trace elongate talc or anthophyllite
Al Bush Coll. Zonolite® 3	ALB23SC00[h]	Enoree, SC	Enoree	Enoree	No	---[e]	---[e]	No	Yes	No amphibole or serpentine
Virginia Vermiculite mine	GDS847[h]	Louisa, VA	Louisa	Louisa	---[g]	Yes	No	Yes	Yes	Blocky to prismatic talc or anthophyllite and prismatic to elongate tremolite/actinolite
W.R. Grace mine	GDS850[h]	Enoree, SC	Enoree	Enoree	---[g]	Yes	No	Yes	Yes	Talc and blocky amphibole likely actinolite
Terra Lite®	GDS445	Denver, CO	Palabora	Palabora	---[g]	---[g]	---[e]	Yes	Yes	Prismatic talc or anthophyllite, serpentine
Chemical packing old	GDS629	Denver, CO	Palabora+Enoree	Libby (false positive)	Yes	Yes	No	Yes	Yes	Sodic-calcic elongate amphibole bundle; talc or anthophyllite
Chemical packing 2004	GDS663	Denver, CO	Palabora	Palabora	---[g]	No	No	Yes	Yes	One small sodic-calcic elongate amphibole particle
Chemical packing 2009	GDS876	Denver, CO	Palabora+unknown	Mixture	---[g]	---[g]	Yes	Yes	Yes	Sodic-calcic elongate amphibole bundles
Zonolite® Chem. packing	GDS652	Port Orchard, WA	Libby	Libby	---[g]	Yes[d]	Yes	Yes	Yes	Sodic-calcic elongate amphibole bundles
Zonolite® Chem. packing	GDS653	Port Orchard, WA	Libby	Libby	---[g]	Yes[d]	Yes	Yes	Yes	Sodic-calcic elongate amphibole bundles
Sun Gro® Chem. packing	GDS700	Denver, CO[i]	Palabora	Palabora	No	No	No	No	Yes	No amphibole, serpentine or talc particles[f]
Zonolite® Chem. packing	GDS917	Kent, WA[i]	Libby	Libby	---[g]	Yes[d]	Yes	Yes	Yes	Sodic-calcic elongate amphibole bundles
Bag Therm-O-Rock®	GDS650	Port Orchard, WA	Palabora+Enoree	Mixture	---[g]	No	No	Yes	No	One small elongate amphibole

102

| Bag Zonolite® IV | GDS651 | Port Orchard, WA | Enoree | Louisa | ---[g] | Yes | No | Yes | Yes | Sodic-calcic prismatic to elongate amphibole and talc |
| Bag masonry Zonolite® | GDS912 | Miami, FL [i] | Enoree | Enoree | ---[g] | ---[g] | Yes | Yes | Yes | Elongate hornblende and tremolite/actinolite |

Notes: XRD = X-ray diffraction analysis of bulk ore samples (B) and sink fractions (S). SEM-EDS = Scanning Electron Microscope – Energy-Dispersive X-Ray Spectroscopy. Band Depth Ratio = 1.40/1.42-μm band depth ratio. The use of "sodic-calcic" refers to amphiboles with compositions including primarily those of winchite, rictherite, and tremolite. The exact amphibole species could not be determined with qualitative SEM-EDS analysis (Meeker et al. 2003; Lowers and Meeker 2004). In this study, we use the term "elongate amphibole particle" (NIOSH 2011) to encompass all amphibole crystals longer than 5 μm with an aspect ratio greater than 3:1 whose habits are asbestiform or nonasbestiform or may have formed as a result of cleaving. Unknown source = distinctly different spectral signature than any of those of the four major historical sources of expanded vermiculite ore. Mixture = combination of ores, one of which is from one of four major historical sources of commercial expanded vermiculite ore. Enoree = Enoree, South Carolina; Libby = Libby, Montana; Louisa = Louisa, Virginia; Palabora = Palabora Mine in South Africa. Chem. = chemical; comp. = composition.

[a] Sample collection location is given; otherwise city of purchase [i] or product manufacture [k] is provided when available.

[b] MCM = Modified Cincinnati Method (see text for description). Yes = detection of macroscopically visible elongate amphibole, talc, or serpentine.

[c] Details of MCM, microprobe, spectroscopy, XRD, and SEM-EDS analyses for expanded vermiculite ore samples can be found in the individual sample descriptions in Swayze et al. (2018).

[d] Macroscopic elongate amphiboles bundles were removed from the sink fraction prior to XRD analysis but were verified as amphibole by SEM analysis, thus they are listed here as being "detectable" by XRD.

[e] Insufficient sample volume to generate a sink fraction for analysis with XRD or MCM.

[f] If hours of searching revealed no amphibole, talc, and/or serpentine particles on an SEM mount then the sample was not considered to contain them.

[g] XRD analysis not performed on the bulk sample and/or its sink fraction sample as noted.

[h] Samples, among others (Lowers and Meeker 2004), used to establish provenance fields on electron probe microanalysis diagrams (Fig. 4).

[i] See [a] above.

[j] Large Palabora flakes spatially dominate probe mounts so analyses may not have sampled smaller flakes from a non-Palabora source in this mixture of ores.

[k] See [a] above.

Table 2. Average EPMA chemical analyses and calculated mineral formulas of selected unexpanded vermiculite ores.

Element	ALB1VA00 Louisa, VA n = 25	Zonolite® 4 Enoree, SC n = 29	GDS469 Libby, MT n = 25	ALB5SA00 Palabora, S. Africa n = 22
SiO_2 (wt%)	38.36	40.21	38.19	41.35
TiO_2	1.80	1.61	1.40	0.92
Al_2O_3	14.50	14.07	13.32	10.19
Fe_2O_3	7.89	9.31	7.52	7.38
FeO	1.46	0.93	2.38	1.08
MnO	0.08	0.11	0.08	0.05
MgO	21.33	18.98	21.40	25.57
CaO	0.38	0.75	1.06	0.13
Na_2O	0.12	0.16	0.15	0.02
K_2O	4.19	5.28	6.29	5.75
H_2O [a]	11.62	8.27	6.19	8.43
Cl	0.02	0.06	0.02	0.01
F	0.33	0.56	0.22	0.57
Subtotal	102.09	100.28	98.22	101.48
O=F,Cl	0.14	0.25	0.10	0.24
Total	101.95	100.03	98.12	101.24
Number of ions on the basis of 22 oxygen equivalents per formula unit				
Si^{4+}	5.616	5.831	5.609	5.932
Al^{3+}	2.384	2.169	2.304	1.723
Fe^{3+} [b]	0.000	0.000	0.087	0.345
T_d sum	8.000	8.000	8.000	8.000
Al^{3+}	0.118	0.233	----	----
Mg^{2+}	4.625	4.103	4.685	5.311
Fe^{2+} [b]	0.178	0.113	0.292	0.130
Fe^{3+} [b]	0.870	1.016	0.744	0.452
Ti^{4+}	0.199	0.176	0.154	0.100
Mn^{2+}	0.010	0.013	0.011	0.007
O_b sum [c]	6.000	5.654	5.886	6.000
Mg^{2+}	0.030	----	----	0.158
Ca^{2+}	0.059	0.117	0.167	0.021
Na^+	0.035	0.044	0.043	0.007
K^+	0.783	0.976	1.179	1.052
Interlayer sum	0.907	1.137	1.389	1.238
Cl	0.005	0.014	0.006	0.003
F	0.154	0.255	0.103	0.258
OH	3.841	3.731	3.891	3.739
Sum	4.000	4.000	4.000	4.000
H_2O [d]	3.756	2.134	1.086	2.166

Notes: Compositions of bulk samples not individual minerals. n = number of microprobe spot analyses collected on multiple mica flakes used to calculate the averaged composition of each

104

sample.   ---- = not enough cation Al and/or Mg to assign to this site. Cation sites were filled according to Deer et al. (1966). Spectral results are consistent with some Mg in the Louisa sample occupying interlayer sites.

[a] Essential water = total water (released from 25 to 950 °C) – absorbed water (released at ≤70 °C).

[b] Proportion of Fe^{3+} and Fe^{2+} calculated from Mössbauer analysis.

[c] Spectral absorptions near 3625 cm^{-1} indicate the presence of octahedral layer vacancies in ALB1VA00 and Zonolite® 4, with trace levels in the other two selected samples, indicating that more Mg resides in the interlayer site than is shown in the table above.

[d] Interlayer water molecules per formula unit = essential water – 4(OH) water equivalent.

Table 3. Mössbauer spectral parameters obtained at 295 K for selected unexpanded vermiculite ore samples.

Site	Parameter	ALB1VA00 Louisa, VA	Zonolite® 4 Enoree, SC	GDS469 Libby, MT	ALB5SA00 Palabora, S. Africa
$Fe^{3+}(T_d.O_h)$	IS (mm/s)	0.31	0.39	0.36	0.26
	QS (mm/s)	0.74	0.45	0.46	0.50
	Width (mm/s)	0.48	0.27	0.37	0.53
	Area (%)	34	7	11	28
$Fe^{3+}(O_{h1})$ [a]	IS (mm/s)	0.42	0.37	0.37	0.41
	QS (mm/s)	1.16	0.75	0.88	0.99
	Width (mm/s)	0.55	0.41	0.48	0.64
	Area (%)	38	36	39	58
$Fe^{3+}(O_{h2})$ [a]	IS (mm/s)	0.28	0.40	0.43	---- [b]
	QS (mm/s)	1.13	1.16	1.18	----
	Width (mm/s)	0.34	0.54	0.46	----
	Area (%)	11	47	25	----
	% Fe^{3+}	83	90	74	86
$Fe^{2+}(M1)$	IS (mm/s)	1.15	1.00	1.10	0.99
	QS (mm/s)	2.08	2.34	2.24	2.29
	Width (mm/s)	0.33	0.26 [c]	0.36	0.26 [c]
	Area (%)	5	2	7	4
$Fe^{2+}(M2)$	IS (mm/s)	1.15	1.05	1.09	1.09
	QS (mm/s)	2.54	2.78	2.68	2.68
	Width (mm/s)	0.32	0.35	0.33	0.26 [c]
	Area (%)	12	7	19	10
	% Fe^{2+}	17	9	26	14
	χ^2_{norm}	1.2	2.0	0.8	0.8

Notes: IS = isomer shift; QS = quadrupole splitting; Width = absorption peak width; Area = % area of an absorption peak relative to other peaks in the spectrum.
[a] O_{h1} & O_{h2} = 1st and 2nd octahedral Fe^{3+} sites.
[b] No second octahedral Fe^{3+} site was resolved in the Mössbauer spectrum of the ALB5SA00 sample.
[c] Parameter fixed at 0.26.

106

Table 4. Cation cluster OH stretch fundamental
absorptions in phlogopite and other micas at
frequencies ≥ 3600 cm^{-1}. Positions after Vedder
and Wilkins (1969), Farmer et al. (1971),
Farmer (1974), Robert and Kodama (1988),
Besson and Drits (1997), and Bishop et al. (2002).

Band position cm^{-1} (μm)	Cation Cluster Assignment
N-bands	
3735 (2.677)	Mg_3OH [a]
3712 (2.694)	Mg_3OH
3696 (2.706)	$Mg_2Fe^{2+}OH$
3680 (2.717)	$MgFe^{+2}_2OH$
3664 (2.729)	Fe^{2+}_3OH
I-bands	
3668 (2.726)	$Mg_2(Fe^{3+}, Al)OH$
3652 (2.738)	$MgFe^{2+}(Fe^{3+}, Al)OH$
3643 (2.745)	$Mg_2Fe^{3+}OH$ [b]
V-bands	
~3675 (2.721)	$Al_2[\ \ ]OH$ [c]
~3658 (2.734)	$Al_2[\ \ ]OH$ [d, e]
~3652 (2.738)	$AlFe^{3+}[\ \ ]OH$ [c]
~3641 (2.746)	$Al_2[\ \ ]OH$ [d, e]
~3631 (2.754)	$Fe^{3+}_2[\ \ ]OH$ [c]
~3621 (2.762)	$Al_2[\ \ ]OH$ [d]
~3620 (2.762)	$MgAl[\ \ ]OH$
~3600 (2.777)	$MgFe^{3+}[\ \ ]OH$

Notes: [a] Observed position in tetrasilicic Mg-mica.
[b] Observed in heated, partially dehydroxylated Al-Fe phlogopite.
[c] Observed position in dioctahedral micas with
  interlayer cation deficiencies.
[d] Observed position in dioctahedral micas.
[e] Absorption increases in intensity as Al content increases.

107

Table 5. Summary of OH-related mid-infrared (MIR) spectral features of unexpanded and expanded vermiculite ores.

Absorption type (keyed to figures)	Vibrational assignment (cation cluster)	Phlogopite	Hydrobiotite	Vermiculite
MIR vibrational absorptions in cm^{-1} (and µm) from deconvolution modeling [a]				
Octahedral layer OH stretches				
ν_1	Mg$_3$OH:Si$_4$Al$_2$ collapsed [b]	----	----	3741 (2.673)
ν_2	Mg$_3$OH:Si$_5$Fe^{3+} repulsed [c]	----	----	3739 (2.674)
ν_a	Mg$_3$OH:Si$_5$Al repulsed [d]	3718 (2.690)	3719 (2.689)	3718 (2.690)
ν_b	Mg$_3$OH:Si$_4$Al$_2$ repulsed	3708 (2.697)	3707 (2.698)	3708 (2.697)
ν_c	Mg$_2$Fe^{2+}OH repulsed	3697 (2.705)	3696 (2.706)	----
ν_d	Mg$_3$OH:Si$_5$Al non-repulsed [e]	----	3680 (2.717)	3681 (2.717)
ν_e	Mg$_3$OH:Si$_4$Al$_2$ non-repulsed	----	3671 (2.724)	3672 (2.723)
ν_f	Mg$_2$(Fe^{3+}, Al, Ti)OH:Si$_5$Al repulsed	3666 (2.728)	3663 (2.730)	3663 (2.730)
ν_g	Mg$_2$(Fe^{3+}, Al, Ti)OH:Si$_4$Al$_2$ repulsed	3655 (2.736)	3654 (2.737)	----
ν_3	MgAl[ ]OH [f]	----	3647 (2.742)	3647 (2.742)
ν_h	Mg$_2$(Fe^{3+}, Al, Ti)OH:Si$_5$Al non-repulsed	----	----	3633 (2.752)
ν_i	MgFe^{3+}[ ]OH:Si$_5$Al [g]	3623 (2.760)	3625 (2.759)	3627 (2.757)
ν_j	Mg$_2$(Fe^{3+},Al,Ti)OH: Si$_4$Al$_2$ non-repulsed	----	3621 (2.762)	3621 (2.762)
ν_k	MgFe^{3+}[ ]OH:Si$_4$Al$_2$ [g]	3618 (2.764)	3616 (2.765)	3612 (2.769)
Octahedral layer out-of-plane cation-OH bends				
δ_a	Mg$_3$OH:Si$_5$Al repulsed	588 (17.01)	591 (16.91)	591 (16.91)
δ_b	Mg$_3$OH:Si$_4$Al$_2$ repulsed	615 (16.26)	618 (16.17)	612 (16.34)
δ_c	Mg$_2$Fe^{2+}OH repulsed	636 (15.71)	642 (15.56)	----
δ_d	Mg$_3$OH:Si$_5$Al non-repulsed	----	632 (15.82)	632 (15.82)
δ_e	Mg$_3$OH:Si$_4$Al$_2$ non-repulsed	----	675 (14.81)	674 (14.84)
δ_f	Mg$_2$(Fe^{3+}, Al, Ti)OH:Si$_5$Al repulsed	708 (14.13)	710 (14.09)	710 (14.09)
δ_g	Mg$_2$(Fe^{3+}, Al, Ti)OH:Si$_4$Al$_2$ repulsed	733 (13.64)	----	----
δ_h	Mg$_2$(Fe^{3+}, Al, Ti)OH:Si$_5$Al non-repulsed	----	738 (13.56)	739 (13.54)
δ_i	MgFe^{3+}[ ]OH:Si$_5$Al [g]	851 (11.75)	852 (11.74)	856 (11.68)
δ_j	Mg$_2$(Fe^{3+}, Al)OH: Si$_4$Al$_2$ non-repulsed	----	765(13.08)	763 (13.10)
δ_3	MgAl[ ]OH [f]	838 (11.93)	838 (11.93)	838 (11.93)
δ_k	MgFe^{3+}[ ]OH:Si$_4$Al$_2$ [g]	868 (11.52)	870 (11.50)	869 (11.51)
Octahedral layer in-plane cation-OH bends				
δ_a'	Mg$_3$OH:Si$_5$Al repulsed	495 (20.21)	491 (20.38)	----
δ_b'	Mg$_3$OH:Si$_4$Al$_2$ repulsed	517 (19.33)	519 (19.25)	520 (19.22)
δ_c'	Mg$_2$Fe^{2+}OH repulsed	560 (17.87)	563 (17.75)	----
δ_d'	Mg$_3$OH:Si$_5$Al non-repulsed	----	501 (19.95)	505 (19.80)
δ_e'	Mg$_3$OH:Si$_4$Al$_2$ non-repulsed	----	537 (18.63)	547 (18.28)
δ_f'	Mg$_2$(Fe^{3+}, Al, Ti)OH:Si$_5$Al repulsed	614 (16.29)	604 (16.55)	----
δ_g'	Mg$_2$(Fe^{3+}, Al, Ti)OH:Si$_4$Al$_2$ repulsed	674 (14.84)	----	----

Notes: Vibrational positions from spectra of handpicked, ground mica flakes from the unexpanded GDS469 ore sample from Libby, MT; the unexpanded ALB5SA00 ore sample from Palabora, S. Africa; and the expanded vermiculite ores as noted. Vibrational assignments from Beran et al. (2002), Besson and Drits (1997), Farmer et al. (1971), Fechtelkord et al. (2003), Jenkins (1989), Papin et al. (1997), Serratosa et al. (1970), Vedder and Wilkins (1969), Wunder and Melzer (2002), and this study. ν_a = OH stretch, δ_a = out-of-plane cation-OH bend, and δ_a' = in-plane cation-OH bend fundamental absorptions. [ ] = vacant octahedral cation site. ---- = absorption not observed. ν_1 and ν_3 absorptions observed in spectra of expanded vermiculite ore caused by heating (see Fig. 15b); ν_2 = absorption observed in unexpanded ore ALB5SA00 (see Fig. 15a), which has 37% of its Fe as Fe^{3+} in tetrahedral sites according to electron probe microanalysis and Mössbauer analysis.

[a] Wavelength positions of absorptions based on Gaussian-Lorentizian area (fixed shape, variable width) deconvolution using Peakfit® v4.12.

[b] Collapsed = increased dehydration-induced repulsion of hydroxyl hydrogen by adjacent interlayer divalent cations that were water-coordinated prior to heating-induced expansion of vermiculite ore.

[c] Higher frequency shift of absorption likely due to Fe^{3+} in tetrahedral layer.

[d] Repulsed = repulsion of hydroxyl hydrogen by positive charge of adjacent interlayer cations.

[e] Non-repulsed = no repulsion of hydroxyl hydrogen due to lack of adjacent interlayer cations.

[f] Assignment based on presence of this absorption in spectra of the expanded vermiculite ore samples ALB22SC00, South Carolina; GDS847, Louisa, Virginia; and GDS909, Libby, Montana (Figs. 15b and 19); and in the spectrum of an unexpanded Mg-vermiculite VTx-1 sample from Llano, Texas (see appendix discussion and Fig. A6).

[g] Assigned to $MgFe^{3+}$[ ]OH vacancy cation clusters based on the absence of these absorptions in the Mg- and Al-rich, Fe-poor Llano, Texas, vermiculite sample (see appendix discussion and Fig. A6).

Table 6. Summary of OH-related near-infrared spectral features of unexpanded and expanded vermiculite ores.

Absorption type (keyed to figures)	Vibrational Assignment	Phlogopite	Hydrobiotite	Vermiculite
NIR vibrational absorptions in μm (and cm^{-1}) from deconvolution modeling [a]				
Octahedral layer OH stretch overtones				
o_a	$2\nu_a$ Mg$_3$OH:Si$_5$Al repulsed [b]	1.376 (7269)	1.375 (7274)	1.376 (7268)
o_b	$2\nu_b$ Mg$_3$OH:Si$_4$Al$_2$ repulsed	1.379 (7250)	1.380 (7249)	1.381 (7240)
o_c	$2\nu_c$ Mg$_2$Fe^{2+}OH repulsed	1.383 (7228)	1.384 (7226)	----
o_d	$2\nu_d$ Mg$_3$OH:Si$_5$Al non-repulsed [c]	----	1.390 (7197)	1.390 (7194)
o_e	$2\nu_e$ Mg$_3$OH:Si$_4$Al$_2$ non-repulsed	----	1.393 (7178)	1.393 (7178)
o_f	$2\nu_f$ Mg$_2$(Fe^{3+}, Al, Ti)OH:Si$_5$Al repulsed	1.394 (7172)	1.396 (7161)	1.397 (7159)
o_g	$2\nu_g$ Mg$_2$(Fe^{3+}, Al, Ti)OH:Si$_4$Al$_2$ repulsed	1.401 (7139)	1.400 (7142)	1.401 (7137)
o_3	$2\nu_3$ MgAl[ ] [d]	----	1.404 (7121)	----
o_h	$2\nu_h$ Mg$_2$(Fe^{3+}, Al, Ti)OH:Si$_5$Al non-repulsed	----	----	1.408 (7100)
o_i	$2\nu_i$ MgFe^{3+}[ ]OH:Si$_5$Al	----	1.412 (7084)	1.412 (7084)
o_j	$2\nu_j$ Mg$_2$(Fe^{3+}, Al, Ti)OH: Si$_4$Al$_2$ non-repulsed	----	1.417 (7075)	1.414 (7073)
o_k	$2\nu_k$ MgFe^{3+}[ ]OH:Si$_4$Al$_2$	----	1.416 (7064)	1.417 (7055)
Interlayer H$_2$O vibrations				
o_{H2O}	$2\nu_{H2O}$ interlayer water	----	1.417 (7057)	1.422 (7030)
o_{H2O}	$2\nu_{H2O}$ interlayer water	----	1.440 (6946)	1.442 (6934)
o_{H2O}	$2\nu_{H2O}$ interlayer water	----	1.474 (6783)	1.472 (6794)
o_{H2O}	$2\nu_{H2O}$ interlayer water	----	1.521 (6573)	1.504 (6650)
Octahedral layer out-of-plane cation-OH-bend-plus-stretch combinations				
c_a	$\nu_a + \delta_a$ Mg$_3$OH:Si$_5$Al repulsed	2.334 (4285)	2.333 (4286)	2.333 (4286)
c_b	$\nu_b + \delta_b$ Mg$_3$OH:Si$_4$Al$_2$ repulsed	2.323 (4304)	2.324 (4302)	2.323 (4304)
c_c	$\nu_c + \delta_c$ Mg$_2$Fe^{2+}OH repulsed	2.307 (4335)	2.310 (4330)	----
c_d	$\nu_d + \delta_d$ Mg$_3$OH:Si$_5$Al non-repulsed	----	2.318 (4313)	2.322 (4306)
c_e	$\nu_e + \delta_e$ Mg$_3$OH:Si$_4$Al$_2$ non-repulsed	----	2.301 (4346)	2.300 (4349)
c_f	$\nu_f + \delta_f$ Mg$_2$(Fe^{3+}, Al, Ti)OH:Si$_5$Al repulsed	2.293 (4361)	2.294 (4359)	2.292 (4362)
c_g	$\nu_g + \delta_g$ Mg$_2$(Fe^{3+}, Al, Ti)OH:Si$_4$Al$_2$ repulsed	2.278 (4390)	----	----
c_h	$\nu_h + \delta_h$ Mg$_2$(Fe^{3+}, Al, Ti)OH:Si$_5$Al non-repulsed	----	2.289 (4369)	2.288 (4371)
c_i	$\nu_i + \delta_i$ MgFe^{3+}[ ]OH:Si$_5$Al	----	----	----
c_j	$\nu_j + \delta_j$ Mg$_2$(Fe^{3+}, Al, Ti)OH: Si$_4$Al$_2$ non-repulsed	----	2.279 (4388)	2.280 (4386)
c_k	$\nu_k + \delta_k$ MgFe^{3+}[ ]OH:Si$_4$Al$_2$	2.246 (4453)	2.247 (4450)	2.246 (4451)
c_3	$\nu_3 + \delta_3$ MgAl[ ]OH [d]	----	2.245 (4453)	----
Octahedral layer in-plane cation-OH-bend-plus-stretch combinations				
c_a'	$\nu_a + \delta_a$' Mg$_3$OH:Si$_5$Al repulsed	2.390 (4184)	2.390 (4185)	2.390 (4183)
c_b'	$\nu_b + \delta_b$' Mg$_3$OH:Si$_4$Al$_2$ repulsed	2.380 (4201)	2.381 (4200)	2.382 (4198)
c_c'	$\nu_c + \delta_c$' Mg$_2$Fe^{2+}OH repulsed	2.363 (4232)	2.363 (4232)	----
c_d'	$\nu_d + \delta_d$' Mg$_3$OH:Si$_5$Al non-repulsed	----	2.392 (4181)	2.390 (4183)
c_e'	$\nu_e + \delta_e$' Mg$_3$OH:Si$_4$Al$_2$ non-repulsed	----	2.359 (4240)	2.360 (4236)
c_f'	$\nu_f + \delta_f$' Mg$_2$(Fe^{3+}, Al, Ti)OH:Si$_5$Al repulsed	2.352 (4252)	2.347 (4261)	2.354 (4248)
c_g'	$\nu_g + \delta_g$' Mg$_2$(Fe^{3+}, Al, Ti)OH:Si$_4$Al$_2$ repulsed	2.331 (4290)	----	----

110

Octahedral layer OH stretch + framework vibrations?

c_a"	$\nu_a + \delta_a$" $Mg_3OH:Si_5Al$ repulsed	2.448 (4086)	----	----
c_b"	$\nu_b + \delta_b$" $Mg_3OH:Si_4Al_2$ repulsed	2.434 (4109)	----	----
c_c"	$\nu_c + \delta_c$" $Mg_2Fe^{2+}OH$ repulsed	2.419 (4134)	---	---
c_d"	$\nu_d + \delta_d$" $Mg_3OH:Si_5Al$ non-repulsed	----	2.439 (4099)	2.434 (4108)
c_e"	$\nu_e + \delta_e$" $Mg_3OH:Si_4Al_2$ non-repulsed	----	2.411 (4148)	2.409 (4150)
c_f"	$\nu_f + \delta_f$" $Mg_2(Fe^{3+}, Al, Ti)OH:Si_5Al$ repulsed	2.409 (4151)	2.411 (4148)	----
c_l	$\nu + \delta$'" Mg_3OH	2.473 (4044)	----	----
c_m	$\nu + \delta$'" Mg_3OH	2.505 (3992)	----	----
c_n	$\nu + \delta$'" Mg_3OH	2.561 (3904)	----	----

Notes: Vibrational positions from spectra of handpicked, ground mica flakes from the unexpanded GDS469 ore sample from Libby, MT; and the expanded vermiculite ores as noted. Vibrational assignments from this study. o_a = OH overtone; c_a = out-of-plane cation-OH-bend-plus-stretch combination absorption and c_a' = in-plane cation-OH-bend-plus-stretch combination absorption. ν_a = OH stretch, δ_a = out-of-plane cation-OH bend, and δ_a' = in-plane cation-OH bend fundamental absorptions (positions listed in Table 5). δ_a" and δ'" = possible framework modes. [ ] = vacant octahedral cation site. ---- = absorption not observed.
[a] Wavelength positions of absorptions based on Gaussian-Lorentizian area (fixed shape, variable width) deconvolution using Peakfit® v4.12. Gaussian-Lorentizian curves used for modeling OH and interlayer water absorptions in the 1.4-μm region required use of variable shapes and widths to achieve reasonable fits.
[b] Repulsed = repulsion of hydroxyl hydrogen by positive charge of an adjacent interlayer cation.
[c] Non-repulsed = no repulsion of hydroxyl hydrogen due to lack of an adjacent interlayer cation.
[d] Assignment based on presence of these absorptions in the spectrum of the expanded ALB22SC00 ore sample from Enoree, South Carolina (Figs. 19 and 20).

111

Table 7. Accuracy of expanded vermiculite ore spectral source determinations and impurity detections.

Vermiculite Source	No. Samples	Spectral misidentification of vermiculite provenance (No. of samples)	Percent of expanded vermiculite ore samples with amphibole, talc, and/or serpentine impurities: Detection methods [a]			
			MCM Bundles (%)	SEM-EDS Elongate (%)	Any Shape (%)	Spectral Band Depth Ratio (%)
Louisa	5	0	0	40	100	80
Enoree	8	1 [b]	40 [c]	63	75	100
Libby	23	0 [d]	100	100	100	100
Palabora	8	1 [e]	0 [c]	13	25	50
Mixtures	6	0	20 [c]	67	83	50
Jiangsu	1	0	---- [f]	100	100	100
Unknown	1	0	100	100	100	100

Notes: Samples evaluated for impurities using the Modified Cincinnati Method (MCM) with separates examined by Scanning Electron Microscope – Energy-Dispersive X-Ray Spectroscopy (SEM-EDS) for the presence of amphibole, talc, and/or serpentine, and using the spectral 1.40/1.42-μm band depth ratio.

[a] Details of MCM, electron probe microanalysis (EPMA), spectroscopy, XRD, and SEM-EDS analyses for expanded vermiculite ore samples can be found in Swayze et al. (2018).

[b] The expanded Enoree GDS651 sample has no detectable 1.38-μm absorption, so its symbol plots on the zero 1.38/2.32-μm band-depth-ratio line as do the Louisa sample symbols.

[c] Only three of the expanded Enoree samples, one expanded Palabora sample, and one expanded "Mixtures" sample had sufficient volume for using the MCM for separating amphibole bundles.

[d] The GDS629 sample was misidentified as an expanded Libby ore when it was actually a mixture of expanded Palabora and Enoree ores. The 2.24-μm band position test (Fig. 21) reduces these types of false positive identifications (see text for details).

[e] Three EPMA spot analysis values fall in the Enoree provenance field suggesting that the GDS327 sample is actually a mixture of expanded Palabora and Enoree ores and not just an expanded Palabora ore as indicated by spectroscopy.

[f] The expanded Jiangsu sample had insufficient volume for using the MCM.
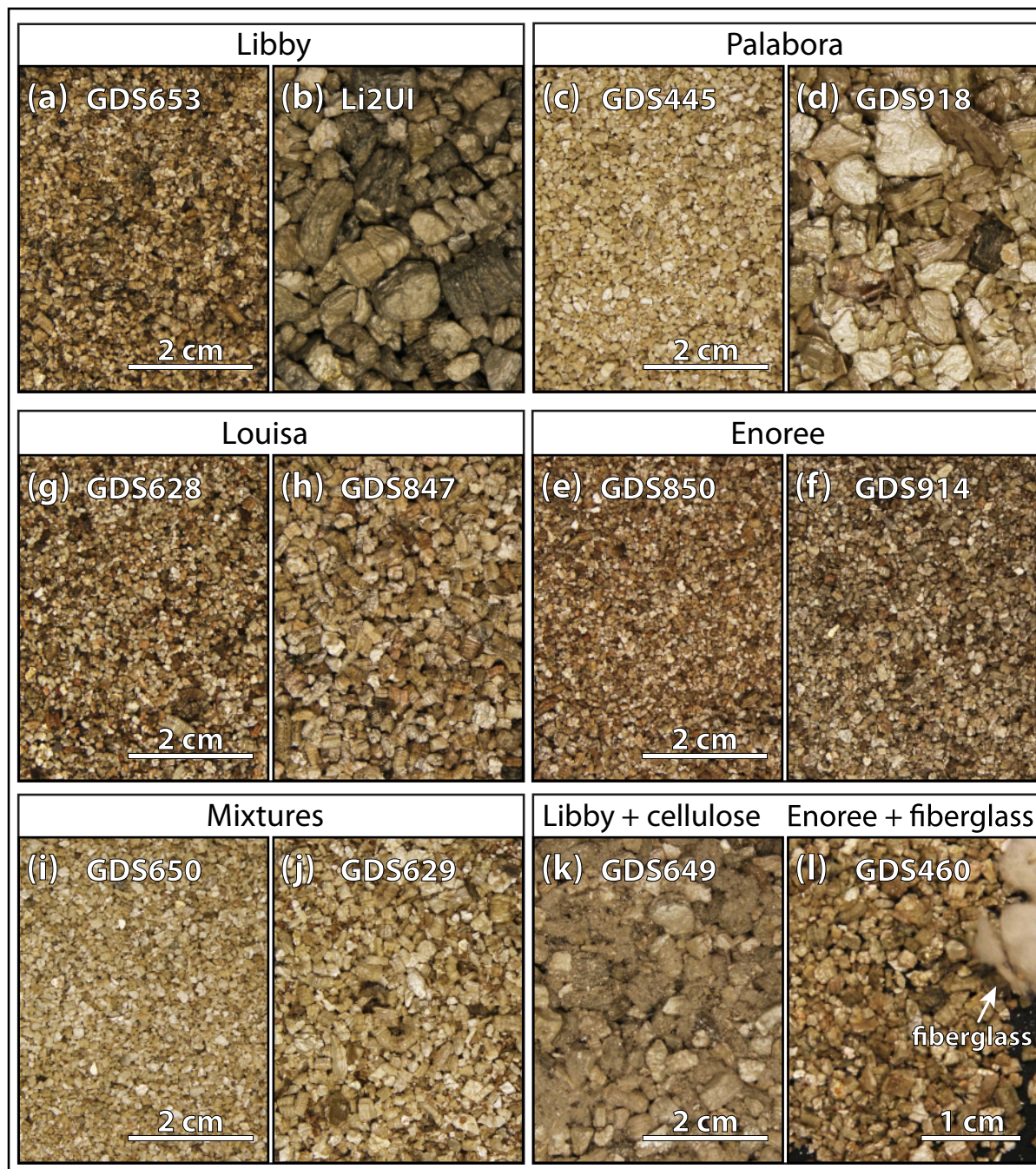
Swayze et al.   Figure 2
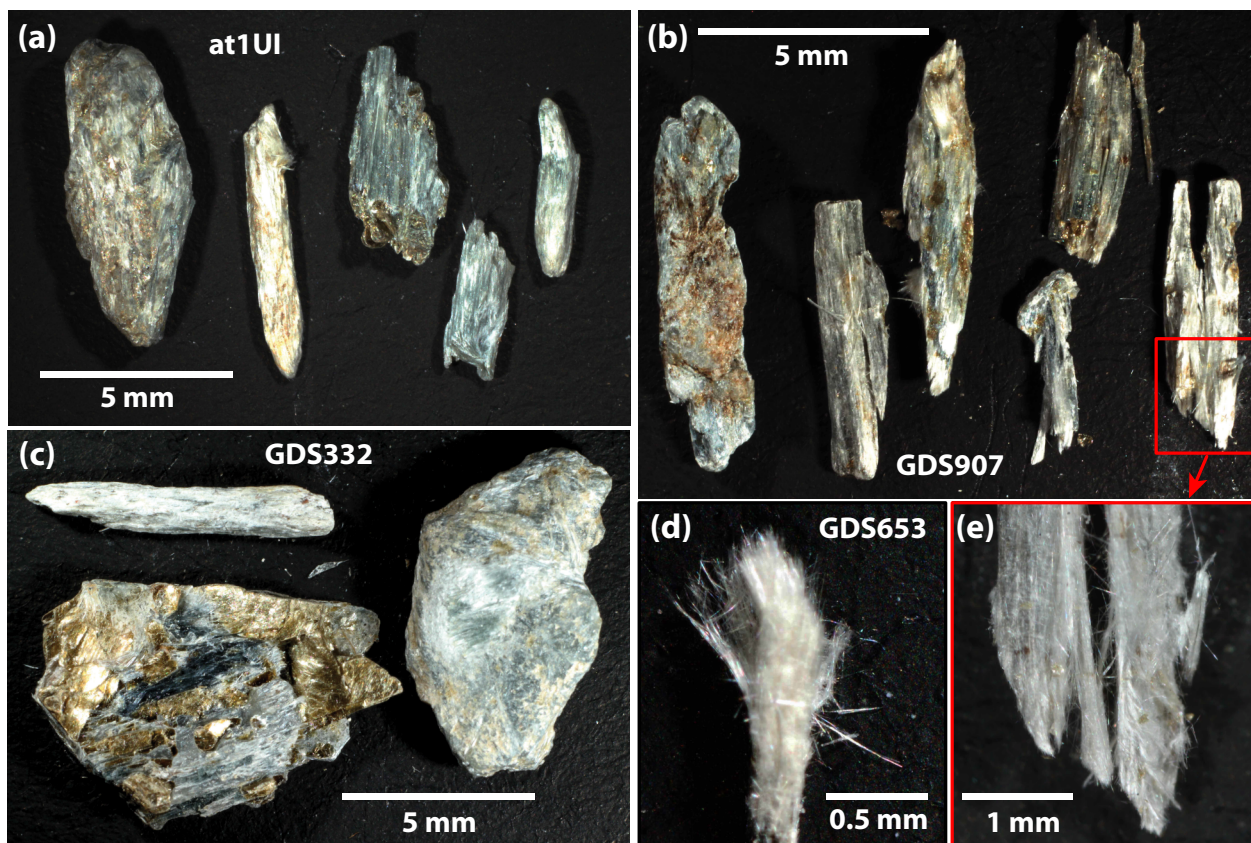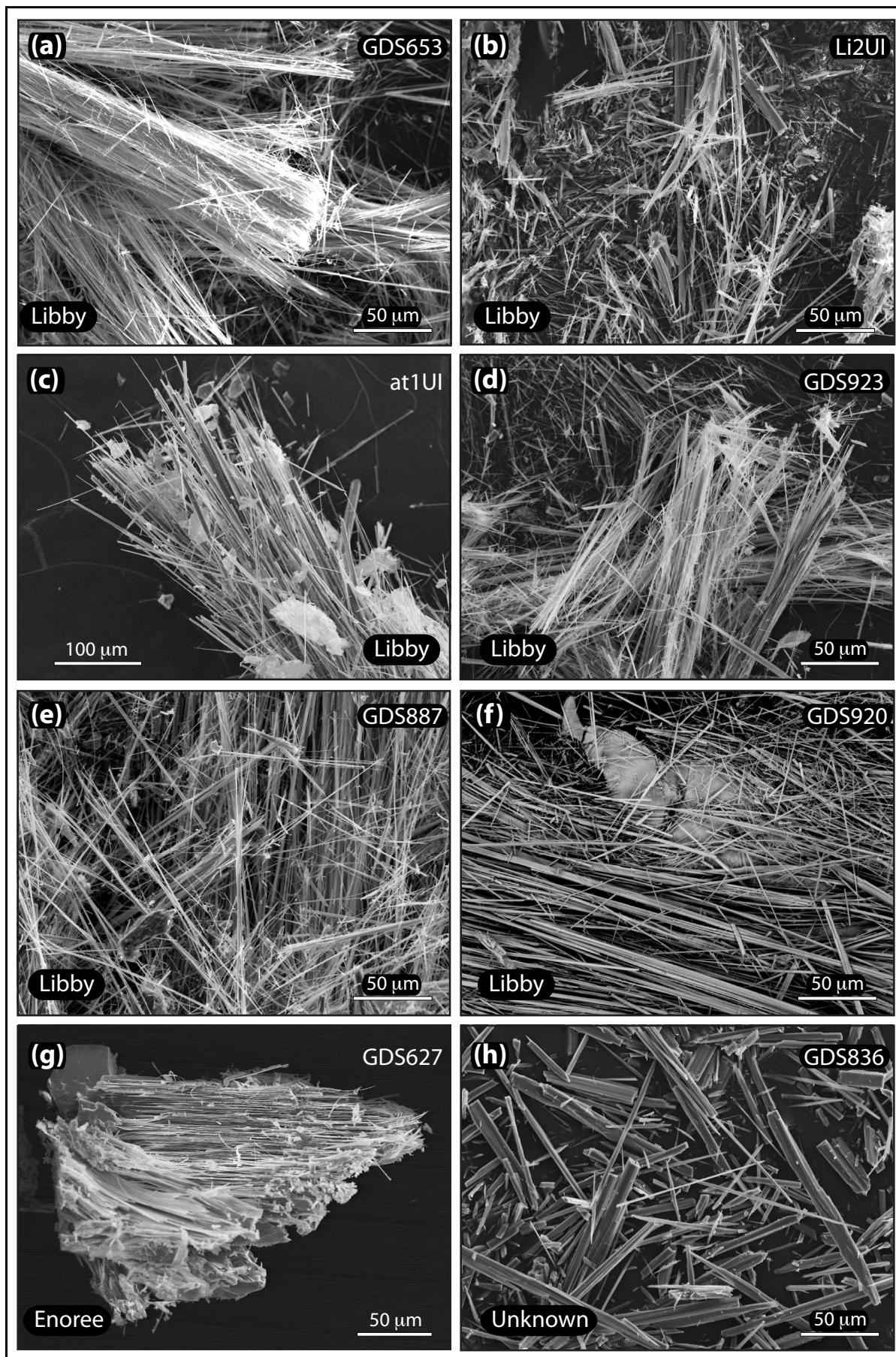
Swayze et al.   Figure 4
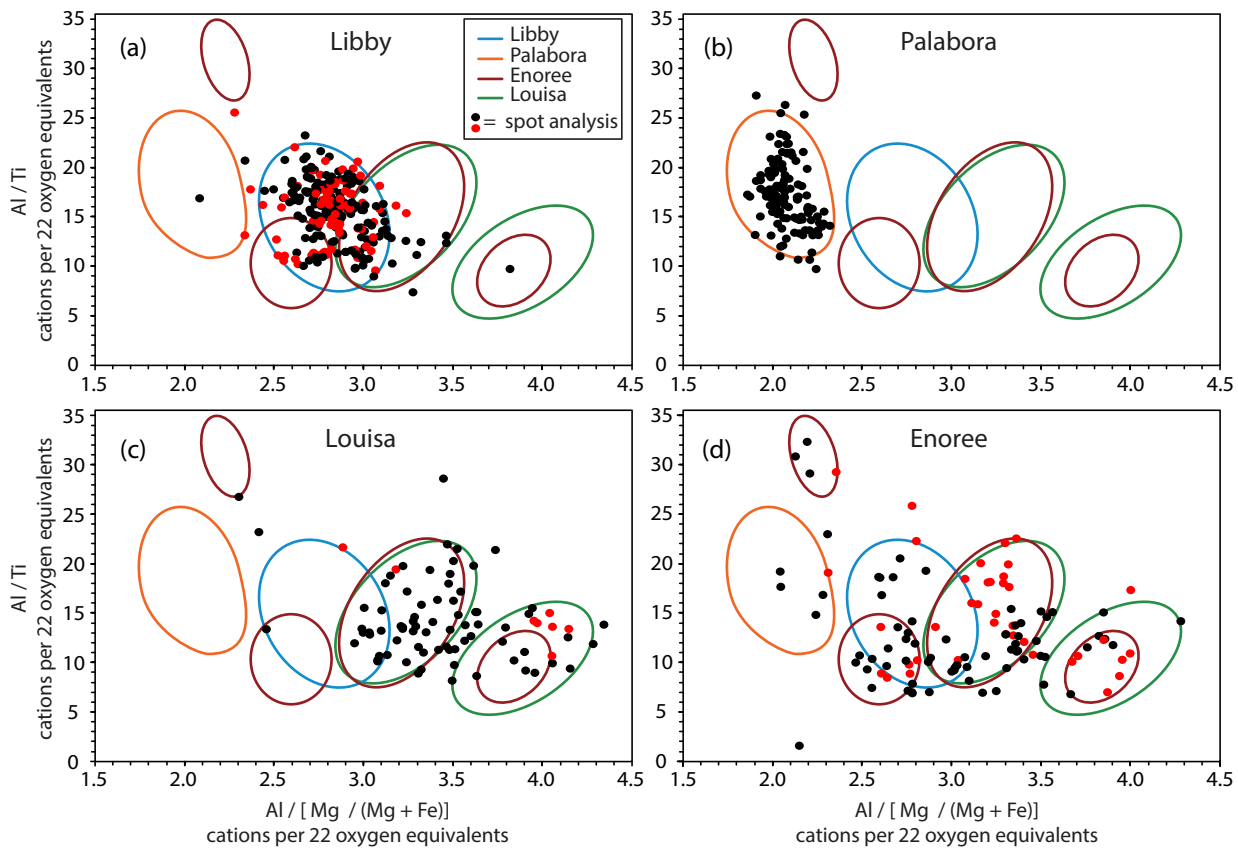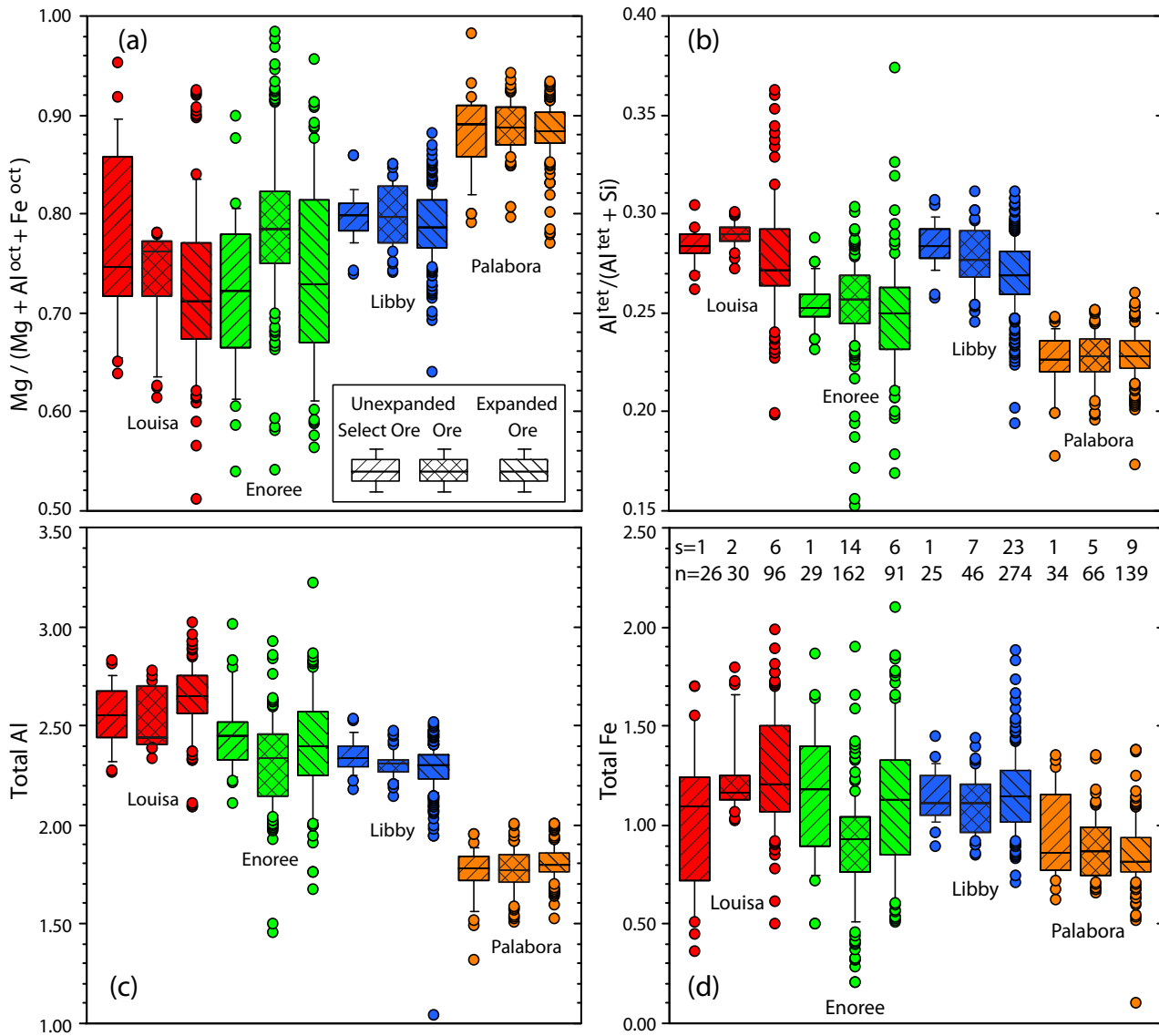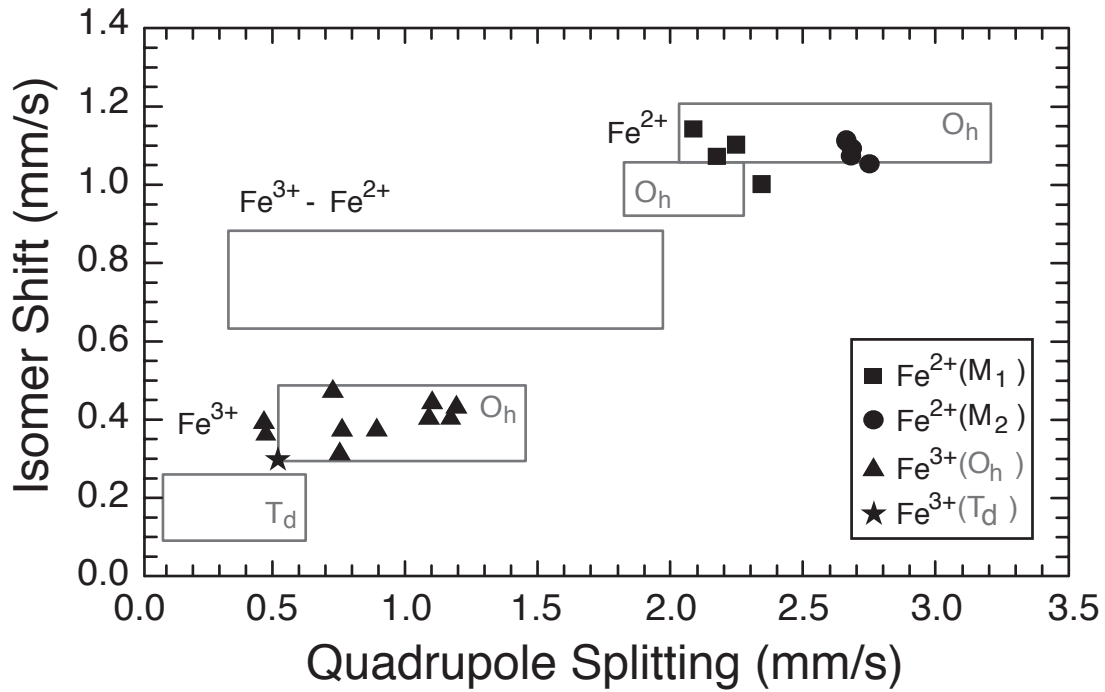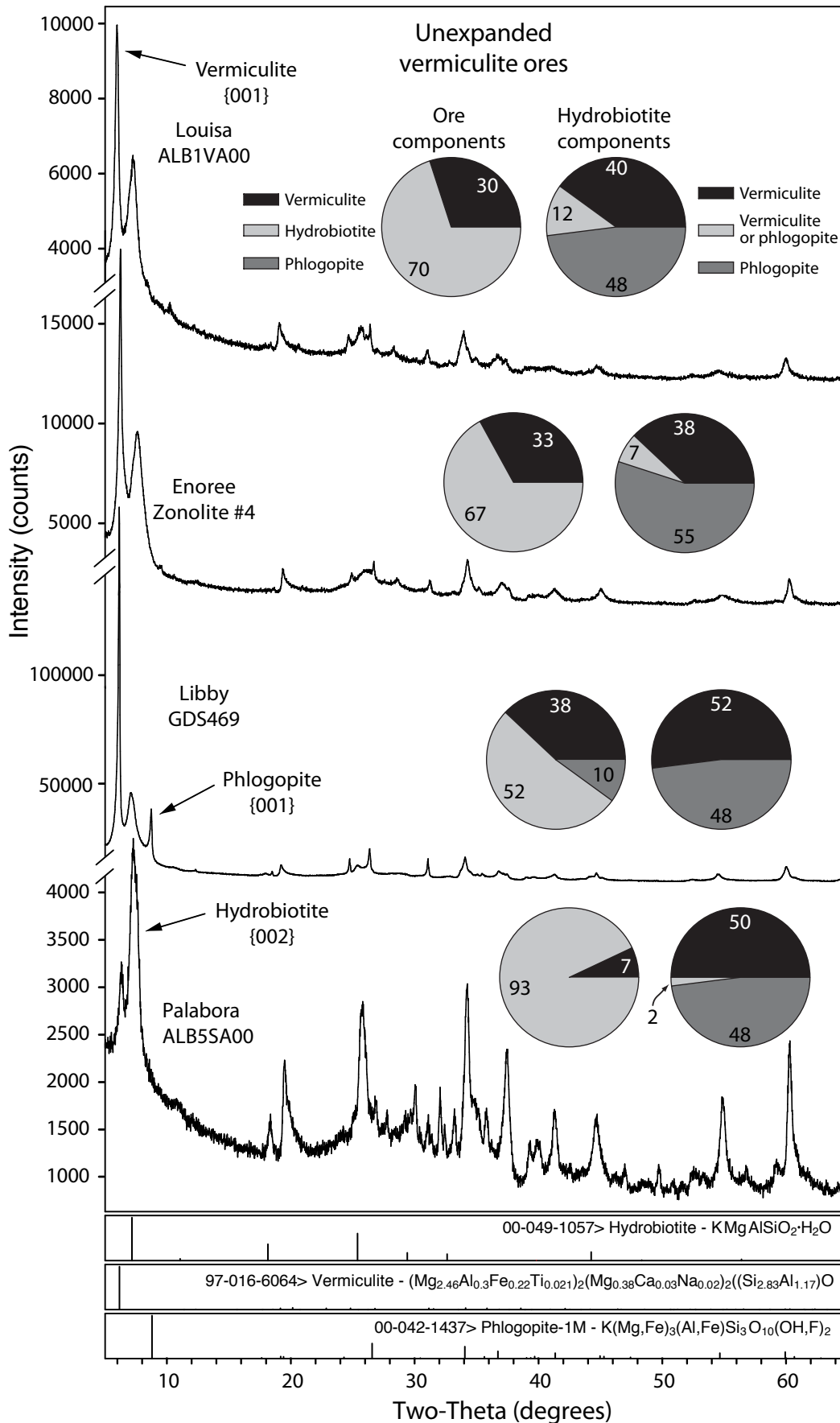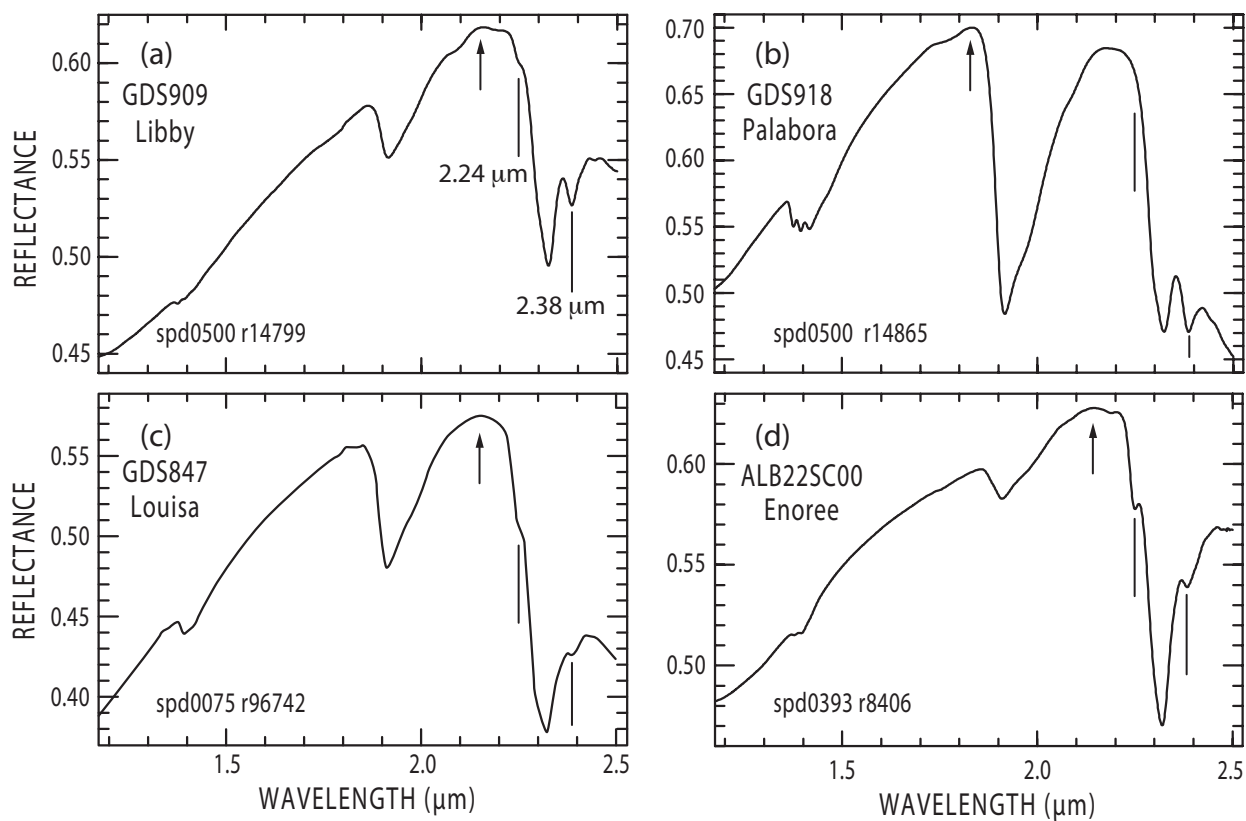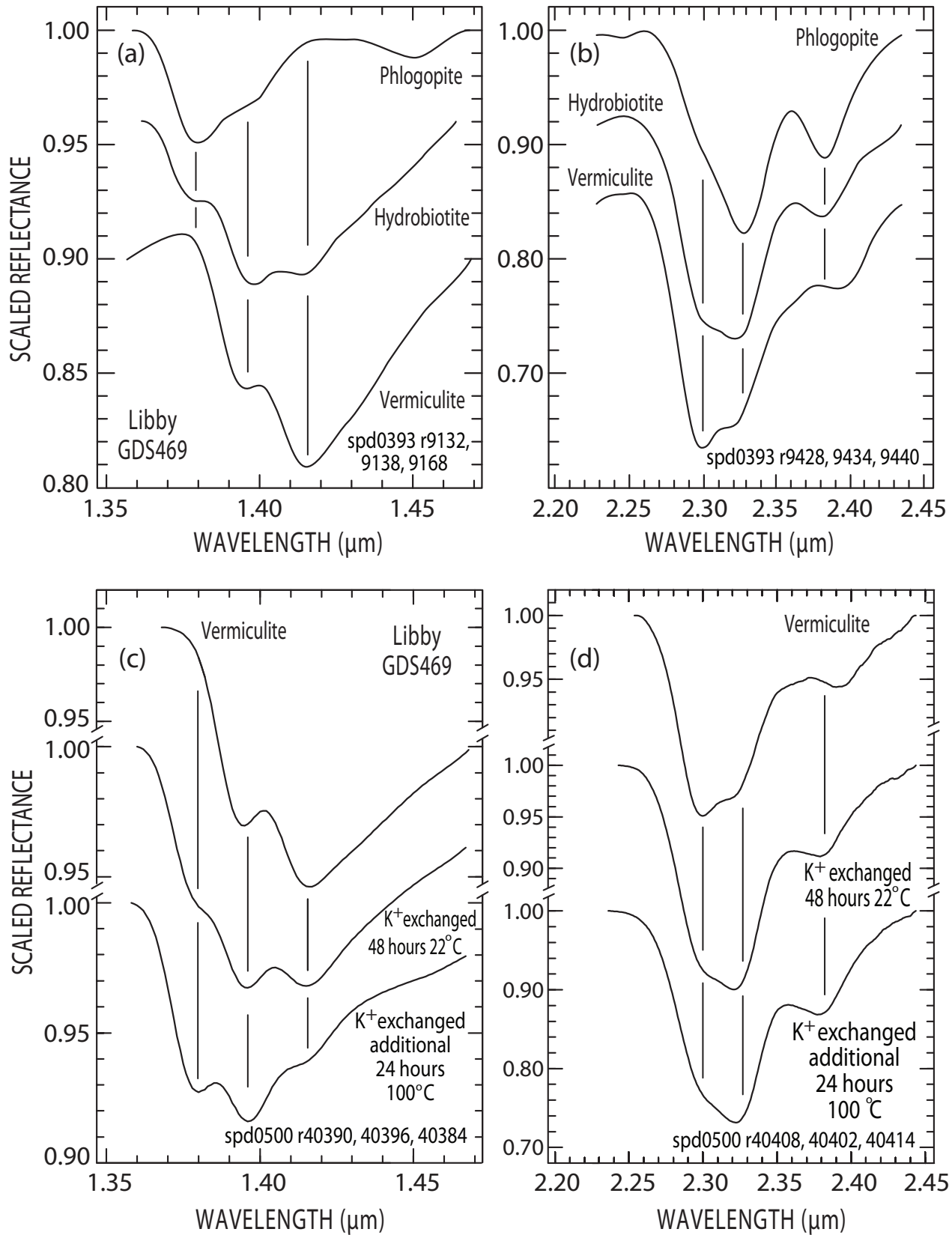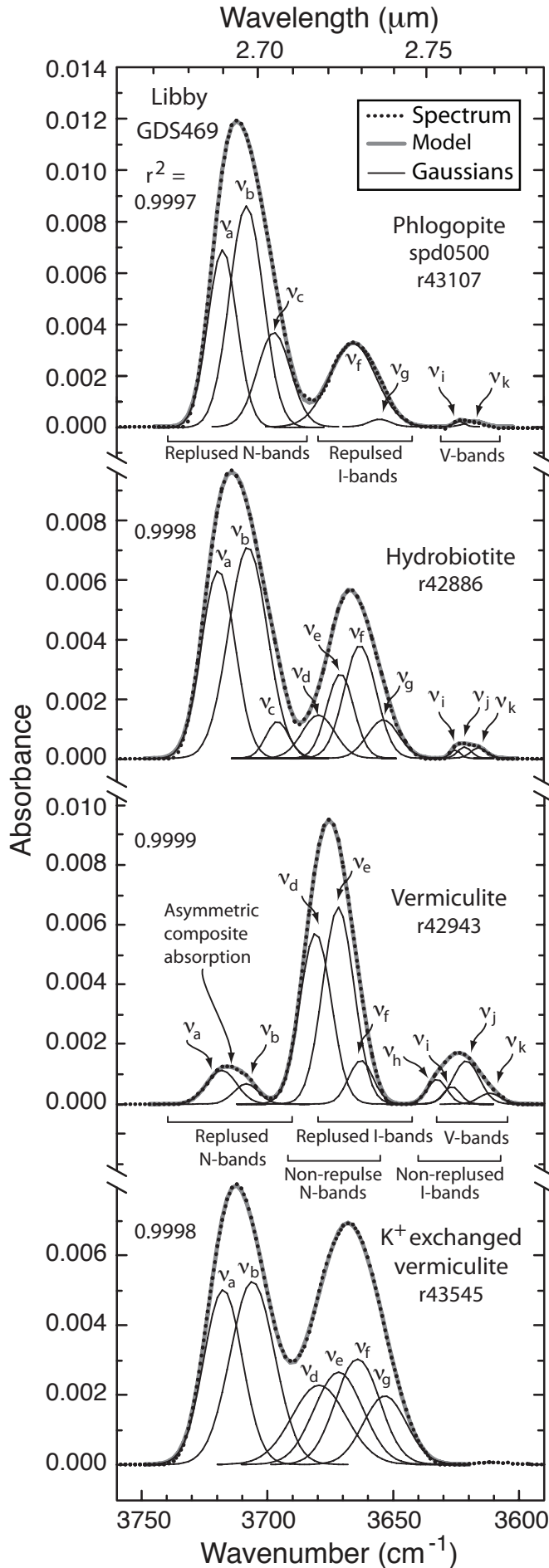
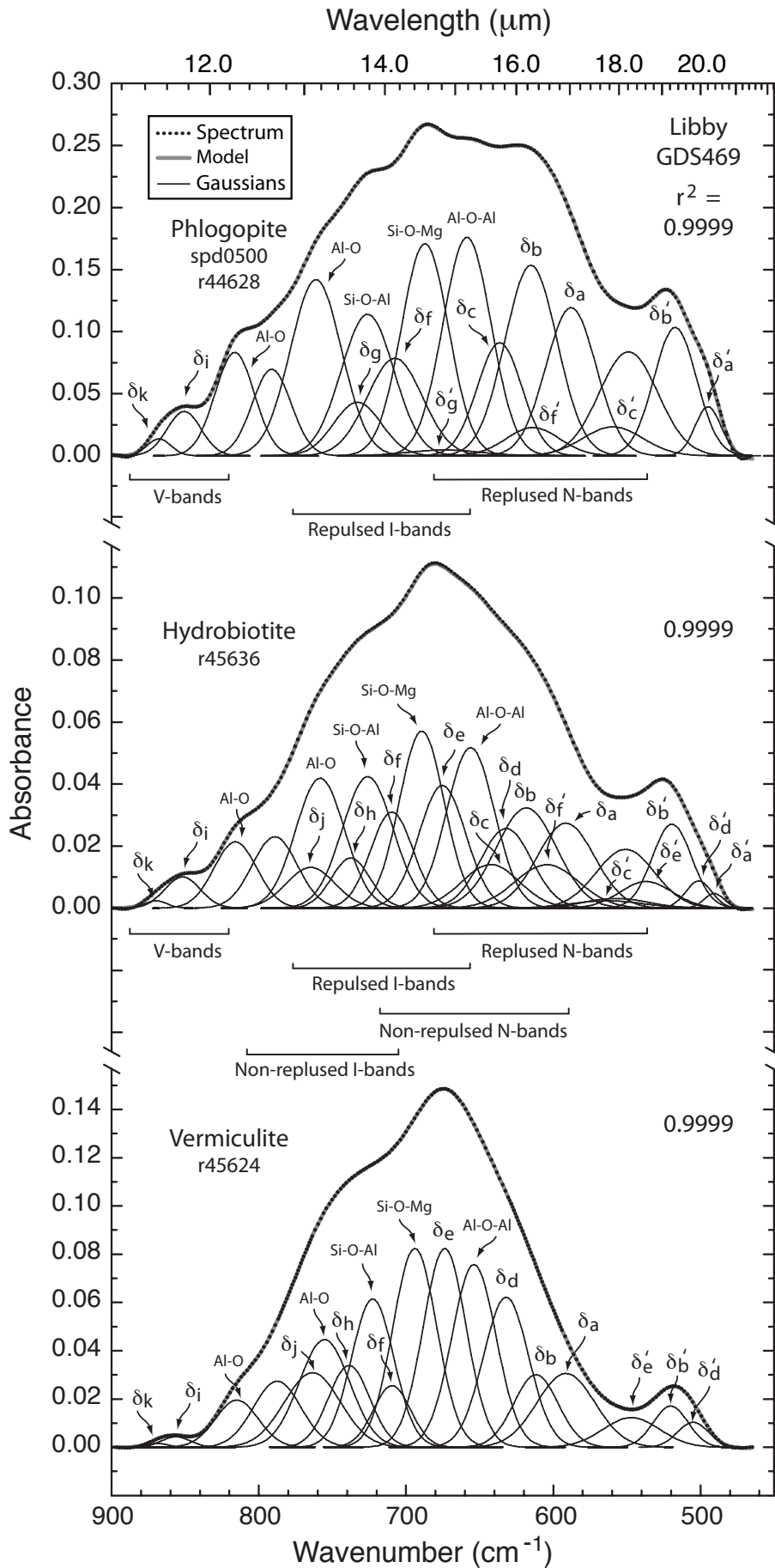Swayze et al.   Figure 8
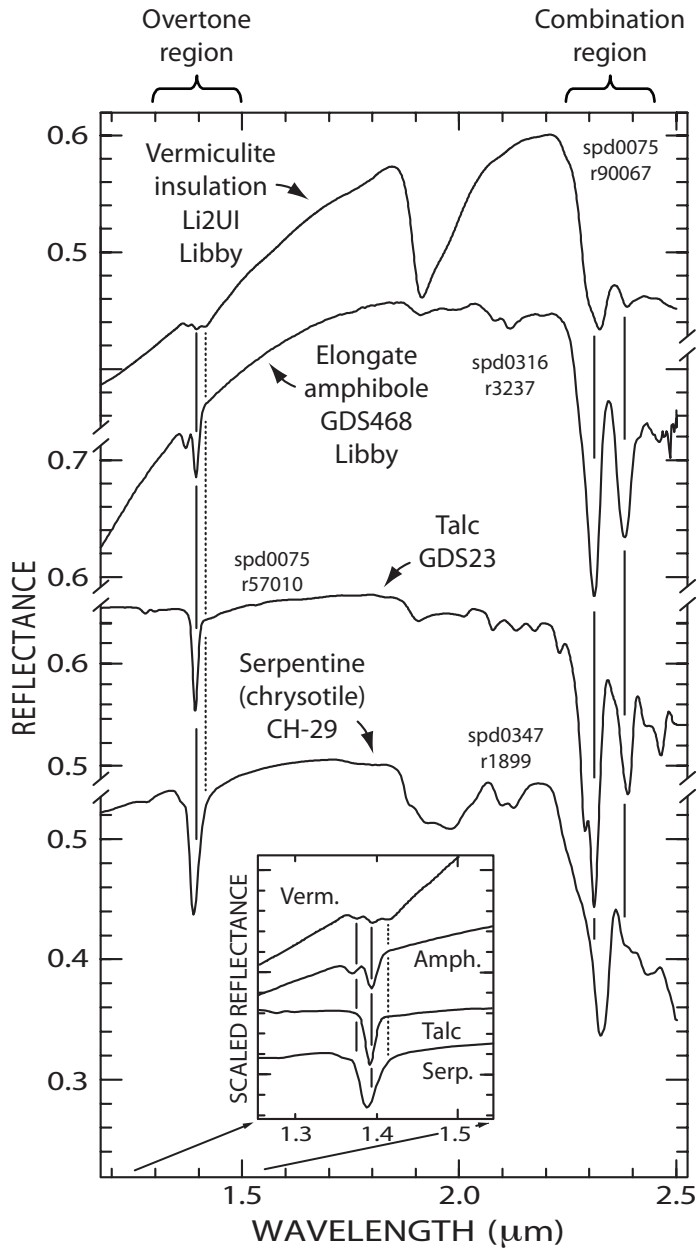
Swayze et al.   Figure 9

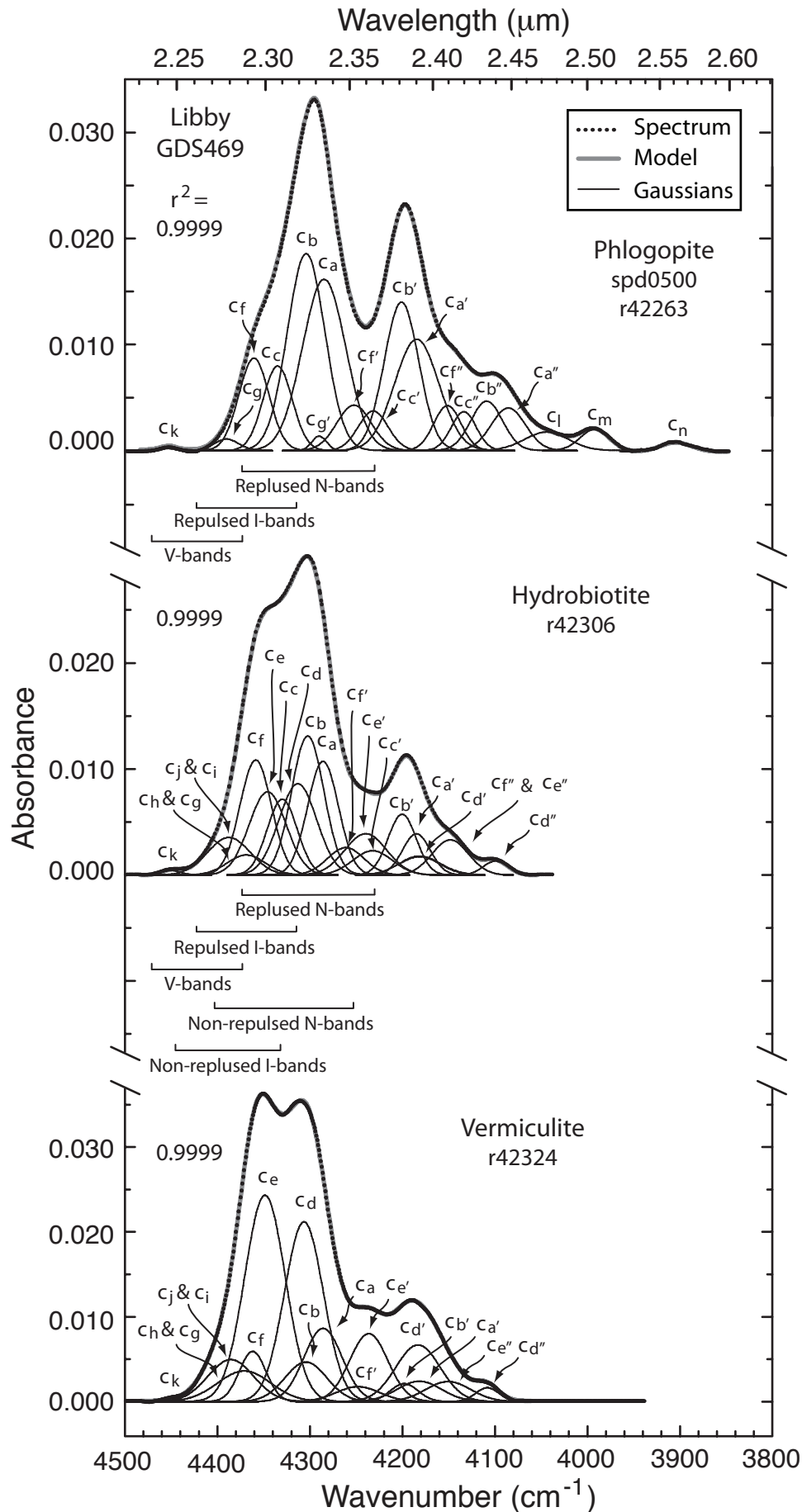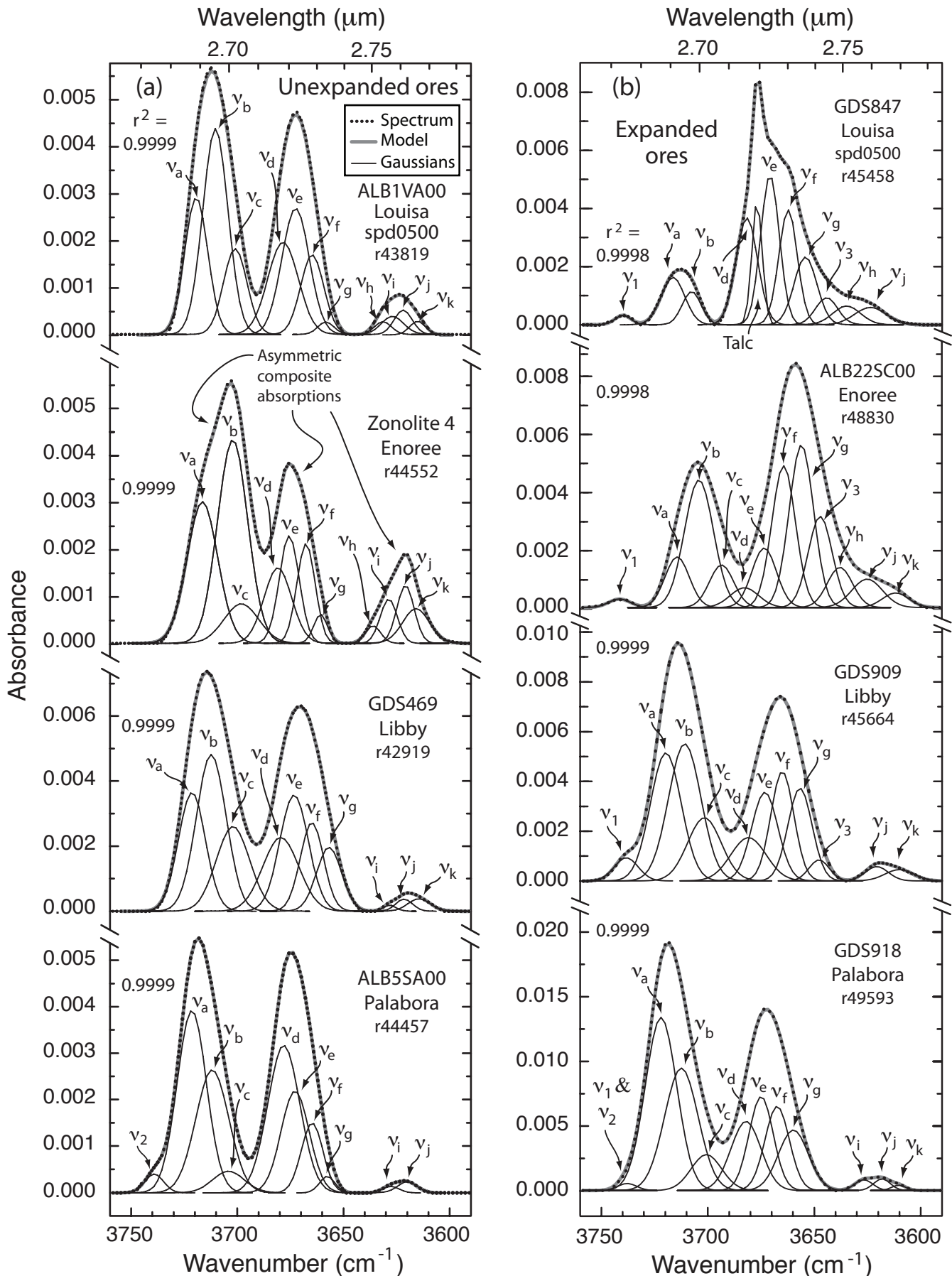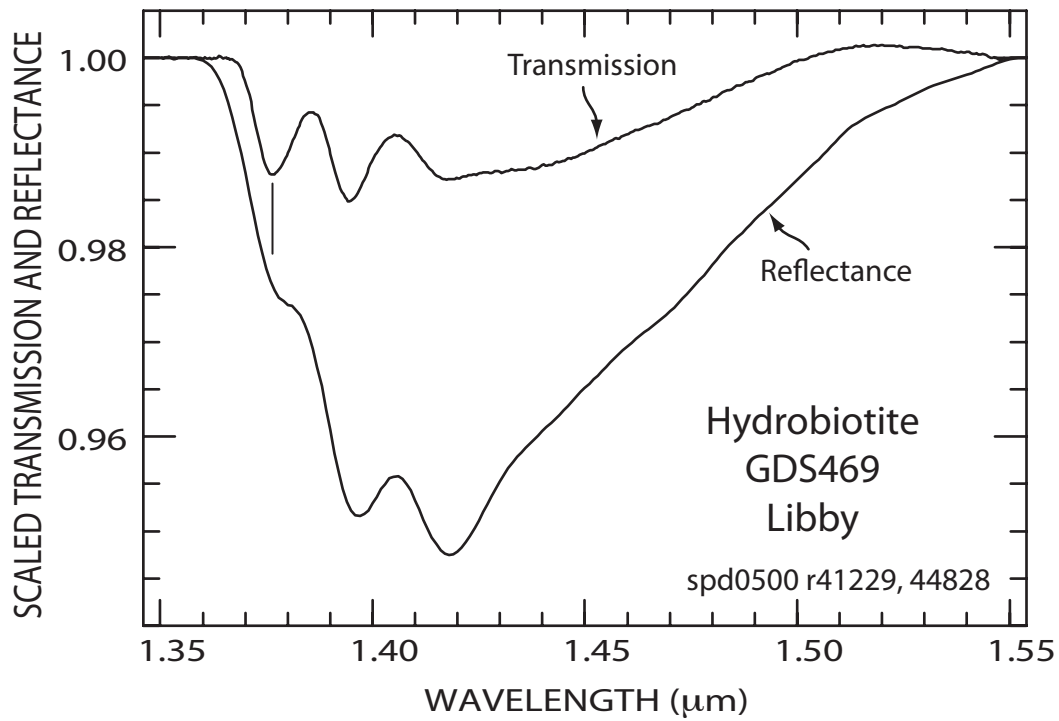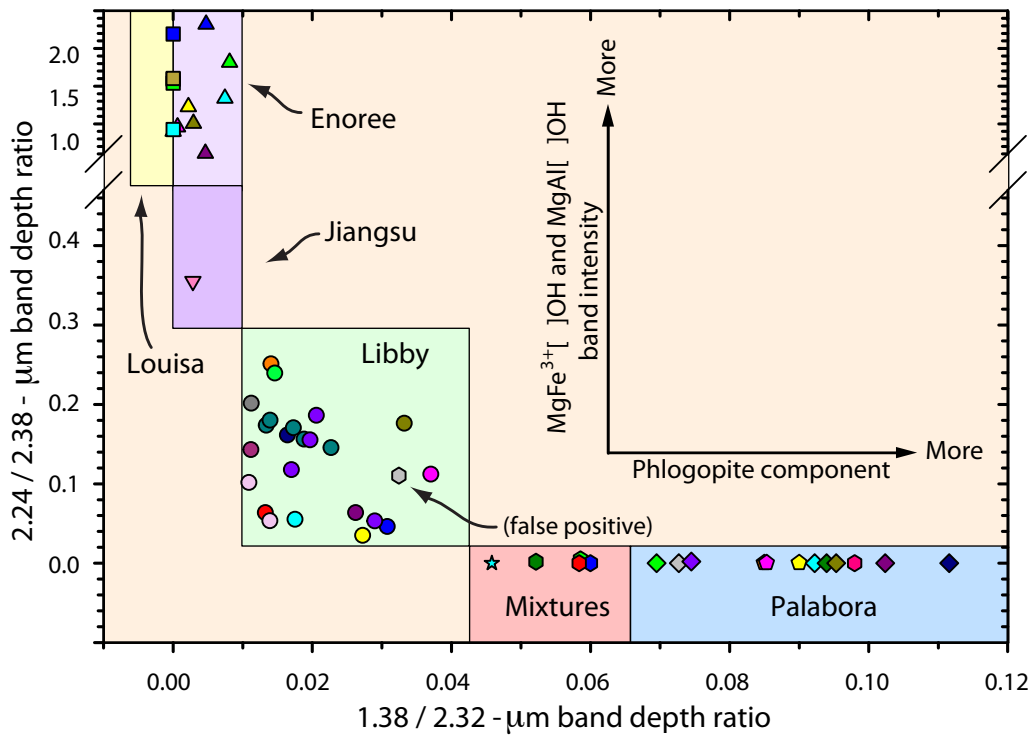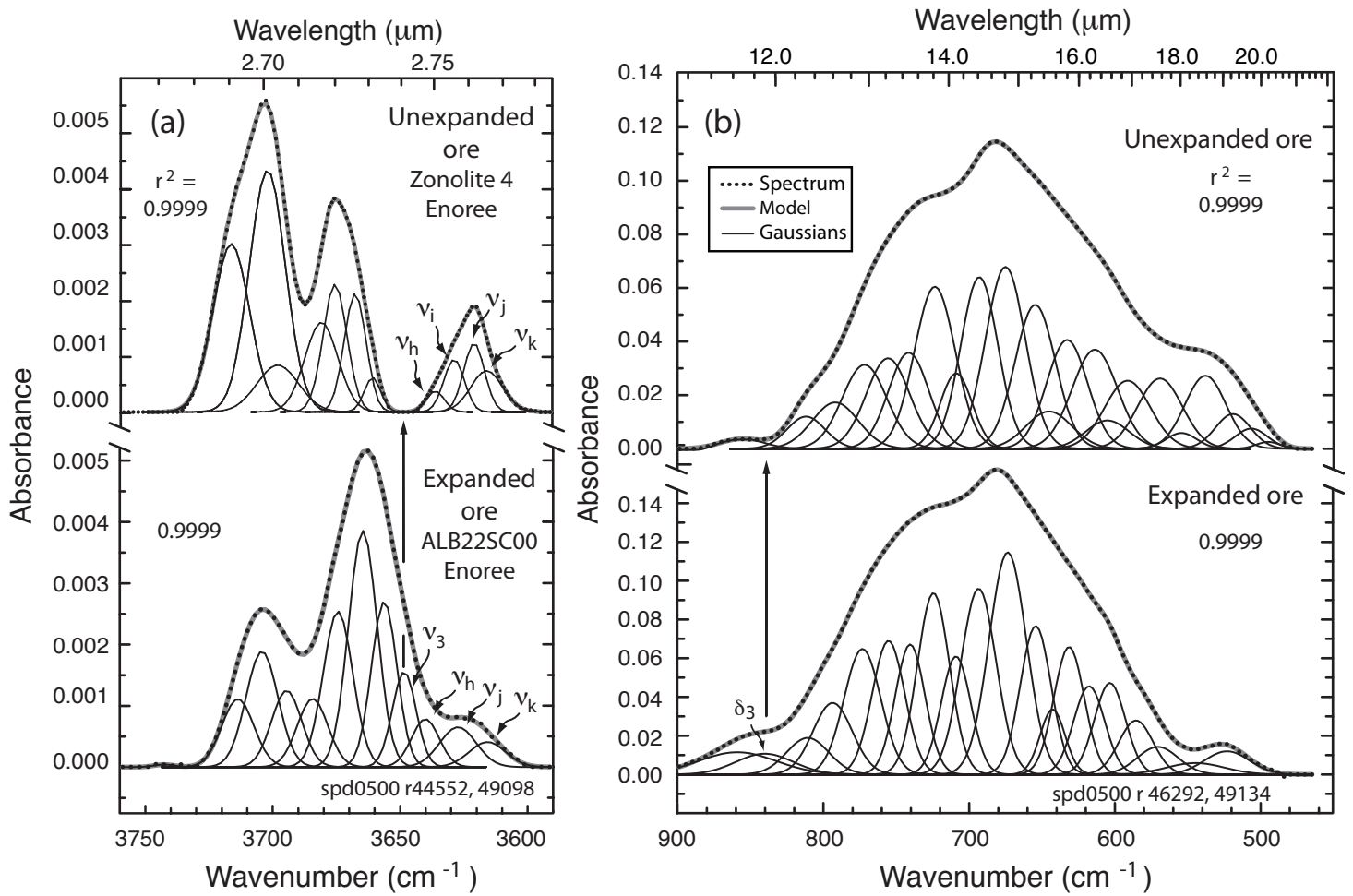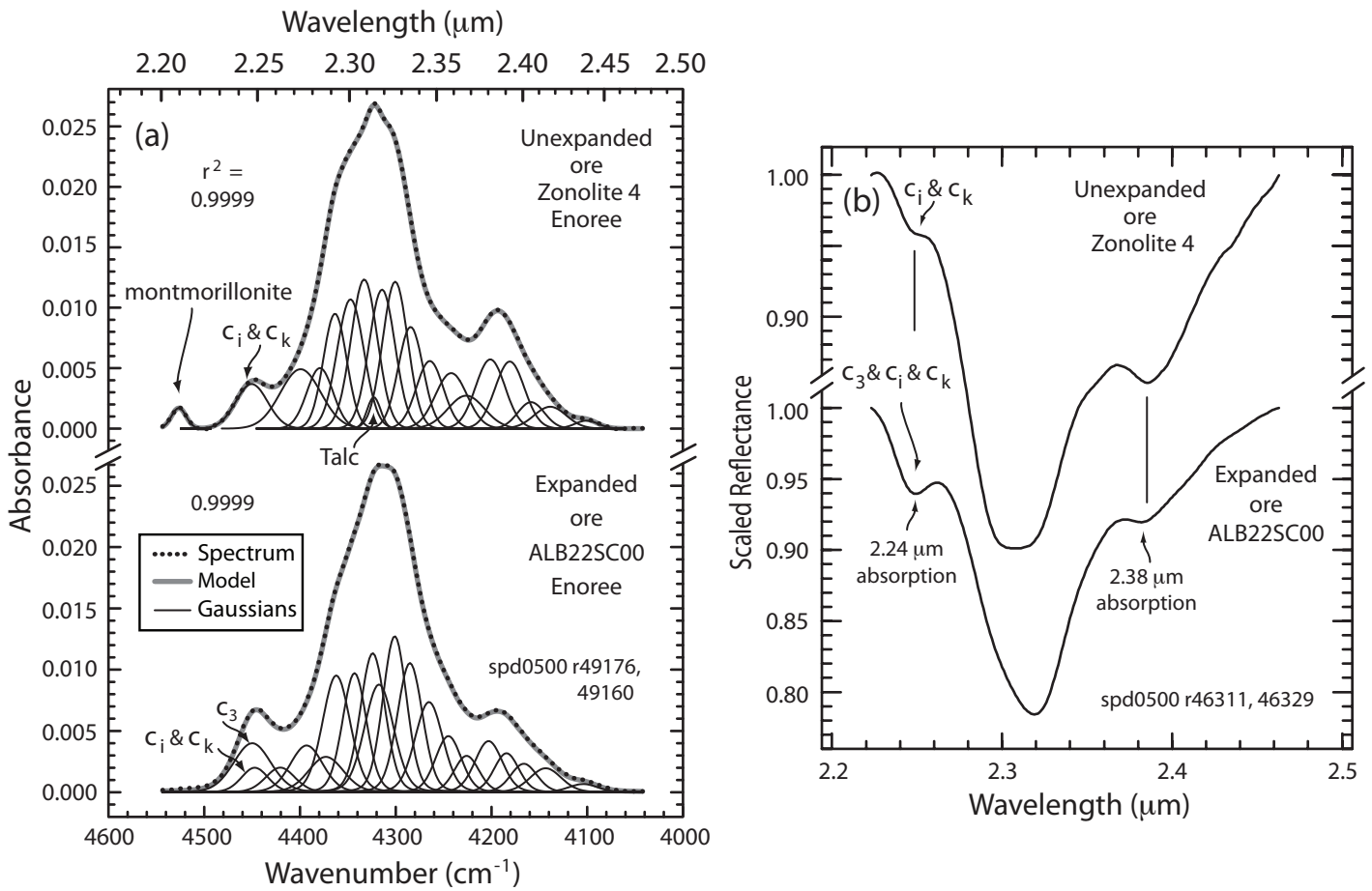Swayze et al. Figure 11
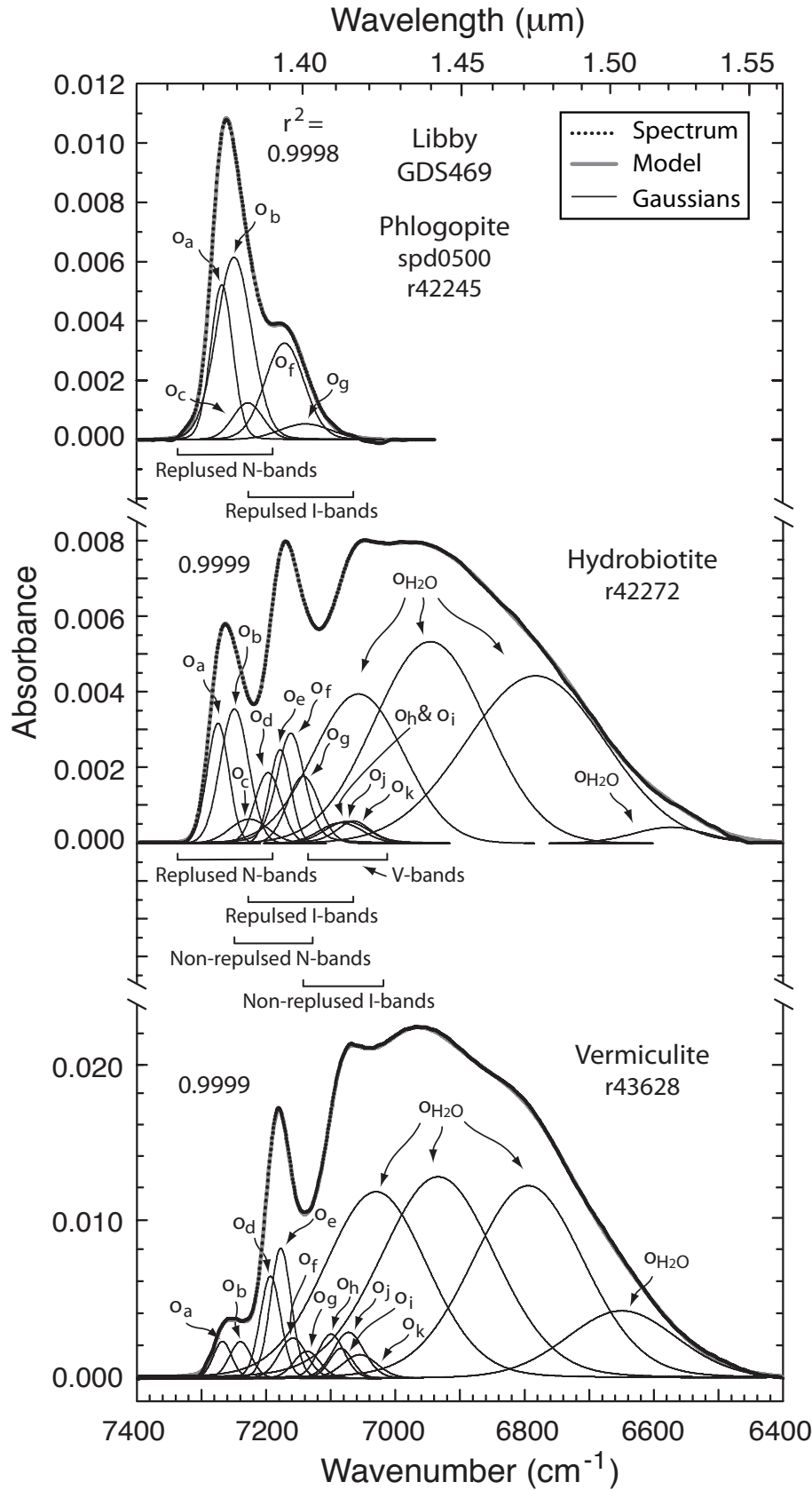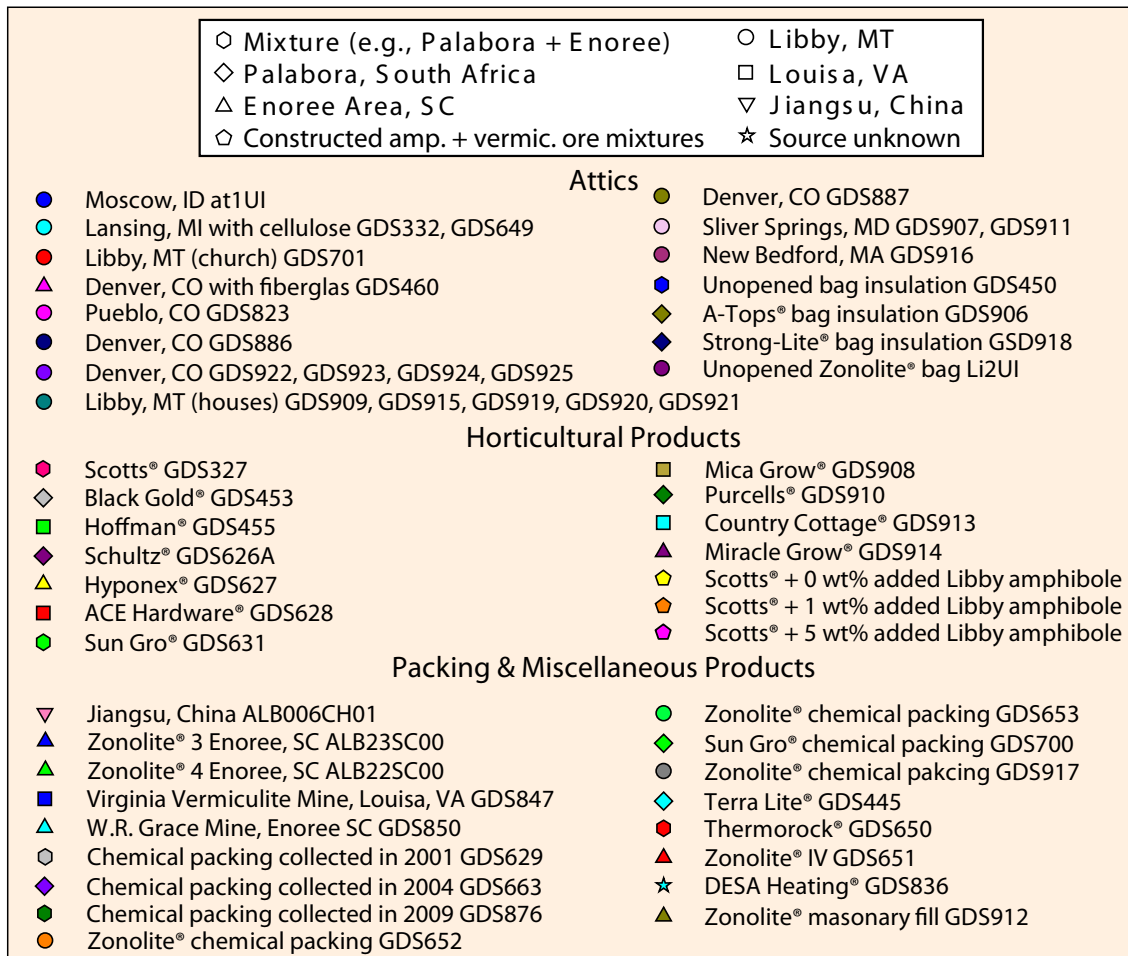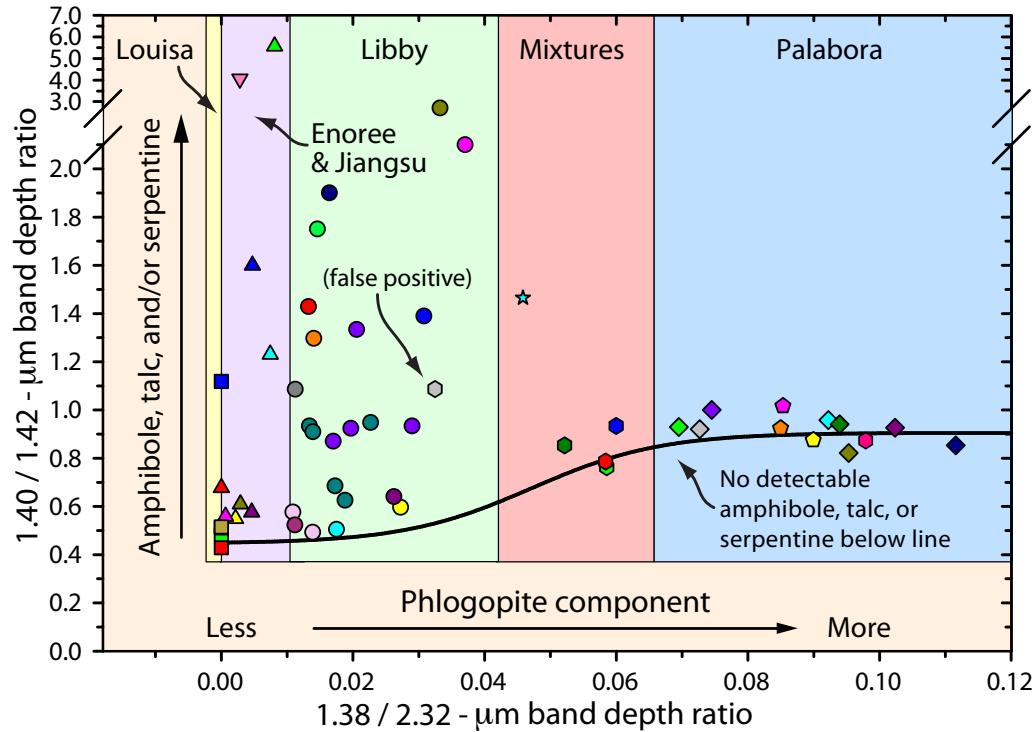
Swayze et al.   Figure 17

Swayze et al.   Figure 18

Swayze et al. Figure 20

Swayze et al.   Figure 21